AFGL-TR-88-0310

AD-A203 182

Study of Magnetic Reconnection

R. L. Stenzel
W. Gekelman
J. M. Urrutia

University of California
Department of Physics
Los Angeles, CA 90024

November 1988

DTIC
ELECTE
S **D**
DEC 1 2 1988

Final Report
6 November 1984-7 November 1988

APPROVED FOR PUBLIC RELEASE; DISTRIBUTION UNLIMITED

AIR FORCE GEOPHYSICS LABORATORY
AIR FORCE SYSTEMS COMMAND
UNITED STATES AIR FORCE
HANSCOM AIR FORCE BASE, MASSACHUSETTS 01731-5000

88 1 073

" This technical report has been reviewed and is approved for publication"
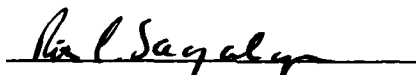

PAUL L. ROTHWELL
Contract Manager

NELSON C. MAYNARD
Branch Chief

FOR THE COMMANDER

RITA C. SAGALYN
Division Director

This report has been reviewed by the ESD Public Affairs Office (PA) and is releasable to the National Technical Information Service (NTIS).

Qualified requestors may obtain additional copies from the Defense Technical Information Center. All others should apply to the National Technical Information Service.

If your address has changed, or if you wish to be removed from the mailing list, or if the addressee is no longer employed by your organization, please notify AFGL/DAA, Hanscom AFB, MA 01731. This will assist us in maintaining a current mailing list.

Do not return copies of this report unless contractual obligations or notices on a specific document requires that it be returned.

REPORT DOCUMENTATION PAGE

1a. REPORT SECURITY CLASSIFICATION Unclassified			1b. RESTRICTIVE MARKINGS			
2a. SECURITY CLASSIFICATION AUTHORITY			3. DISTRIBUTION/AVAILABILITY OF REPORT Approved for public release; Distribution unlimited			
2b. DECLASSIFICATION/DOWNGRADING SCHEDULE						
4. PERFORMING ORGANIZATION REPORT NUMBER(S)			5. MONITORING ORGANIZATION REPORT NUMBER(S) AFGL-TR-88-0310			
6a. NAME OF PERFORMING ORGANIZATION University of California		6b. OFFICE SYMBOL (If applicable)	7a. NAME OF MONITORING ORGANIZATION Air Force Geophysics Laboratory			
6c. ADDRESS (City, State, and ZIP Code) Department of Physics Los Angeles, CA 90024			7b. ADDRESS (City, State, and ZIP Code) Hanscom AFB Massachusetts 01731-5000			
8a. NAME OF FUNDING/SPONSORING ORGANIZATION		8b. OFFICE SYMBOL (If applicable)	9. PROCUREMENT INSTRUMENT IDENTIFICATION NUMBER F19628-85-K-0003			
8c. ADDRESS (City, State, and ZIP Code)			10. SOURCE OF FUNDING NUMBERS			

			PROGRAM ELEMENT NO.	PROJECT NO.	TASK NO.	WORK UNIT ACCESSION NO.
			61102F	2311	G2	HG

11. TITLE (Include Security Classification)
Study of Magnetic Reconnection

12. PERSONAL AUTHOR(S)
R. L. Stenzel, W. Gekelman, J. M. Urrutia

13a. TYPE OF REPORT FINAL REPORT	13b. TIME COVERED FROM 11/6/84 TO 11/7/88	14. DATE OF REPORT (Year, Month, Day) 1988 November	15. PAGE COUNT

16. SUPPLEMENTARY NOTATION

17. COSATI CODES			18. SUBJECT TERMS (Continue on reverse if necessary and identify by block number)
FIELD	GROUP	SUB-GROUP	Magnetic reconnection
			Substorms
			Ion tearing mode

19. ABSTRACT (Continue on reverse if necessary and identify by block number)
The purpose of this research was to study magnetic reconnection in a laboratory setting. (Magnetic reconnection is considered to be the primary cause of substorms.) It was found possible to trigger magnetic reconnection through the ion tearing mode and associated magnetic and particle properties were studied in detail. Finally, a summary is given of the lessons learned in regard to laboratory experiments on magnetic reconnection.

20. DISTRIBUTION/AVAILABILITY OF ABSTRACT ☐ UNCLASSIFIED/UNLIMITED ☐ SAME AS RPT. ☐ DTIC USERS	21. ABSTRACT SECURITY CLASSIFICATION Unclassified	
22a. NAME OF RESPONSIBLE INDIVIDUAL Paul Rothwell	22b. TELEPHONE (Include Area Code)	22c. OFFICE SYMBOL AFGL/PHG

DD FORM 1473, 84 MAR   83 APR edition may be used until exhausted.   SECURITY CLASSIFICATION OF THIS PAGE
All other editions are obsolete.   Unclassified

ACKNOWLEDGEMENTS

CONTENTS

INTRODUCTION

The topic of the experimental research performed under Air Force contract was magnetic field line reconnection in a large laboratory plasma. The motivation was to test theoretical models and ideas applied to reconnection in space plasmas. Particular attention has been focused on the magnetic field topology which is thought to change by tearing instabilities resulting in impulsive conversion of magnetic energy to kinetic particle energies.

The first report, Reference 1, describes measurements and interpretations of triggered tearing modes in a neutral sheet. In these experiments multiple magnetic X- and O-points were imposed on the neutral sheet and growth/decay of these structures were followed in space and time. No major disruptions were observed.

Reference 2 summarizes the nonlinear interactions between fields and particles in a neutral sheet. Fully resolved particle distribution functions in three-dimensional velocity space have been measured. Likewise, fluctuations in the magnetic field have been resolved by three-dimensional correlation measurements. As shown in detail in Reference 3, these fluctuations consist of oblique whistler waves which, as demonstrated in Reference 4 are driven unstable by anisotropic tails in the electron distribution function. These tails are generated by particle acceleration in the reconnection electric field along the separator, i.e. by conversion of magnetic field energy via Faraday's law.

Reference 5 describes experiments on current sheet disruptions such as those which may arise in magnetic substorms or solar flares. Most striking is the observation of the formation of double layers in the current path. At these double layers, the magnetic field energy is converted to particle beams which, upon injection into the surrounding plasma, generate microinstabilities and heat electrons and ions.

Reference 6 summarizes our understanding of reconnection in a laboratory plasma and relates the finding to observations in space. It is pointed out that MHD theories

cannot account for the plasma dynamics near null points since the ions are essentially unmagnetized and the magnetic fields/currents are mainly controlled by the electrons. For example, magnetic field transport occurs by electron whistler waves rather than ionic Alfven waves.

Due to space charge coupling of electrons and ions, an electron current system can be drastically modified by the ion dynamics such as demonstrated in Reference 7. It is observed that strong current flow in narrow flux tubes leads to space charge electric fields which pump the ions/plasma out of the flux tube leading to a current disruption. Such phenomena may account for the frequently observed turbulence and fine scale structure of currents in neutral sheets.

SUMMARY

In summary, extensive data on magnetic field line reconnection have been obtained in a laboratory plasma which have helped to understand reconnection processes close to magnetic null regions. These regions are difficult to study in the magnetotail due to the variability of the solar wind, and they have not been studied theoretically due to the difficulty to use kinetic theory coupled with electromagnetism. We think the laboratory effort contributed to the understanding of reconnection in a parameter regime not accessible by other means.

REFERENCES

1. "Triggered Tearing Modes in a Magnetic Neutral Sheet," R. L. Stenzel and W. Gekelman, PPG 756 (1983).

2. "Nonlinear Interactions During Magnetic Field-Line Reconnection in Plasmas," R. L. Stenzel and W. Gekelman, Physica 12D, 133-144 (1984).

3. "Magnetic Field Line Reconnection Experiments 6. Magnetic Turbulence," W. Gekelman and R. L. Stenzel, J. Geophys. Res. 89, 2715 (1984).

4. "Measurement and Instability Analysis of Three-Dimensional Anisotropic Electron Distribution Functions," W. Gekelman and R. L. Stenzel, Phys. Rev. Lett. 54, 2414 (1985).

5. "Laboratory Experiments on Current Sheet Disruptions, Double Layers, Turbulence and Reconnection," R. L. Stenzel and W. Gekelman in Unstable Current Systems and Plasma Instabilities in Astrophysics, M. R. Kundu and G. D. Holman, editor, pp. 47-60, Int'l Astron. Union, D. Reidel Publ. Co. (1985).

6. "Lessons from Laboratory Experiments on Reconnection," R. L. Stenzel, W. Gekelman and J. M. Urrutia, Adv. Space Res. 6, 135-147 (1986).

7. "Anomalous Currents to an Electrode in a Magnetoplasma," J. M. Urrutia and R. L. Stenzel, Phys. Rev. Lett. 57, 715 (1986).

APPENDIX   A

Triggered Tearing Modes in a

Magnetic Neutral Sheet

R. L. Stenzel and W. Gekelman

PPG 756   November 1983

Department of Physics
University of California
Los Angeles, CA 90024

Abstract

An experimental investigation of tearing mode instabilities in a magnetic neutral sheet has been performed. A long flat current sheet is generated in a large laboratory plasma. It is perturbed by pulsing a current through a fine wire along the separator so as to trigger the formation of magnetic O-and X-points. Two magnetic islands are excited. Their growth, propagation and merging within the neutral sheet is observed.

Introduction

Tearing mode instabilities are considered to be responsible for the disruption of current sheets in solar flares and magnetospheric substorms (Birn and Schindler, 1981; Hones, 1980). Although tearing modes have been investigated theoretically in great detail (Furth et al., 1963; Coroniti, 1977; Park et al., 1983) their experimental investigation has been mostly restricted to Tokamaks (Von Goeler et al., 1974; Robinson and McGuire, 1979). These toroidal devices have magnetic field topologies substantially different from those in space and in-situ measurements of the magnetic fields are not possible due to high temperatures and densities. In the UCLA reconnection experiments a long flat reverse field geometry has been established and diagnosed in detail (Stenzel et al., 1983a; Gekelman et al., 1982). The current sheet is expected to be unstable to tearing and indeed, the spontaneous formation of magnetic islands has been observed in a certain parameter range. In order to study tearing modes in a controlled fashion it is desirable to perturb a marginally unstable neutral sheet with an external trigger pulse and then to observe its space-time evolution. Such experiments will be described here.

Experiment

A linear discharge plasma column shown in Fig. 1 is generated with a 1 m diameter cathode. Typical plasma parameters are a density $n_e \simeq 10^{12} cm^{-3}$, temperature $kT_e \simeq 10$ eV, $kT_i \simeq 1$eV, Argon gas pressure $p \simeq 2 \times 10^{-4}$ Torr, and an axial confining dc

magnetic field $B_{yo} \simeq 10G$. The plasma is uniform, collisionless
and highly reproducible in pulsed mode. Typical pulse widths are
$t_p \simeq 5$ msec and repetition times $t_r \simeq 2$ sec.

In order to generate a current sheet a pulsed transverse
magnetic field $\vec{B}_\perp (x,y,t)$ is applied. It is generated by pulsing
axial currents (I $\simeq$ 10kA, $t_{rise} \simeq 100 \mu sec$) through two plates
parallel to the plasma column. The magnetic field topology
contains in vacuum an X-type neutral point at the center.
However, in the presence of plasma electron currents are induced
which are so large ($I_p \simeq 1000A$) that the magnetic field topology
is strongly modified. While the current prefers to flow in the
null regions of the transverse magnetic field it can rearrange
the neutral region in a self-consistent manner. As predicted by
MHD theories (Dungey, 1958) we observe during the rise of the
external magnetic field the formation of a classical neutral
sheet shown in Fig. 2a. The corresponding current sheet, $J_y = \nabla \times \vec{B}_\perp/\mu_o$, has a thickness $\Delta z \simeq 5$ cm which lies in between the
collisionless skin depth ($c/\omega_{pe} \simeq 0.8$ cm) and the ion Larmor
radius ($r_{ci} \simeq 30$ cm).

Current sheets can break up into current filaments through
the process of tearing mode instabilities. Fig. 2b shows the
observation of a large magnetic island which has grown in the
original neutral sheet at larger current densities. In order to
study in a controlled manner the growth of such modes the current
sheet is kept near threshold for tearing and a trigger magnetic
island is excited. As shown in Fig. 3 this is accomplished by
inserting a fine wire (0.5 mm diam.) parallel to the neutral

sheet along the full length of the device and applying a current
pulse to it (900 A, 20μsec). The wire is insulated from the
plasma and causes only a small local density perturbation.

Time and space resolved measurements of the magnetic field
topology are obtained with a movable magnetic probe pair (B_x,
B_z). For repeated pulses the time history of $\vec{B}_\perp(t)$ is digitally
recorded at typically 300 different positions in the x-z plane
transverse to the axial currents J_y. The large data flow
requires the extensive use of modern digital data processing
equipment including fast anolog-to-digital converters (100 MHz,
32 k words), on-line minicomputer (LSI 11/23), an array processor
(MAP 200), and a data link to a large off-site computer (Cray 1)
for final data analysis and display. Not only magnetic probe
signals are analyzed in this manner but also signals from
particle detector, Langmuir probes and wave detectors (Stenzel et
al., 1983b). Fig. 4 shows a schematic summary of the diagnostics
and data processing setup.

Triggered Tearing Modes

At a time t = 30μsec after the generation of the current
sheet the trigger pulse is applied to the axial wire. Its
waveform is that of a half-sine wave of duration T = π/ω ≈ 20μsec
and peak current I_{max} ≈ 900 A and peak voltage V_{max} = L dI/dt ≈
1000 V.

A sequence of vector magnetic field maps at various times t
is presented in Fig. 5 a-ℓ. Just after turn-on of the current
pulse (t = 30.2μsec, Fig. 5a) the perturbation magnetic field

becomes visible. The x-z plane of measurement is chosen
inadvertedly too high with respect to the device axis or trigger
wire. At t = 36μsec (Fig. 5b) the perturbation magnetic field
stands clearly out from the neutral sheet. The point of
measurement is at the center of each vector whose length scales
linearly with the local field strength. The data points are
separated by $\Delta x = \Delta z = 2$ cm. Due to the rapid variation of $\vec{B}_\perp$
near the wire the measured field appears somewhat random but
close inspection shows that the field lines circle around the
wire located at $x \simeq 33$ cm, $z \simeq 6$ cm. The current in the wire flows
normal to the x - z plane in the same direction as the plasma
current, i.e. toward the cathode.

Fig. 5c and d show the growth of the trigger magnetic island
up to its maximum at $t \simeq 40$ μsec. The addition of the large
magnetic island to the neutral sheet has generated two magnetic
X-points at $x_1 \simeq 17$ cm, $x_2 \simeq 50$ cm and $z_{1,2} \simeq 9$ cm. The growing
magnetic island tends to decrease the plasma current since, by
Lenz's law the induced currents are opposite to the applied
current. The axial plasma current is greatly impeded by the
strong transverse magnetic field of the island ($B_\perp = 10...100$ G).
An $\underline{E} \times \underline{B}$ plasma drift leads to the expulsion of plasma radially
away from the wire. At typical ion velocities $v_i \simeq c_s \simeq 5 \times 10^5$
cm/sec the plasma can move in $\Delta t = 10$μsec over distances $\Delta r \simeq 5$
cm which leads to significant plasma losses in the island. The
X-points shift outward with the expanding plasma. However, since
the separatrices at the X-points intersect at nearly 90° little
current flows in these regions.

11

Besides the transverse magnetic field there is also an axial magnetic field component, $B_{yo} \simeq 10$ G, applied to the plasma. The peak plasma pressure nkT $\simeq 10^{12}$ cm^{-3} x 10eV is larger than the magnetic field pressure, nkT $\simeq 4$ $(B_{yo}^2/ 2\mu_o)$. This implies a significant modification of the axial field. Observations show that the axial field does not completely vanish but can locally decrease to 50% of its external value. Nevertheless, the field lines around the wire are helical with varying pitch like in a flux rope. The current may actually arrange itself in a force-free configuration $(\nabla$ x $\underline{B} \parallel \underline{B})$. Three-dimensional field maps $[B_{x (x,y,z)}, B_{y (x,y,z)}$ and $B_{z (x,y,z)}]$ would be required to conclusively establish the field topology. The capability for performing such measurements is presently being build up. It requires a fully three-dimensional probe motion, three vector component measurements and a full-size computer (VAX 11/750) for an order of magnitude larger data arrays.

Fig. 5e and f show the field topology during the decrease of the current applied to the wire. At this time the inductive electric field has changed sign and induces plasma currents in the same direction as the wire currents. These currents flow near the neutral points whose separatrix now intersects at angles different from 90° $(\nabla$ x $B \neq 0)$.

Fig. 5g and h are the most interesting cases showing the excitation of two magnetic islands. These islands are induced in the current sheet in response to the time-varying wire current. It is important to note that the induced plasma current flows in two current channels located in the original neutral sheet rather

12

than in a coaxial return current distributed symmetrically around
the wire. This feature indicates the inherent instability for
the current sheet to filament or to tear.

While in Fig. 5h the 0-and X-points are clearly separated
one observes in Fig. 5i and j the merging of both null points.
The current in the axial wire has reversed sign and is growing in
magnitude. The trigger field lines are reversed from those of
the first half cycle. The resultant field topology forms neutral
points above and below the wire. The normal component B_z in the
original neutral sheet is enhanced so that the null region
vanishes.

Finally, Fig. 5k and l shows the change in the field
topology during the decrease of the trigger current. The null
region above the trigger wire has separated into two X-points
($x_1 \simeq 15$ cm, $x_2 \simeq 50$ cm, $z \simeq 20$ cm). Over a large region
around the wire the field lines are linked with it indicating a
substantial plasma current parallel to the wire current. It is
worth noting that at $t \simeq 80\mu sec$ the applied current through the
plate electrodes has reached its maximum yet the plasma current
has reversed the applied B_x component. Except near the
boundaries the field inside the plasma is established self-
consistently by $\nabla \times \underline{B} = \mu_o \underline{J}$.

Acknowledgments

stimulating these experiments and for participating in the data taking phase. We also acknowledge helpful discussions with Dr. M.Ashour-Abdallah. The technical assistance from Mr. J. M. Urrutia is appreciated. This work was supported by the Air Force Geophysics Laboratory under contract No. F19628-82-K0019.

References

1. Birn, J. and K. Schindler, Two ribbon flares: magnetospheric equilibria, in Solar Flare Magnetohydrodynamics, (ed. E. R. Priest) p. 337, Gordon and Breach, London, 1981.

2. Coroniti, F. V., Nonlinear evolution of the collisionless tearing mode, Phys. Rev. Lett. 38, 1355-1358, 1977.

3. Dungey, J. W., Cosmic Electrodynamics, Cambridge University Press, New York, 1958.

4. Furth, H. P., J. Killeen and M. Rosenbluth, Finite resistivity instabilities in a sheet pinch, Phys. Fluids 6, 495-484, 1963.

5. Gekelman, W., R. L. Stenzel and N. Wild, Magnetic field line reconnection experiments, Physica Scripta T2/2, 277-287, 1982.

6. Hones, E. W., Jr., Plasma flow in the magnetotail and its implications for substorm theories, in Dynamics of the Magnetosphere, ed. S.-I. Akasofu, p. 545, D. Reidel Publ. Co, Dordrecht, Holland, 1980.

7. Park, W., D. A. Monticello, and R. B. White, Reconnection rates of magnetic fields, Princeton Plasma Physics Lab Report 2014 (submitted to Phys. Fluids), 1983.

8. Robinson, D. C., and K. McGuire, Magnetic island and disruptions in the Tosca tokamak, Nuclear Fusion 19, 115-119, 1979.

9. Stenzel, R. L., W. Gekelman and N. Wild, Magnetic field line reconnection experiments 5. Current disruptions and double layers, J. Geophys. Res. 88 4793-4804, 1983a.

10. Stenzel, R. L., W. Gekelman, N. Wild, J. M. Urrutia, and D.Whelan, Directional velocity analyzer for measuring electron distribution functions in plasmas, Rev. Sci. Instrum. 54, 1302-1310, 1983b.

11. Von Goeler, S., W. Stodiek, and N. Sauthoff, Studies of internal disruptions and m = 1 oscillations in tokamak discharges with soft x-ray techniques, Phys. Rev. Lett. 33, 1201-1203, 1974.

Figure Captions

Fig. 1 Schematic picture of the experimental arrangement. (a) Cross-sectional view showing parallel plate electrodes with pulsed currents I_S and magnetic field lines $\vec{B}_\perp$ without plasma. (b) Side view of the device with main electrodes, currents (I_p, I_S) electric fields ($\vec{E} = -\dot{\vec{A}} - \nabla\phi_p$), and magnetic fields ($\vec{B} = \vec{B}_\perp + \vec{B}_{yo}$). The coordinate system common in magnetospheric physics has been adopted where y is along the neutral line (device axis), x is along the horizontal neutral sheet, and z is normal to the sheet.

Fig. 2 Transverse magnetic field topologies during field line reconnection. (a) Magnetic neutral sheet (b) Magnetic island (O-point with adjacent X-points) due to tearing instability.

Fig. 3 Schematic experimental arrangement for triggering tearing modes. A fine wire is stretched along the device axis and a current pulse is passed through it. It excites magnetic O- and X-points in the current sheet.

Fig. 4 Block diagram of the plasma diagnostics performed with various probes and a digital data acquisition system. Fast mass data handling with computers allows one to perform time and space resolved vector measurements, statistical analysis and particle distribution function measurements.

Fig. 5 Time evolution of the transverse magnetic field topology $\vec{B}_{\perp(x,z)}$ in response to the trigger magnetic island.

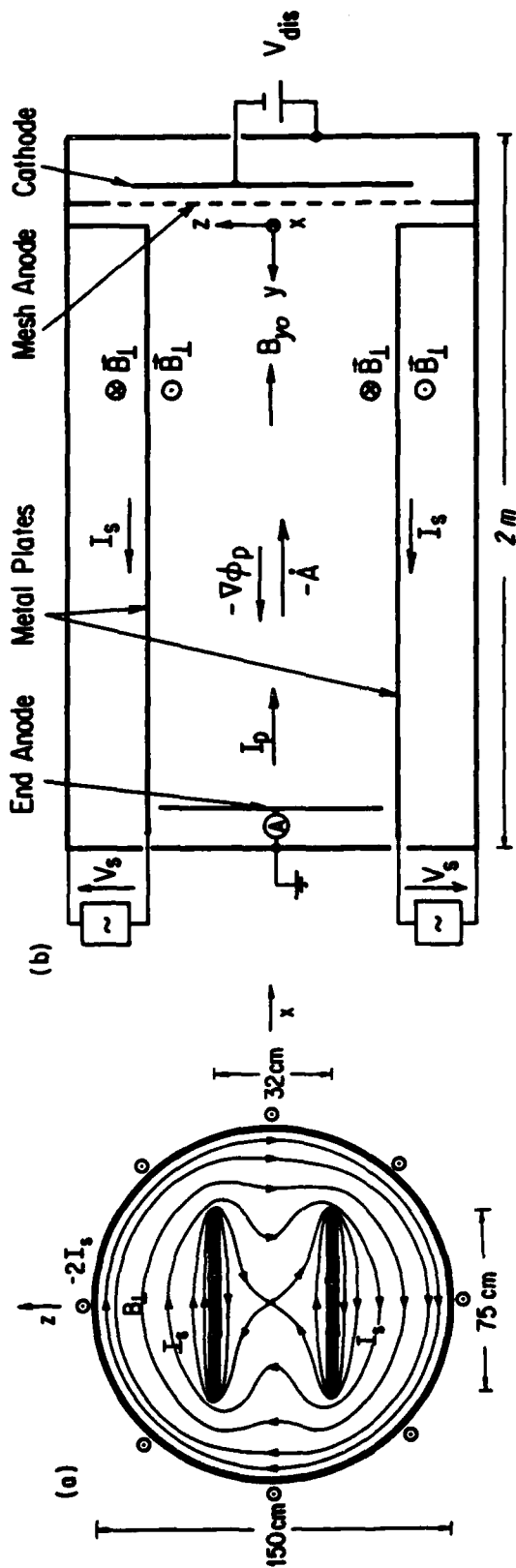The excitation of two O-points and X-points due to current sheet tearing is clearly visible in Fig. 5h.
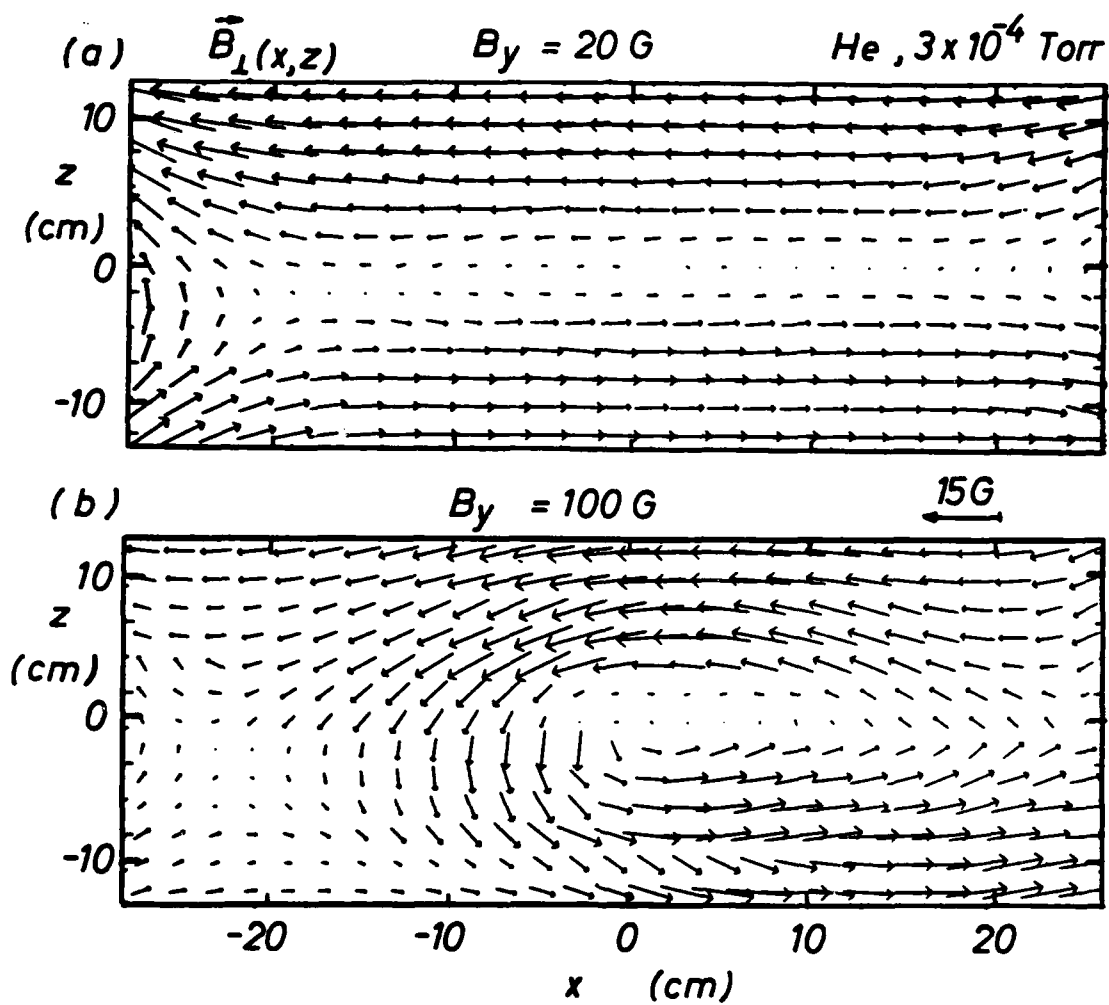
Fig. 1

17

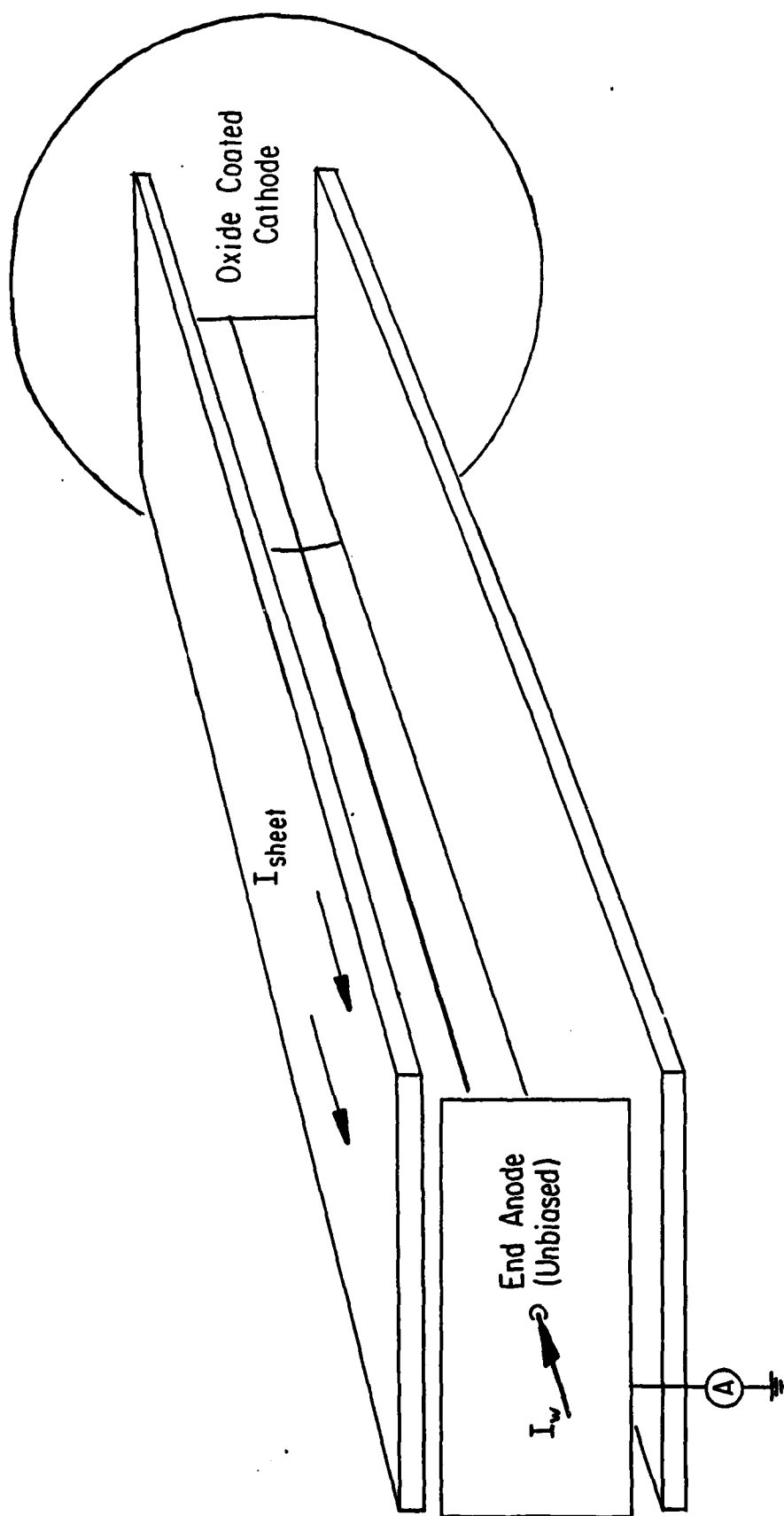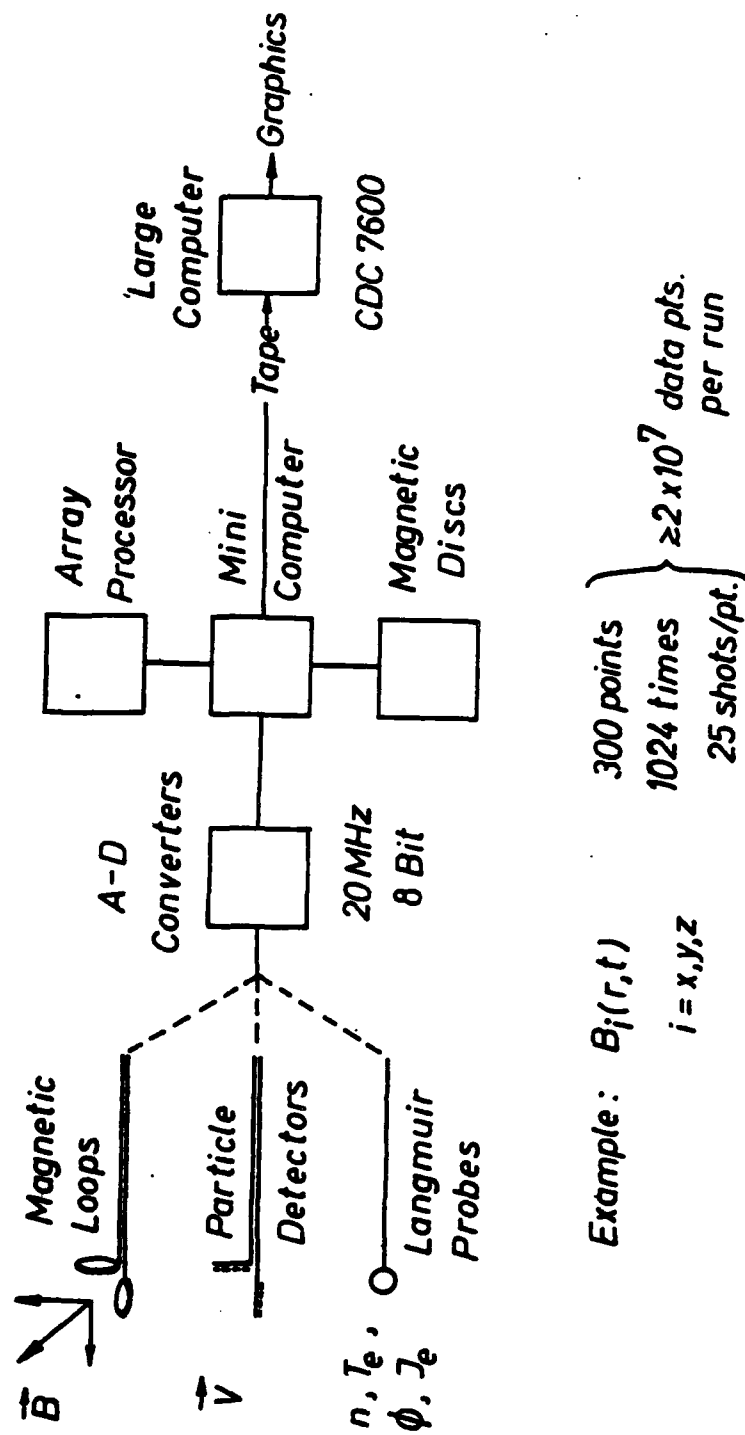(a) $\vec{B}_\perp(x,z)$ $B_y = 20\ G$ $He\ ,3\times 10^{-4}\ Torr$

(b) $B_y = 100\ G$ $15G$

x   (cm)

Figure 2

Figure 3

19

Magnetic
Loops

$\vec{B}$

Particle
Detectors

$\vec{V}$

Langmuir
Probes

$n, T_e,$
ϕ, J_e

A-D
Converters

20 MHz
8 Bit

Array
Processor

Mini
Computer

Magnetic
Discs

Large
Computer

Tape

CDC 7600

Graphics

Example: $B_i(r,t)$
$i = x,y,z$

300 points
1024 times
25 shots/pt.

$\geq 2 \times 10^7$ data pts.
per run

Figure 4

20

LINEAR VECTORS AXIAL WIRE

AUG 16 1983   Y= 137.0 CM
    BAVE= 2.88E+00 GAUSS
    BMAX(64,20) = 7.31E+00 GAUSS   T =   30.20 US
    BMIN(38, 6) = 2.27E-01 GAUSS

LINEAR VECTORS AXIAL WIRE

AUG 16 1983   Y= 137.0 CM
    BAVE= 3.59E+00 GAUSS
    BMAX(32, 4) = 2.45E+01 GAUSS   T =   36.00 US
    BMIN(42, 6) = 8.26E-01 GAUSS
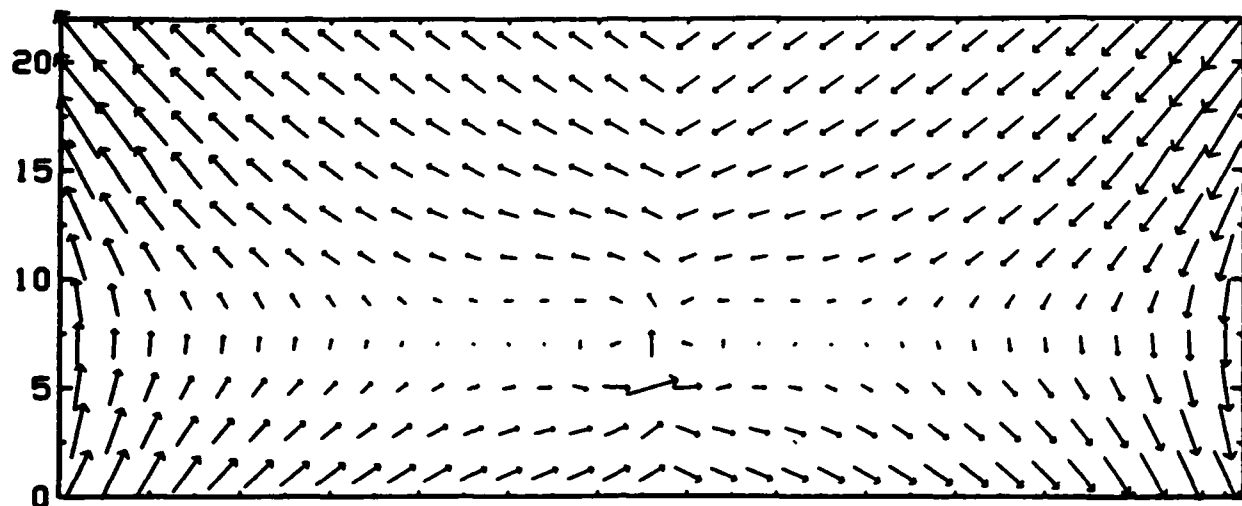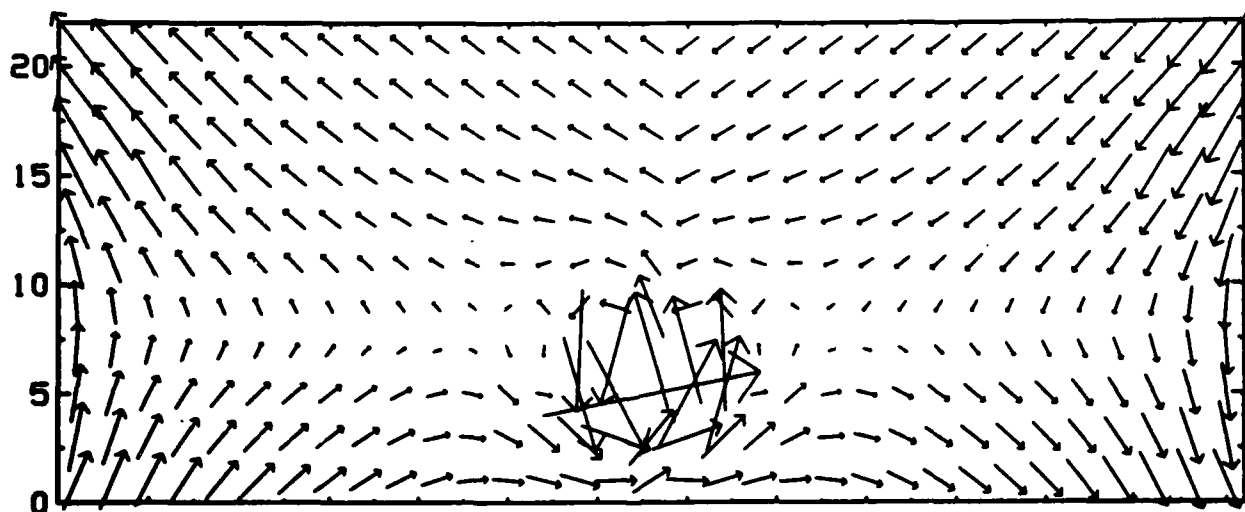
Figure 5a, b

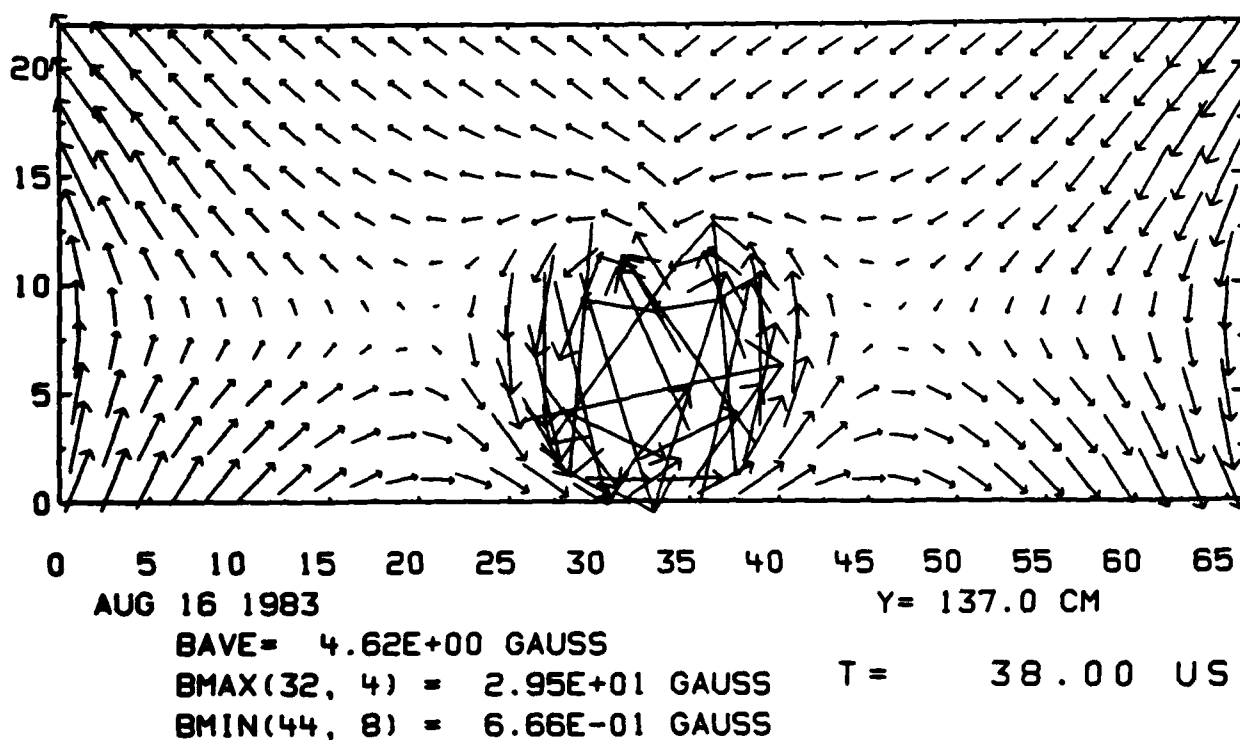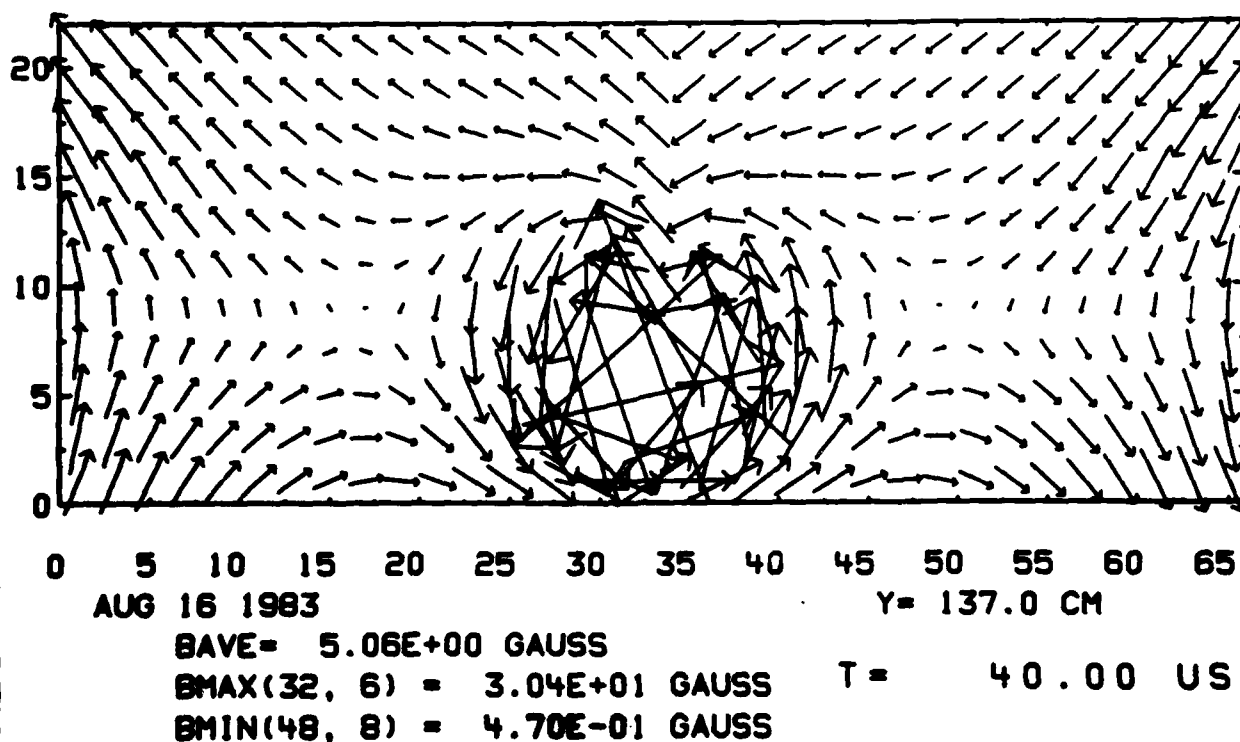LINEAR VECTORS AXIAL WIRE
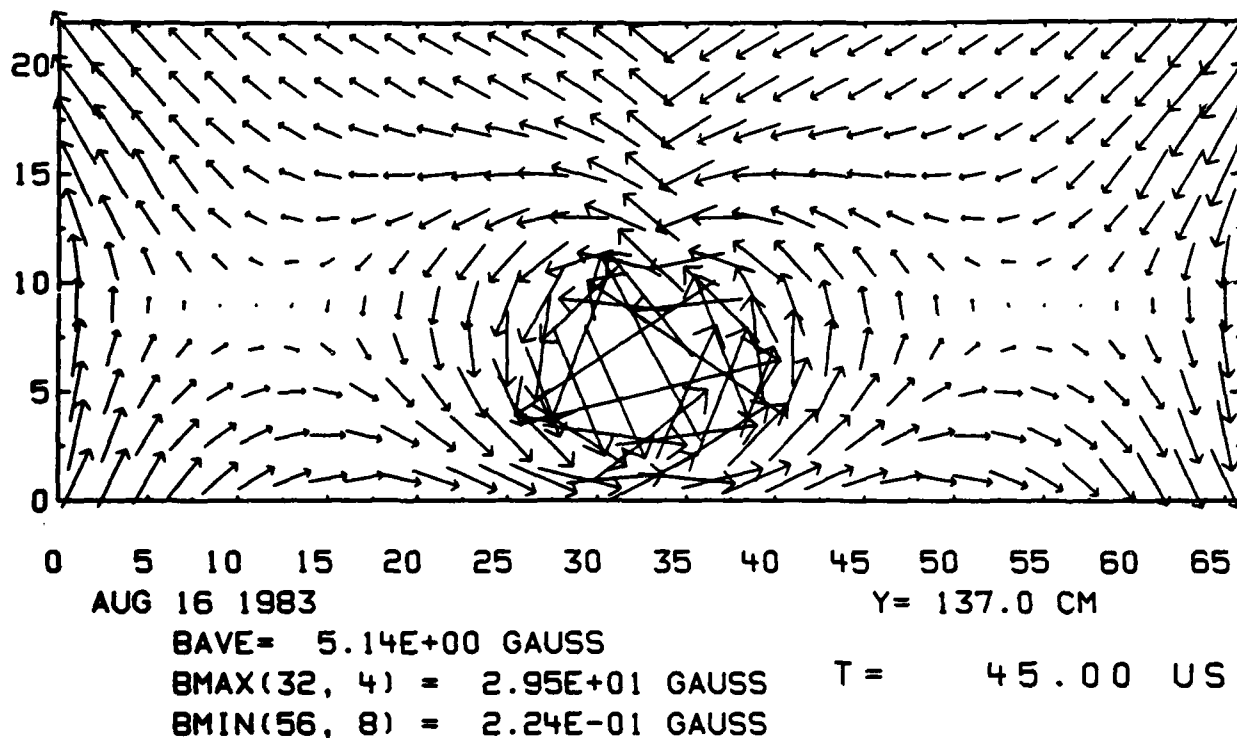
0   5   10   15   20   25   30   35   40   45   50   55   60   65

AUG 16 1983   Y= 137.0 CM

    BAVE= 4.62E+00 GAUSS
    BMAX(32, 4) = 2.95E+01 GAUSS   T =   38.00 US
    BMIN(44, 8) = 6.66E-01 GAUSS

LINEAR VECTORS AXIAL WIRE

0   5   10   15   20   25   30   35   40   45   50   55   60   65

AUG 16 1983   Y= 137.0 CM

    BAVE= 5.06E+00 GAUSS
    BMAX(32, 6) = 3.04E+01 GAUSS   T =   40.00 US
    BMIN(48, 8) = 4.70E-01 GAUSS

Figure 5c, d

22

LINEAR VECTORS AXIAL WIRE

0   5   10   15   20   25   30   35   40   45   50   55   60   65

AUG 16 1983   Y= 137.0 CM

BAVE= 5.14E+00 GAUSS

BMAX(32, 4) = 2.95E+01 GAUSS   T =   45.00 US

BMIN(56, 8) = 2.24E-01 GAUSS

LINEAR VECTORS AXIAL WIRE

0   5   10   15   20   25   30   35   40   45   50   55   60   65

AUG 16 1983   Y= 137.0 CM

BAVE= 4.08E+00 GAUSS

BMAX(32, 4) = 1.49E+01 GAUSS   T =   50.10 US

BMIN(52, 8) = 1.12E-01 GAUSS

Figure 5e, f

23
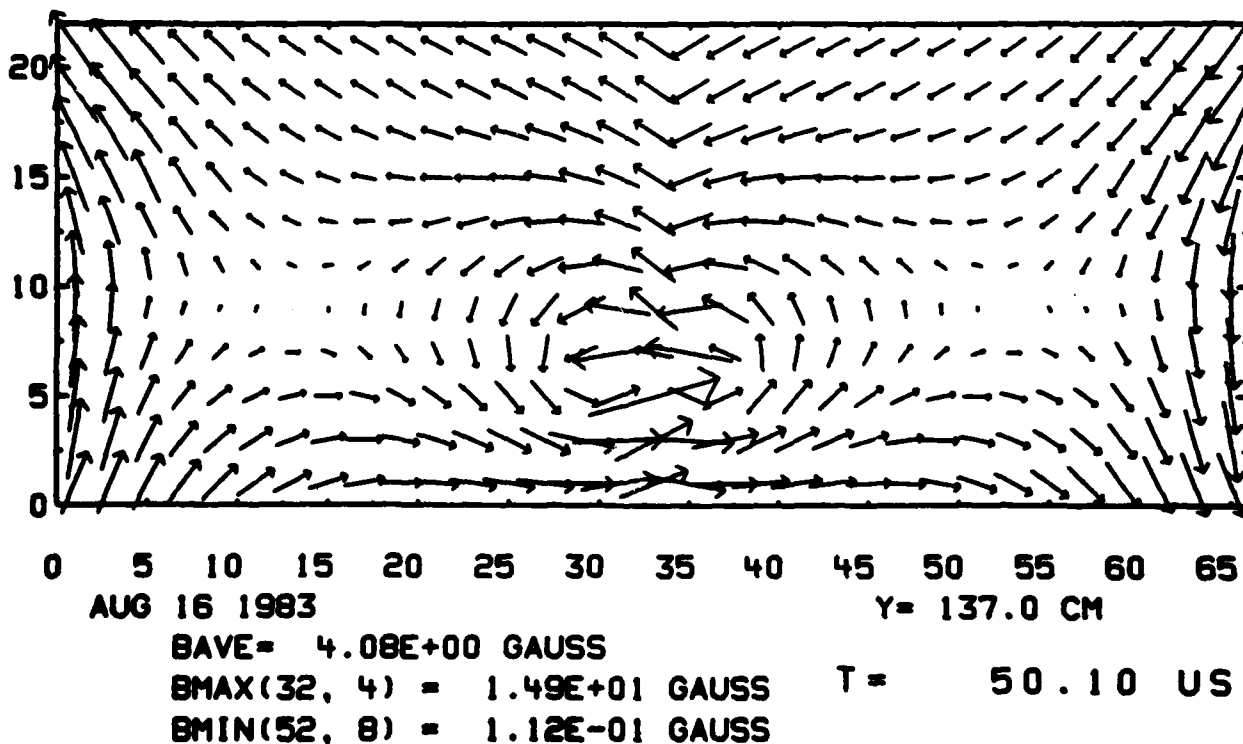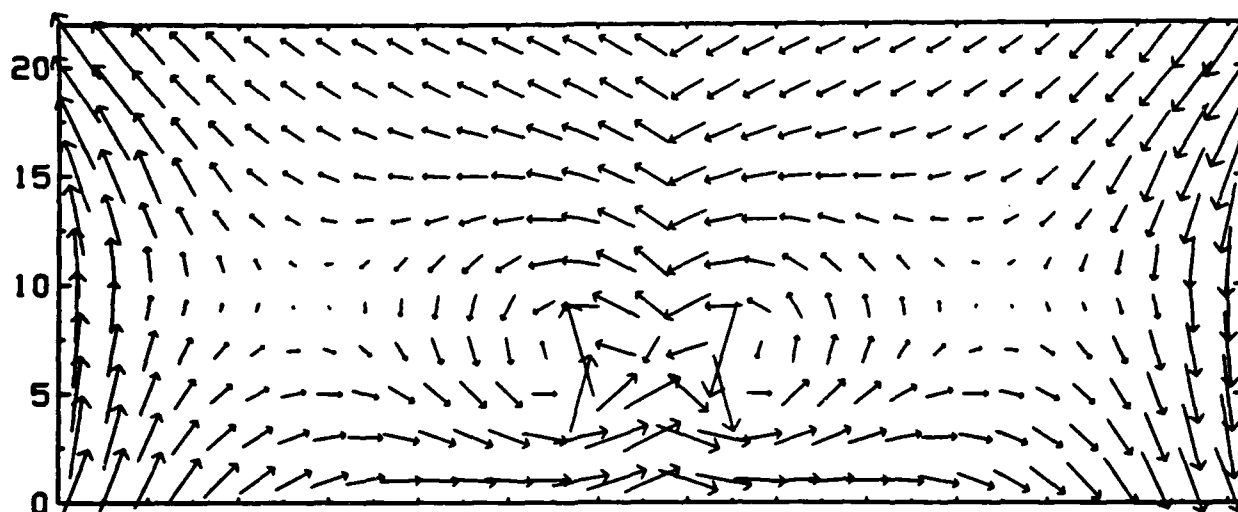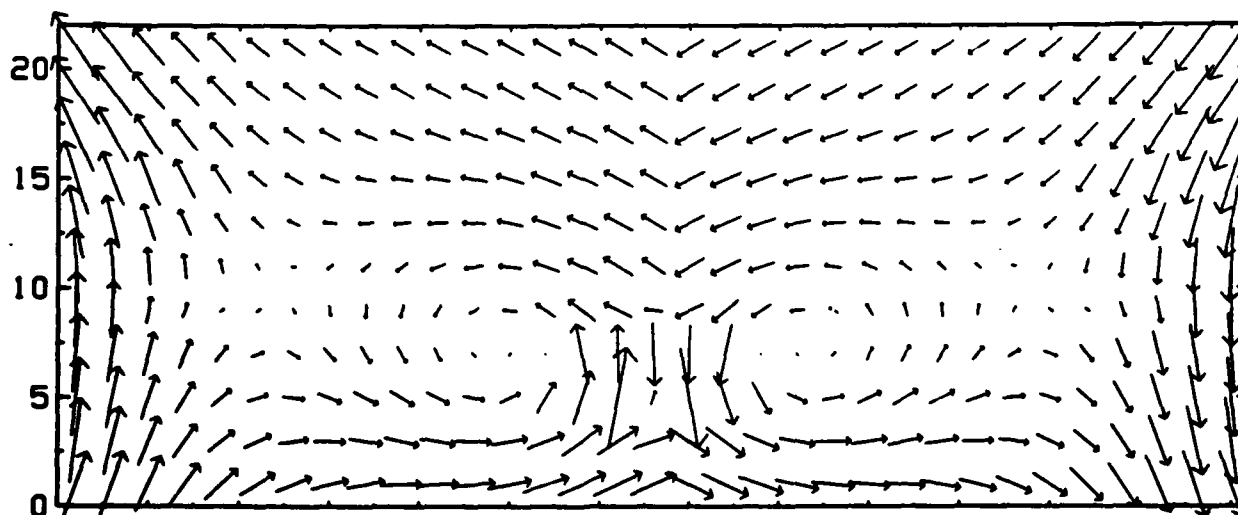
LINEAR VECTORS AXIAL WIRE

0   5   10   15   20   25   30   35   40   45   50   55   60   65

AUG 16 1983   Y= 137.0 CM
    BAVE= 3.79E+00 GAUSS
    BMAX(36, 6) = 9.13E+00 GAUSS   T =   52.00 US
    BMIN(50, 8) = 3.09E-01 GAUSS
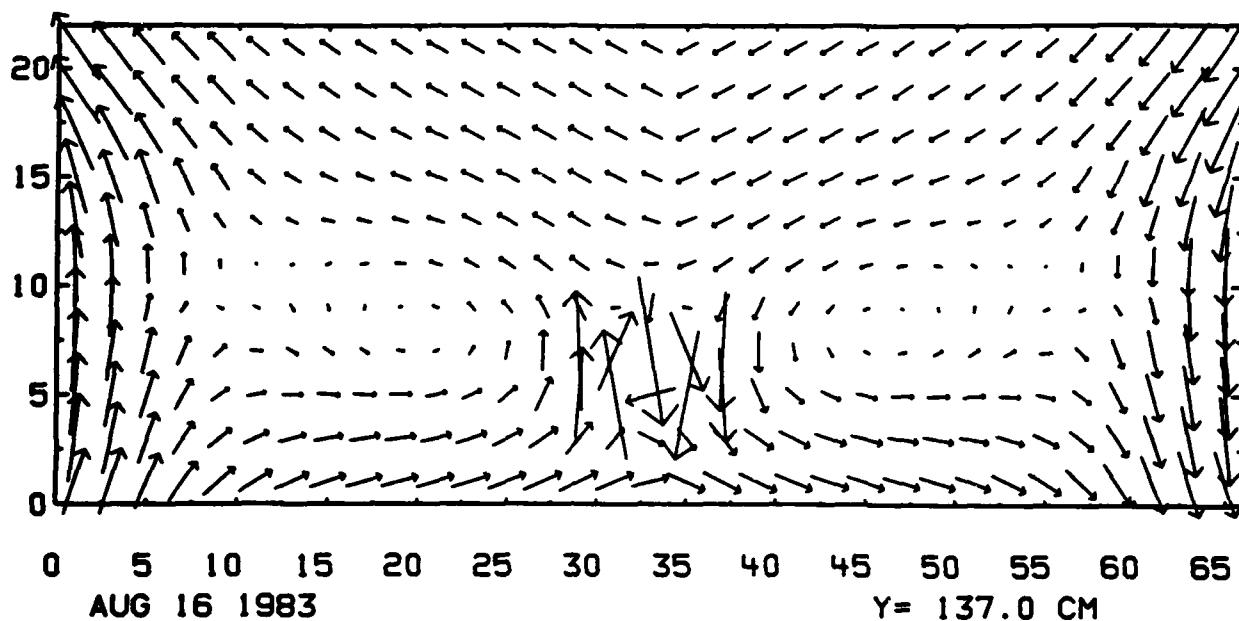
LINEAR VECTORS AXIAL WIRE

0   5   10   15   20   25   30   35   40   45   50   55   60   65

AUG 16 1983   Y= 137.0 CM
    BAVE= 3.45E+00 GAUSS
    BMAX(34, 4) = 9.40E+00 GAUSS   T =   53.50 US
    BMIN(38, 6) = 1.50E-01 GAUSS

Figure 5g, h

24

LINEAR VECTORS AXIAL WIRE
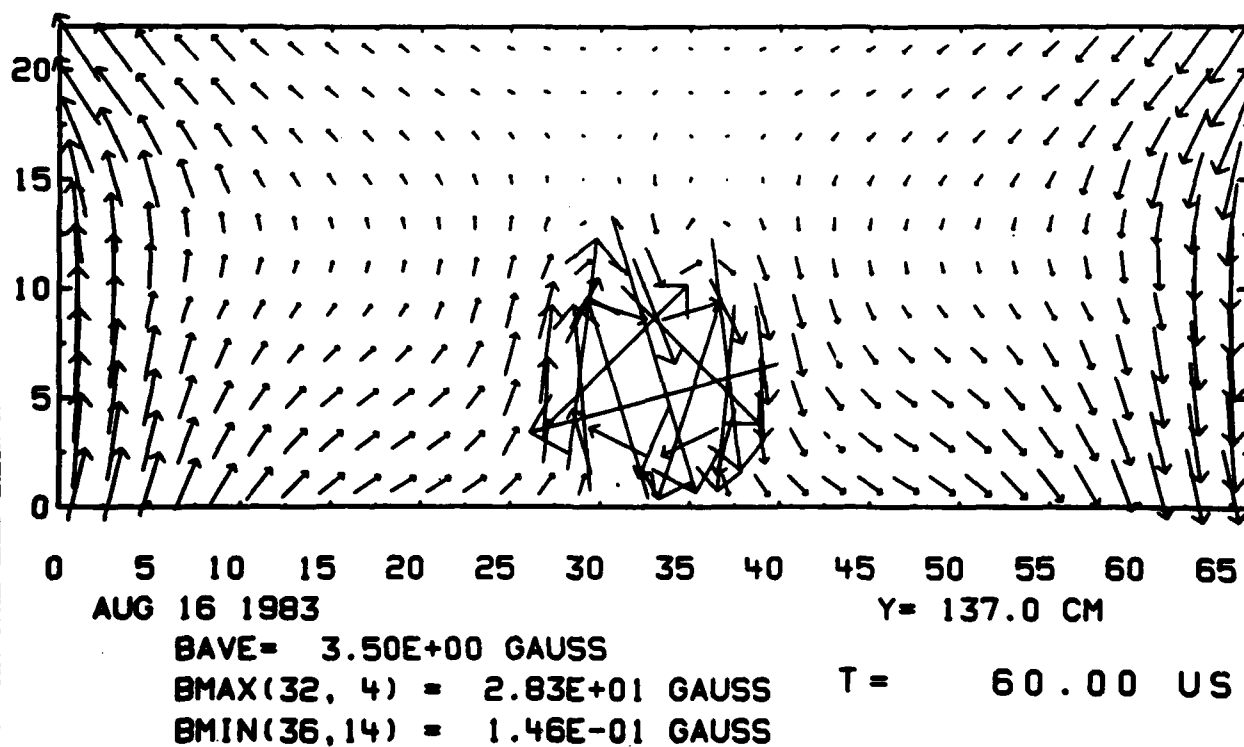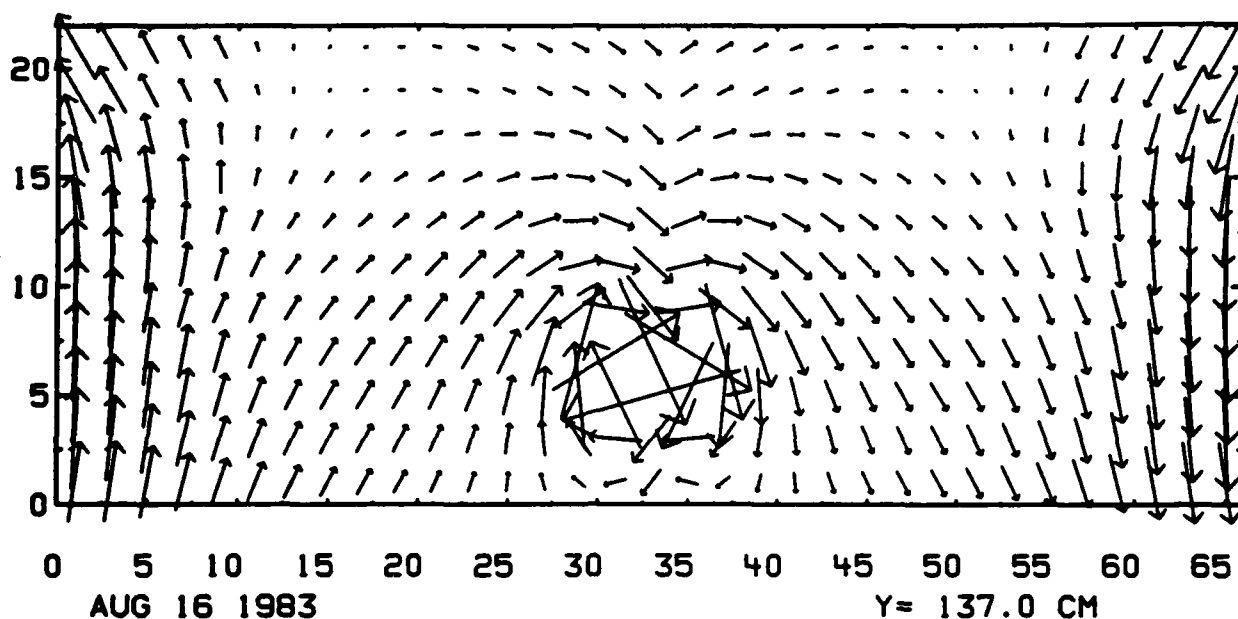

0   5   10   15   20   25   30   35   40   45   50   55   60   65

AUG 16 1983   Y= 137.0 CM

    BAVE= 3.28E+00 GAUSS
    BMAX(32, 6) = 1.38E+01 GAUSS   T =   55.00 US
    BMIN(54,10) = 2.61E-01 GAUSS

LINEAR VECTORS AXIAL WIRE

0   5   10   15   20   25   30   35   40   45   50   55   60   65

AUG 16 1983   Y= 137.0 CM

    BAVE= 3.50E+00 GAUSS
    BMAX(32, 4) = 2.83E+01 GAUSS   T =   60.00 US
    BMIN(36,14) = 1.46E-01 GAUSS

Figure 51, j

25

LINEAR VECTORS AXIAL WIRE

0   5   10   15   20   25   30   35   40   45   50   55   60   65

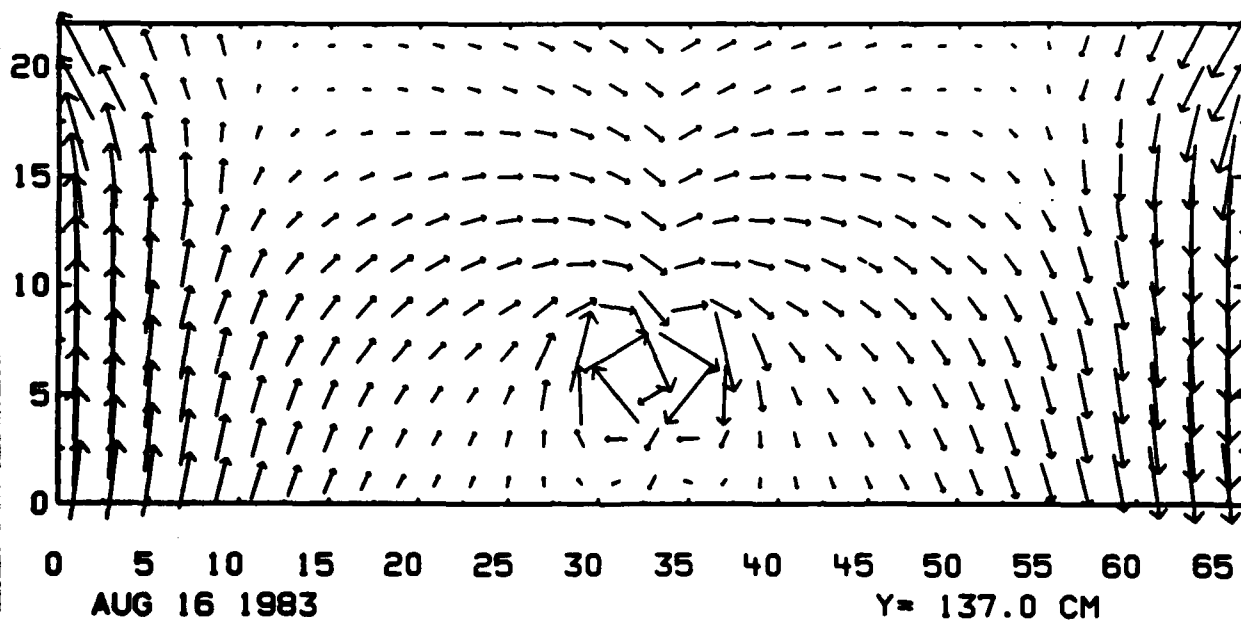AUG 16 1983   Y= 137.0 CM
    BAVE= 3.80E+00 GAUSS
    BMAX(32, 4) = 2.02E+01 GAUSS   T =   70.00 US
    BMIN(50,20) = 3.91E-01 GAUSS

LINEAR VECTORS AXIAL WIRE

0   5   10   15   20   25   30   35   40   45   50   55   60   65

AUG 16 1983   Y= 137.0 CM
    BAVE= 3.25E+00 GAUSS
    BMAX(64, 2) =   8.97E+00 GAUSS   T =   80.00 US
    BMIN(52,18) =   5.49E-01 GAUSS

Figure 5k, 1   26

PHYSICA D

NONLINEAR PHENOMENA

NONLINEAR INTERACTIONS DURING MAGNETIC FIELD-LINE RECONNECTION IN PLASMAS

R.L. STENZEL and W. GEKELMAN
Department of Physics, University of California, Los Angeles, CA 90024, USA

27

NONLINEAR INTERACTIONS DURING MAGNETIC FIELD-LINE RECONNECTION IN PLASMAS

R.L. STENZEL and W. GEKELMAN
Department of Physics, University of California, Los Angeles, CA 90024, USA

Stimulated by important dynamic processes in space and fusion plasmas, the reconnection of magnetic fields in plasmas is investigated. A well-controlled large laboratory plasma is established, and direct observations of magnetic fields and particle distributions are performed. High speed computers are interfaced with the experiment so as to permit the analysis of multidimensional functions. These include the average magnetic field topology $\langle B(r, t) \rangle$ and the tensor correlation function $\langle B_1 B_2 \rangle_{\omega, k}$ of magnetic fluctuations, as well as the electron phase space distribution function $f(v, r, t)$. The observations show that the characteristic field topology of a neutral sheet is subject to a high level of magnetic turbulence consisting of low frequency whistler waves. These are excited by anisotropies in the electron distribution functions inside the current sheet, in particular by energetic electrons which run away in the electric field along the separator. The observed microinstabilities and kinetic processes cannot be described by classical fluid theories or MHD simulations but are important in determining the effective resistivity and reconnection rate.

1. Introduction

Solar flares [1] and magnetic substorms [2] present examples from space plasma physics where a strong nonlinear interaction of magnetic fields with plasmas takes place. These dynamic processes are both characterized by a rapid energy transfer from stored magnetic field energy into plasma kinetic energy [3]. The events appear to violate the classical MHD picture which predicts that magnetic fields are essentially "frozen in" [4] highly conducting fluids and cannot be dissipated except in small regions near magnetic null points where finite resistivity permits diffusion, hence reconnection of field lines and dissipation [5]. The discrepancy between the observed impulsive energy exchange and the classical steady-state theories has long been recognized, and models for various plasma instabilities near null points have been proposed [6]. These involve either macroscopic changes in the magnetic field topology by tearing instabilities [7] or microscopic instabilities which generate small scale fluctuations and effectively enhance the plasma resistivity [8]. Either case leads to nonlinear phenomena since field and plasma

properties are highly coupled. In spite of many years of theoretical work, numerical simulation effort and observations from spacecraft, the complex reconnection process is still an open fundamental problem in plasma physics.

Its significance is not restricted to space plasmas. In various fusion devices such as tokamaks, reverse field pinches, spheromaks, and laser fusion, magnetic null point geometries arise [9]. In most confinement devices there is evidence that tearing instabilities lead to a loss of confinement of particles and energy even though the details are not known.

A common problem in fusion and space plasmas is the difficulty of making direct detailed observations of the reconnection processes near magnetic null points. The basic physical processes are best observed in a well-controlled laboratory plasma designed for optimizing diagnostic access. A large diameter discharge plasma has been used at UCLA for reconnection studies for several years [10–15].

Although one cannot model in a laboratory device global configurations of cosmic plasmas, the characteristic magnetic null point geometry can be

reproduced [16–18]. Here we will show the formation of a classical magnetic neutral sheet [5]. It presents the interface between two oppositely directed magnetic field regions, and it is maintained by a plasma current sheet. Its stability has been investigated and is found to contain a high level of magnetic turbulence. It consists of a broad spectrum of unstable whistler waves. The source of these instabilities lies in the non-equilibrium electron distribution function in the current sheet. Anisotropies in the form of runaway electron tails are observed from direct measurements of $f(v, r, t)$. The significance of these findings to the reconnection physics is twofold: (i) Non-Maxwellian distribution functions modify the classical transport parameters; for example, the effective resistivity is determined by the runaway electrons rather than the bulk electron "temperature". (ii) Velocity space instabilities create a high level of turbulence which interacts with resonant particles. These wave–particle interactions are outside the models described by MHD theory, yet may explain "anomalous" resistivities, enhanced reconnection, and energy transfer.

Most of the physical quantities measured in this experiment involve higher dimensions and multiple variables. In order to be able to investigate a wide parameter space the experiment has been interfaced with high speed computers. This approach opens a new dimension in experimental work. Without digital data processing it would be essentially impossible to investigate the seven-variable distribution function or the Fourier transformed cross-correlation tensor of magnetic fluctuations. We will display some of these functions in stereoscopic form; the details for viewing such figures are described in the appendix.

2. Experimental arrangement

The present reconnection experiment (see fig. 1) employs a linear discharge plasma column produced with a large diameter (1 meter) cathode [19]. Typical densities are $n_e \approx 10^{12}$ cm^{-3}, temperature

$kT_e \approx 10$ eV, axial magnetic fields $B_y \approx 10$ G. The plasma is uniform, quiescent, nearly collisionless, and highly reproducible in pulses of duration $t_p \approx 5$ ms repeated every $t_r \approx 2$ s. After establishing the plasma a time varying transverse magnetic field ($\langle B_\perp \rangle \approx 10$ G) is applied. Its topology in vacuum contains an X-type neutral point on the axis of the device (see fig. 1a). In the presence of the plasma electron currents ($I_p \approx 1000$ A) are induced which flow preferentially in regions of $B_\perp \approx 0$ but are sufficiently large to modify the applied field topology. During the period of rising magnetic fields ($0 < t < 100 \mu$s) the self-consistent field distribution is that of a classical neutral sheet [5]. The plasma current, driven by inductive and space charge electric fields, $E = -\dot{A} - \nabla \phi_p$, is mainly carried by electrons which drift from the cathode toward the end anode. The current closes via the grounded chamber wall to the cathode. No net currents flow to the insulated plates or to the radial chamber walls which are separated from the plasma by vacuum.

The plasma processes are analyzed with various probes which provide time and space resolved data. A digital data acquisition system consisting of 8 bit, 100 MHz analog-to-digital (A/D) converters, minicomputer (LSI 11/23), array processor and direct data link to large size computers (CDC 7600, Cray 1) is employed. Probes include magnetic loops, Langmuir probes, high-frequency rf probes, and a novel directional velocity analyzer [20]. In a typical magnetic field measurement the signals of orthogonal loops are recorded vs. time at 300 spatial locations. At each position the experiment is repeated up to 80 times so as to obtain statistical averages, i.e., mean, standard deviation, and correlation functions. Extensive space-time maps may involve > 100 million numbers which can only be handled by high speed computers.

3. Magnetic field topologies

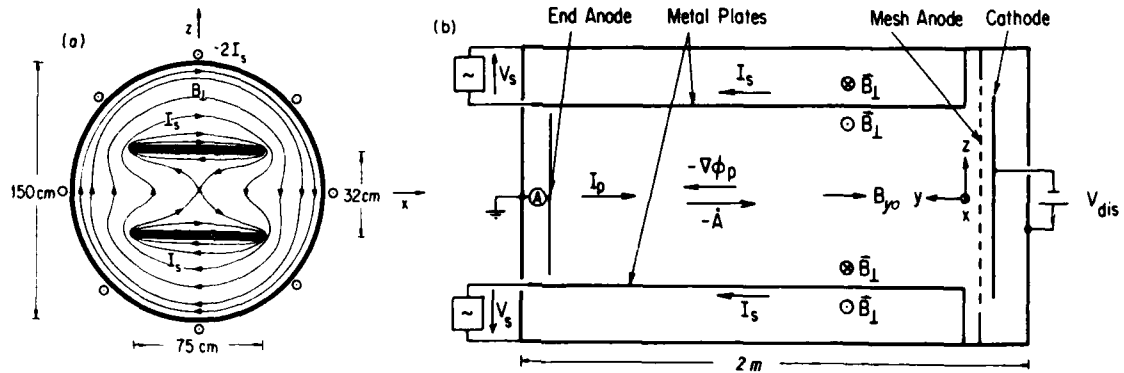A function of multiple variables such as the vector field $B(x, y, z, t)$ cannot be visualized at

Fig. 1. Schematic picture of the experimental arrangement. (a) Cross-sectional view showing parallel plate electrodes with pulsed currents I_s and magnetic field lines $B_\perp$ without plasma. (b) Side view of the device with main electrodes, currents (I_p, I_s) electric fields ($E = -\dot{A} - \nabla\phi_p$), and magnetic fields ($B = B_\perp + B_{y0}$). The coordinate system common in magnetospheric physics has been adopted where y is along the neutral line (device axis), x is along the horizontal neutral sheet, and z is normal to the sheet.

once but only in a reduced parameter space. We start to show the two-dimensional field $B_\perp = (B_x, B_z)$ in the transverse plane (x, z) at a given time t, ensemble averaged at each point over $N = 25$ repeated experiments. Fig. 2a depicts the field topology of a neutral sheet, the classical configuration treated in most steady-state theories of reconnection [21]. We observe this field pattern during the rise of the applied currents. The induced plasma current tends to slow down the penetration of the external field and its reconnection in the null region. The current sheet $J = \nabla \times B/\mu_0$ has a half width of $\Delta z \approx 3$ cm which is on the order of the collisionless skin depth $c/\omega_{pe} \approx 0.7$ cm. Current sheets investigated in space are often broader than an ion Larmor radius so that, in comparison, we are resolving the fine structure of current sheets. The field topology is macroscopically stable for many Alfvén transit times across the plasma ($t_A \approx 7\,\mu$s in He, 20 μs in Ar). However, in the case of very large current densities ($J \approx nev_e$) disruptive instabilities are observed [22]. These will not be considered in this paper.

In response to the induced currents and $J \times B$ forces, the plasma is vertically compressed and horizontally expelled. We have measured the fluid motion with orthogonal differential ion velocity analyzers [12]. Fig. 2b depicts the characteristic ion
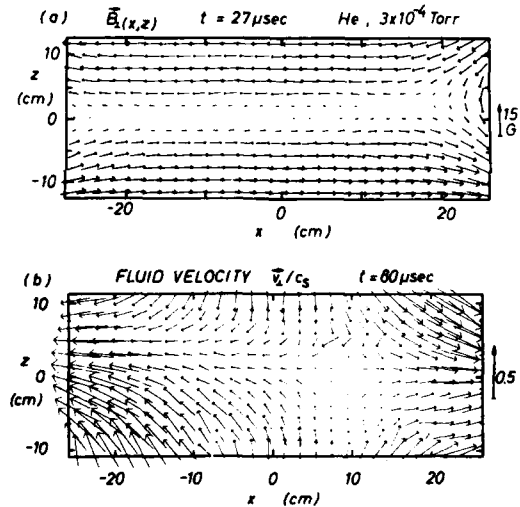

Fig. 2. Measured magnetic field and flow field during reconnection. (a) Transverse field $B_\perp(x, z)$ at a fixed time t, position $y = 137$ cm, showing the classical neutral sheet topology. (b) Transverse ion flow velocity, $v_\perp(x, z)$, normalized to the local sound or Alfvén speed, $C_s = (kT_e/m_i)^{1/2} \approx C_A = (B^2/2\mu_0 nm_i)^{1/2}$. Vertical compression and horizontal jetting are in qualitative agreement with reconnection models.

flow pattern which is observed to develop after an initial phase of turbulence. The measured flow field clearly shows the fluid jetting at Alfvénic speeds, which is predicted by theory and computer simulations [23] and thought to explain the generation

31

of high energy particles in solar flares and the magnetotail.

We now turn to the time dependence of the magnetic field topology. Two time scales can be distinguished: a slow one corresponding to the rise time of the external fields ($t \lesssim 100 \mu s$), and a fast time scale associated with fluctuations and instabilities. The slowly varying processes are well reproducible over repeated experiments. Thus, ensemble averages such as shown in fig. 2 are generated in typically 1024 successive, small time increments. The time evolution of the field topologies is then viewed in sequence in the form of a computer processed movie. Here, we can display only a few frames depicting the major features.

Fig. 3 shows magnetic field lines in the transverse x–z plane at three different time steps, $t = 57$, 58, and 59 μs. Instead of the vector field of fig. 2a, we have integrated the B field and display contours of constant vector potential, $A_y = $ const., where $B = \nabla \times A$. The motion of magnetic field lines through the plasma is best followed by the two inner field lines drawn heavier. With increasing time the opposing field lines move vertically ($\pm z$) towards the center, merge at the null point, and reconnect to form a new field line pair which moves horizontally ($\pm x$) outward. This process of field line reconnection occurs continuously during the external current rise. Magnetic flux generated at the two current carrying plates is transferred across the separatrix into regions of common flux where field lines encircle both current plates. During the current decrease the process reverses but the resultant vertical current sheet usually tears to form a large magnetic island [10]. The motion of field lines through plasmas is highly descriptive but becomes physically significant only through the coupling of plasma and field lines. However, near the null region, diffusion due to finite resistivity dominates. The field-line "velocity" is then a measure of the axial inductive electric field which is often taken as another measure for the reconnection rate [21]. The effective plasma resistivity is an important parameter since it determines the size of the diffusion region, the reconnection rate, and
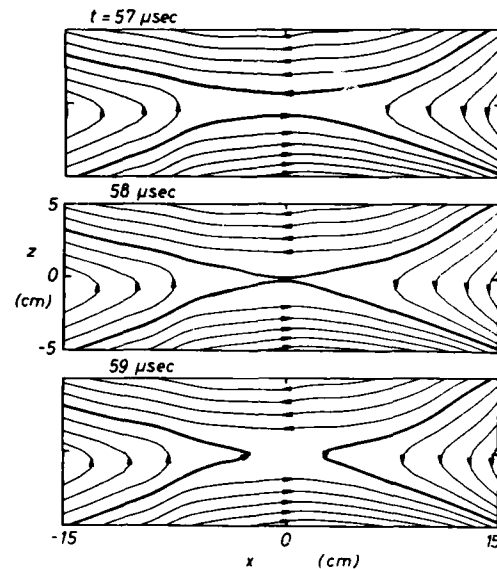

Fig. 3. Snapshots of magnetic field lines ($A_y = $ const.) during reconnection in a plasma. The two inner field lines merge and reconnect to form a pair of horizontally outward moving field lines. The entire time evolution has been displayed in a motion picture.

the plasma heating. Direct measurements of the resistivity [13] show a level well above the classical one, and an inhomogeneous pattern in the neutral sheet. These features may be understood after having discussed wave and particle measurements.

The present discussion was so far limited to the two-dimensional field topology. Because of the axial component B_{y0} the total magnetic field is three-dimensional, $B = (B_x, B_{y0}, B_z)$. Fig. 4 is a display of the three-dimensional vector field in the transverse plane $B_{(x,z)}$. It is presented as a picture pair for stereoscopic viewing, the techniques for which are explained in the appendix. The field lines are straight only in the current sheet, and exhibit increasing shear both above and below it. The neutral sheet is a null region only with respect to the transverse field ($B_x = B_z = 0$) but not the total field ($|B| = B_{y0} \approx 10$ G). Thus, the electrons in the current sheet always remain magnetized. In a different investigation we have varied the axial field strength from $B_{y0} = 0$ to $B_{y0} \gg |B_\perp|$ but here we limit ourselves to the case $B_{y0} \approx |B_\perp|$. Both in
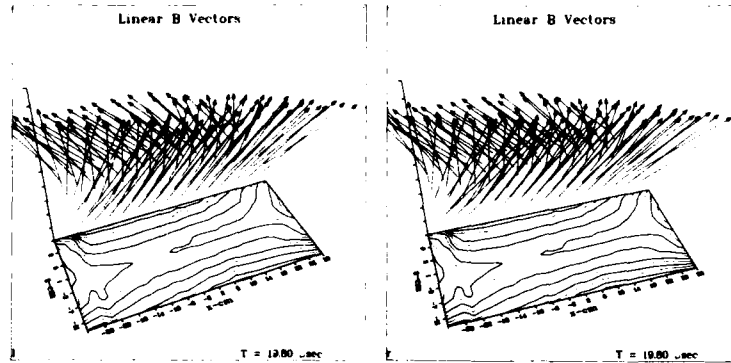
32

Fig. 4. Stereoscopic display of the three-dimensional vector magnetic field $B = (B_x, B_y, B_z)$ in the transverse $x - z$ plane. For reference, bottom plane gives a projection of the transverse field lines $A_y(x, z) = \text{const}$. ($y = 137$ cm). See appendix for viewing stereo pictures.

tokamaks and in the magnetosphere the fields are, in general, three-dimensional, while most theoretical models assume $B_y = 0$, for simplicity. When the axial field component is absent the magnetic field gradients are largest. Fig. 5 presents a stereoscopic view of the field strength $|B_\perp|_{(x,z)}$ along the neutral sheet which forms a deep long valley. In such inhomogeneous fields the particle orbits are, in general, nonadiabatic and the distributions are anisotropic [24].

We now turn to the rapidly varying magnetic field fluctuations ($\delta B/B \approx 10\%$). These result in rippled and distorted field lines. Although with a single probe we cannot map the instantaneous field lines, we can study the nature of the fluctuations statistically, e.g., by two-point cross-correlations. The first step in this investigation is to determine the fluctuation spectrum in terms of characteristic modes. Once the waves are identified the instability mechanism and the saturation processes have to be identified, which requires the knowledge of particle distributions. The final step is to assess the effect of the instability on the macroscopic plasma parameters, i.e., the transport properties.

Cross correlation studies are performed with two identical pairs of magnetic probes, one movable (# 1) and one stationary (# 2). At a given position an ensemble of $N = 80$ repeated mea-
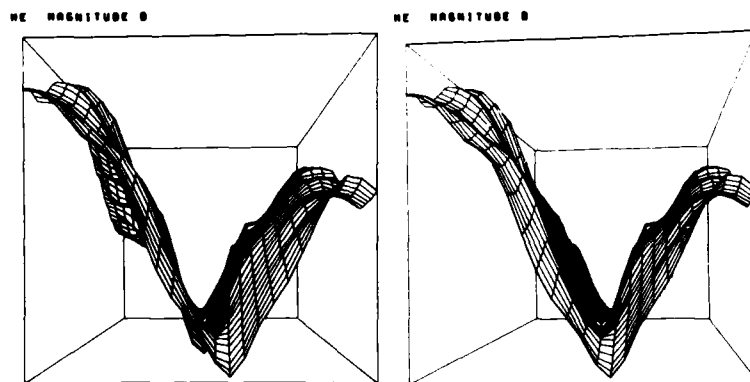

Fig. 5. Stereoscopic view of the transverse magnetic field strength $|B_\perp(x, z)|$ showing steep gradients adjacent to neutral sheet ($0 < B < 15$ G, $-25 < x < 25$ cm, $-12 < z < 12$ cm, $t = 25 \mu$s). See appendix for viewing stereo pictures.

33

surements of the vector components B_x, B_z is
recorded vs. time. Due to the slow time variation
the fluctuation processes are weakly nonstationary
so that statistical averages must be obtained by
ensemble averaging rather than time averaging
[25]. From the stored data we calculate on-line the
ensemble mean

$$\langle B \rangle = \frac{1}{N} \sum_{i=1}^{N} B_i, \tag{1}$$

the root mean square value of the fluctuations,

$$B_{rms} = \left(\frac{1}{N} \sum_{i=1}^{N} (B_i - \langle B \rangle)^2 \right)^{1/2}, \tag{2}$$

and the cross correlation function

$$\langle B_1 B_2 \rangle = \frac{1}{N} \sum_{i=1}^{N} (B_{i1} - \langle B_1 \rangle)(B_{i2} - \langle B_2 \rangle) \tag{3}$$

We note that the correlation of two vectors results
in a tensor of, at least, rank $R = 2$. Here, its

components are given by

$$\langle B_1 B_2 \rangle = \begin{pmatrix} \langle B_{x1} B_{x2} \rangle & \langle B_{x1} B_{z2} \rangle \\ \langle B_{z1} B_{x2} \rangle & \langle B_{z1} B_{z2} \rangle \end{pmatrix} \tag{4}$$

In order to identify the mode spectrum we Fourier
transform the time dependence of the fluctuations,
select a narrow spectral component, and analyze its
spatial properties. The resultant cross spectral
function is a function of probe separation
$\Delta r = (\Delta x, \Delta y, \Delta z)$, delay time τ between the two
probes, and a weaker function of the time t during
the reconnection process, $\langle B_1 B_2 \rangle_\omega (\Delta r, \tau, t)$.

In fig. 6 we display an example of a diagonal
tensor component $\langle B_{x1} B_{x2} \rangle$ in the axial x–y plane
at a given frequency ($\omega/2\pi = 1$ MHz), time
($t = 21.4 \, \mu s$), and delay time ($\tau = 1.3 \, \mu s$). The up-
per part of the figure shows a topological view of
the cross spectral function while the lower part
presents a corresponding contour plot. The dis-
plays on the right-and left-hand side are rotated by
$\approx 6°$ for purpose of stereoscopic viewing (see ap-
pendix A).

The measurement indicates that even at a
selected frequency a broad spectrum of spatial
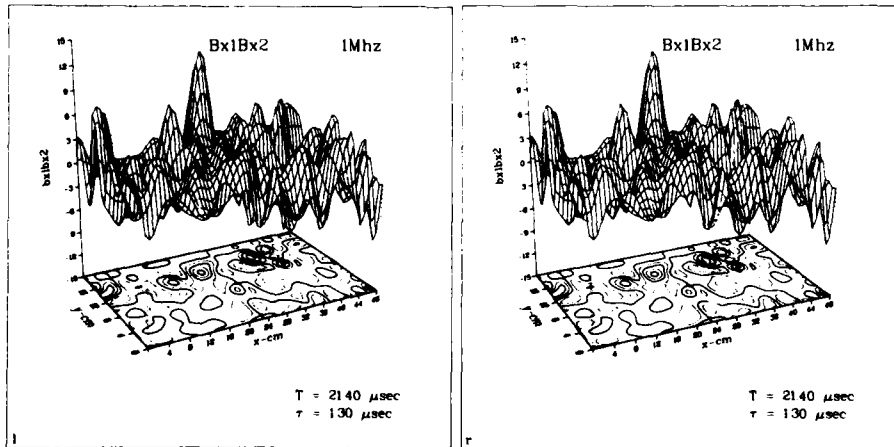modes is excited. This behavior is also found at

Fig. 6. Stereoscopic view of the cross-spectral tensor components $\langle B_{x1} B_{x2} \rangle_{(\Delta x, \Delta y)}$ of magnetic field fluctuations. The data are taken at $t = 21.4 \, \mu s$ during reconnection with $\tau = 1.3 \, \mu s$ time delay between the two probe signals, each filtered at $\omega/2\pi = 1$ MHz. A two-dimensional spatial mode spectrum is observed. See appendix for viewing stereo pictures.

other frequencies in the range investigated (100 kHz $< f <$ 1 MHz). The characteristic electromagnetic modes in this frequency band are the whistler waves [26]. These modes are not only dispersive ($\omega/k \neq$ const.) but also anisotropic, i.e., at a given ω the wave number k depends on the direction of wave propagation with respect to the magnetic field [$k = k(\theta)$]. From our cross-spectral measurements we can obtain the wavenumber spectrum by a spatial Fourier transformation from r-space into k-space. Since the time and space dependence is recorded the complex fast Fourier transform yields both magnitude and direction of k. Using the data from two orthogonal planes (x–y, x–z) we have constructed the three-dimensional wave vector spectrum from the two projections in the k_x–k_y and k_x–k_z planes.

An example of such data analysis is shown in fig. 7. It is a stereoscopic display of the dominant modes of $\langle B_{x1} B_{x2} \rangle_\omega$ in the full three-dimensional k space. The relative intensity of the modes is proportional to the dot size. A more detailed amplitude profile is provided by contour plots in the two orthogonal planes. In order to compare the measurements with theory we also display the wave vector surfaces $\pm k_{(\theta)}$ calculated from the dis-

persion relation for whistlers [26]

$$\left(\frac{kc}{\omega}\right)^2 = 1 - \frac{\omega_p^2}{\omega(\omega - \omega_c \cos \theta)}, \tag{5}$$

where $\omega/2\pi = 1$ MHz, electron plasma frequency $\omega_p/2\pi = 20$ GHz, and cyclotron frequency $\omega_c/2\pi = 28$ MHz are typical experimental parameters. One can see that the unstable modes fall close so the theoretical refractive index (kc/ω) surface for whistlers. An exact fit cannot be expected due to magnetic field and density inhomogeneities.

Besides the dispersion properties we have also investigated the polarization of the unstable modes. Theory predicts that the magnetic field of whistler waves has a right hand circular polarization [26]. By applying a digital filter to the measured k vector spectrum we select one mode at a time, inverse Fourier transform it, and inspect its space-time dependence ($\Delta r, \tau$). This procedure is applied to the two tensor components $\langle B_{x1} B_{x2} \rangle$ and $\langle B_{z1} B_{x2} \rangle$ which have two orthogonal components of vector B_1 correlated with the same reference signal B_{x2}. A display of $\langle B_1 B_{x2} \rangle$ versus τ at a given Δr (or vice versa) provides a hodogram which reveals the polarization.
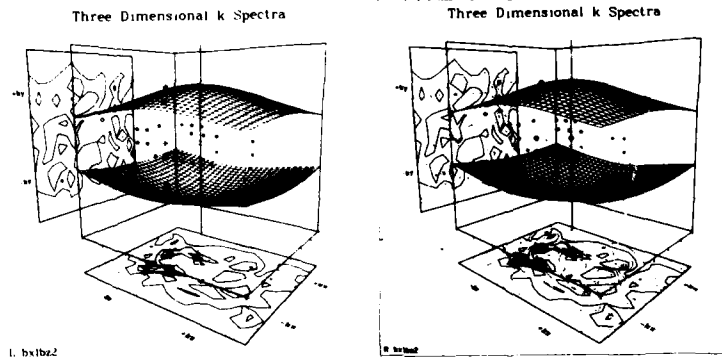

Fig. 7. Three-dimensional wavevector space (k_x, k_y, k_z) with measured modes of the cross-spectral function $\langle B_{x1} B_{x2} \rangle$ and the theoretical dispersion surfaces $\pm k_{(\theta)}$ for whistler waves ($\omega/2\pi = 1$ MHz, $\omega_c/2\pi = 28$ MHz, $\omega_p/2\pi = 20$ GHz). Vertical axis k_y is along average B_{y0}, origin $k = 0$ is indicated by square dot. The mode intensity is proportional to the dot size, the mode location k is constructed from measurements of $\langle B_{x1} B_{x2} \rangle$ in two orthogonal spatial planes, Fourier transformed into k planes and presented as contour plots adjacent to the k space. The observations indicate that the magnetic turbulence consists of oblique whistler modes. See appendix for viewing stereo pictures.

35

Fig. 8 is a stereoscopic view of the hodogram $\langle B_1 B_{x2} \rangle$ vs. τ for a mode propagating nearly along the average magnetic field. The helical trajectory indicates that the mode is essentially right-hand circularly polarized. However, for long delay times ($\tau \approx 3$ μs) phase mixing due to the finite filter bandwidth ($\Delta\omega/\omega \approx 10^{-1}$) tends to randomize the polarizations. For modes propagating at an angle to the magnetic field we first transform the wave B-field into a plane normal to k ($k \cdot B = 0$) and then inspect the polarization. Most modes which fall close to the dispersion surface are right-hand polarized.

Thus, from both the dispersion and polarization properties the eigenmodes which make up the magnetic field fluctuations are found to be whistler waves.

We will next investigate the cause for the instability of whistler waves. According to theoretical models, anisotropies in the electron velocity distribution can lead to whistler instabilities [27].

4. Distribution functions

The distribution of particles in velocity space v, real space r, and time t, $f(v, r, t)$, provides the fundamental description of plasmas on a mic-

roscopic level. All macroscopic plasma properties can be derived from it by forming moments, i.e., averages over the velocity distribution. Kinetic theories and numerical particle simulations all depend on the knowledge of the distribution function. In spite of the theoretical significance of this function there are, surprisingly, few experimental observations of, e.g., electron distributions in laboratory plasmas. In order to measure $f(v)$ a velocity analyzer with directional sensitivity is required. Such detectors are available for low density, high energy particles in space [28] but have only recently been developed for denser laboratory plasmas [20, 29].

Our electron detector consists of a small (3 mm radius) retarding potential velocity analyzer whose directional sensitivity ($\Delta\Omega \approx 4\pi \times 10^{-3}$ sterad) arises from filtering electrons through a microchannel plate. It can be rotated through the two spherical angles ($0 < \theta < \pi$, $0 < \phi < 2\pi$) so as to collect electrons from any direction in velocity space. The three-dimensional distribution function $f(v, \theta, \phi)$ is assembled from individual flux measurements at typically 200 different directions θ, ϕ. Furthermore, at each angular position the experiment is repeated N times so as to form the ensemble average $\langle f \rangle$ and standard deviation f_{rms}, analogous to the case of the magnetic field
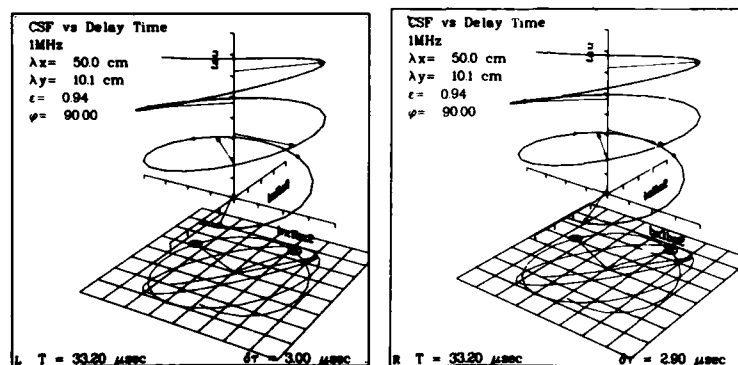

Fig. 8. Polarization properties of a single (ω, k) mode of the magnetic turbulence spectrum. With increasing delay time τ the correlation vector $\langle B_1, B_{22} \rangle$ rotates initially in a right-hand circular sense as expected for whistler waves ($\omega/2\pi = 1$ MHz). See appendix for viewing stereo pictures.
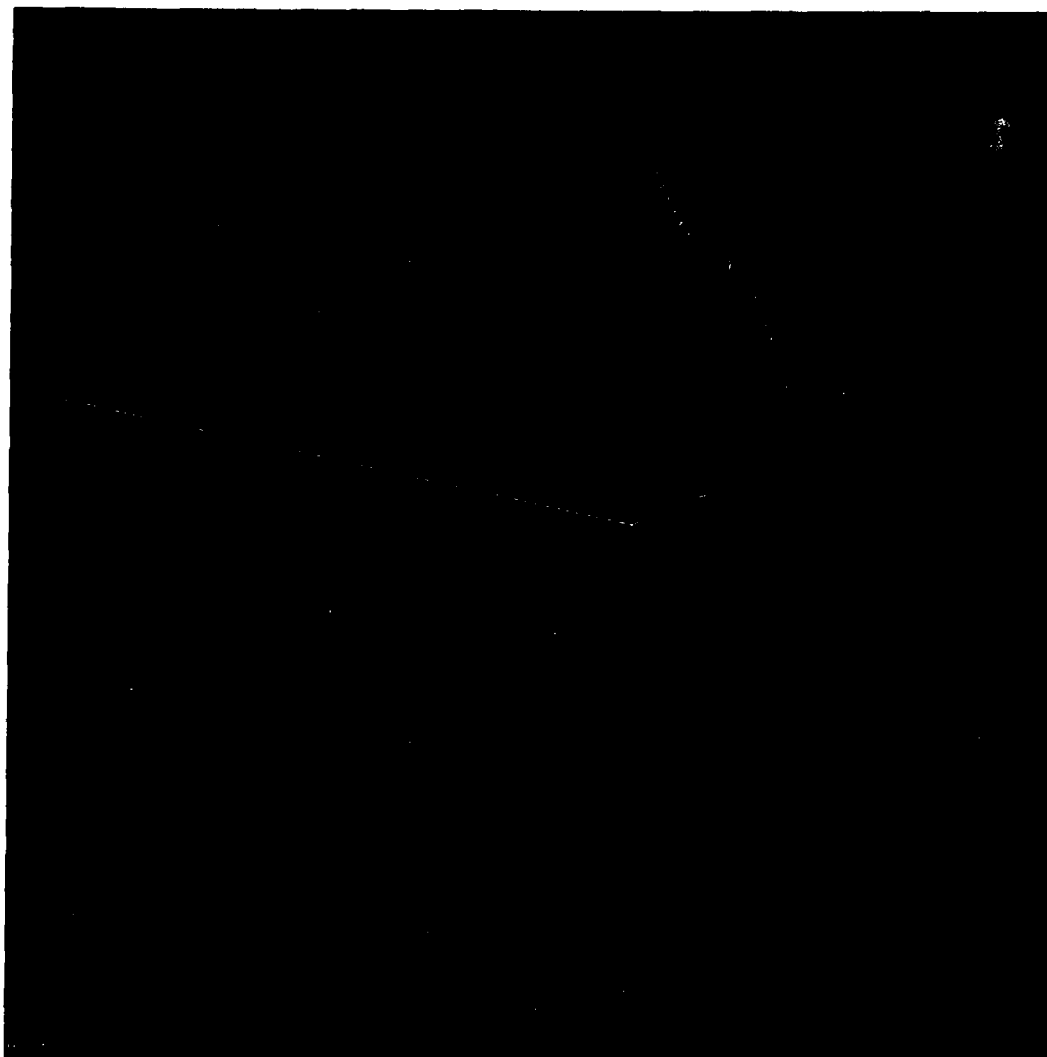
36

Fig. 12. Comparison between the average distribution function and its fluctuations in the neutral sheet.

Upper panel: Logarithmic display of the average value $<f(v_{\parallel}, v_{\perp})>$ and two one-dimensional cuts along $v_{\parallel} = v_y$ axis and $v_{\perp} = v_z$ axis. Note tail of runaway electrons. $[f(0,0) \cong 10^{14}$ cm^6 s^3; reference plane at $f = 10^{17}$ cm^6 s^3.]

Middle level: Contours of constant average $\log<f(v_{\parallel}, v_{\perp})>$ (3 dB contour spacing).

Bottom level: Contours of root-mean-square fluctuations $\log f_{rms}(v_{\parallel}, v_{\perp}) = $ const. (3 dB per contour, $f_{rms\,max}/<f_{max}> \cong 20\%$). Note large fluctuations in regions of runaway electron tails. $[0 \leqslant |v_{\parallel}|, |v_{\perp}| \leqslant 6 \times 10^8$ cm/s.]

37

measurements [see eqs. (1), (2)]. Besides the velocity space dependence we also measure the real space dependence by moving the analyzer to various positions in the neutral sheet. The measurements are also time resolved to within $\Delta t \approx 3\,\mu$s, the time required to sweep out the current–voltage characteristics. The data processing for a function of up to seven variables is made possible only through the use of high speed computers with large memory.

Fig. 9 presents measurements of the electron distribution function in velocity space. In two dimensions the distribution $f(v_x, v_y)$ can either be displayed topographically (fig. 9a) or as a contour plot (fig. 9b). In three-dimensional velocity space a display analogous to fig. 9a cannot be visualized but we can extend fig. 9b and plot surfaces of constant $f(v)$ as done in fig. 9c. The maximum value $f_{max} \approx 10^{-14}\,cm^{-6}\,s^3$ generates a surface near the origin. Decreasing values of $f(v)$ produce nested surfaces of expanding radius in velocity space, three of which are shown in fig. 9c where the outer surfaces are cut open for purpose of display. Using time as the variable f we have displayed the continuous variation $0 < f < f_{max}$ in a computer generated movie.

Anisotropic distribution functions exhibit non-spherical surfaces of $f(v) = $ const. Fig. 10 shows a stereoscopic view of a surface near the tail of the distribution. We choose to display $v^2 f(v) = $ const. rather than $f(v) = $ const. to stress the importance of a seemingly small tail (see fig. 9) on the moments of $f(v)$. The quantity displayed is the kernel for the zeroth moment, i.e., the density

$$n_e = \int f(v)\,dv = \int_0^{2\pi}\int_0^{\pi}\int_0^{\infty} v^2 f(v, \theta, \phi)\,dv\,\sin\theta\,d\theta\,d\phi .$$

(6)

Higher moments such as those leading to the current density $j = \int vf(v)\,dv$, mean energy $E = \int \frac{1}{2}mv^2 f(v)\,dv$, and heat flow $q = \int \frac{1}{2}mv^2 vf(v)\,dv$ involve progressively higher powers of v which puts a strong weight on the fast tail electrons. For example, integration over the distri-
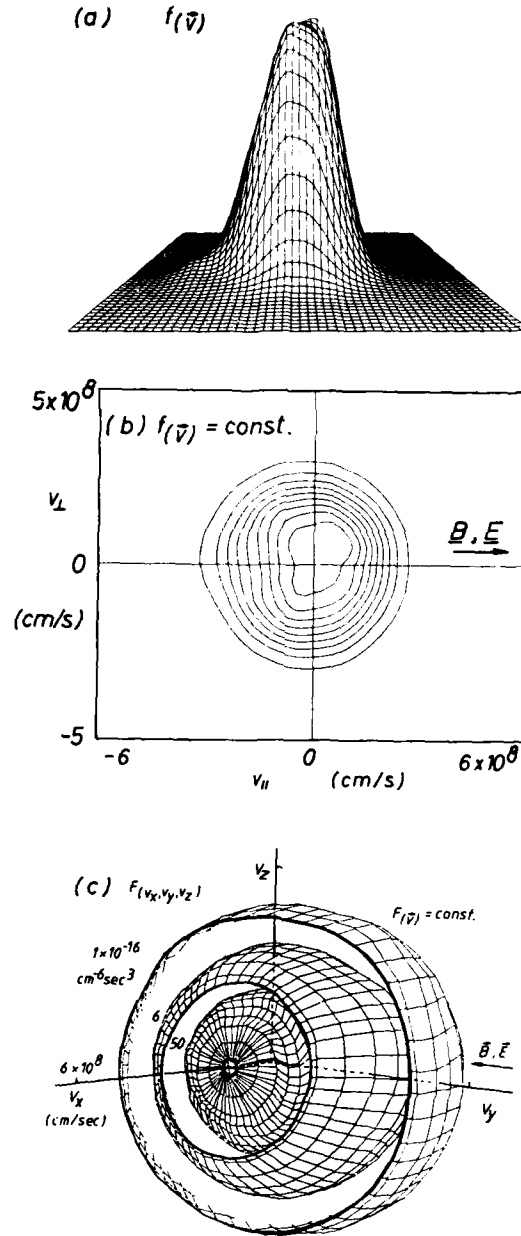

Fig. 9. Measured electron distribution function in the neutral sheet. (a) Linear display of $f(v_\|, v_\perp)$; $f_{(0,0)} \approx 10^{-14}\,cm^{-6}\,s^3$. (b) Contour plot $f(v_\|, v_\perp) = $ const.; $\Delta f/f_{max} = 10\%$ per contour. (c) Distribution function in three-dimensional velocity space displayed as surfaces of $f(v_x, v_y, v_z) = $ const. Outer surfaces are cut for purpose of display. Continuous variation of $0 < f < f_{max}$ has been displayed in a motion picture.
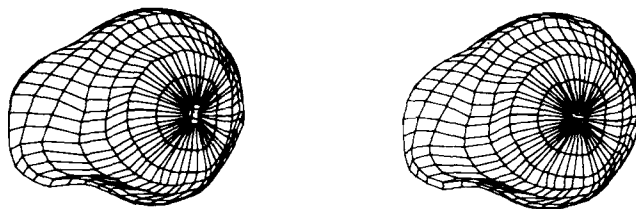
38

Fig. 10. Stereoscopic display of a surface $v^2f(v) = \text{const}$ (50 cm^{-4} s) in three-dimensional velocity space. The distortion on the left-hand side reflects an anisotropy caused by runaway electrons in the electric field $E_y | B_{y0}$ of the current sheet. v_z-axis along maximum protrusion to the left (180° rotation with respect to fig. 9c). See appendix for viewing stereo pictures.

bution function of fig. 9 reveals that the asymmetric tail electrons have a relative density $n_t/n_c \approx 10\%$, energy $E_t/E \approx 22\%$, and are responsible for the current and heat flow in the plasma which is at a small angle ($\Delta\theta \approx 15°$) with respect to the local magnetic field.

The distribution of figs. 9 and 10 are observed in the middle of the neutral sheet during recon-

nection. The tail of high energy (50–100 eV) electrons is thought to arise from the free acceleration of essentially collisionless tail electrons by the electric field E_y along B_{y0}. Outside the neutral sheet the transverse components ($B_x, B_z \neq 0$) prevent the free acceleration. This is clearly visible in fig. 11b which displays distribution functions, $\log f(v_y, v_z)$, at two different positions (x, z) pointed out by
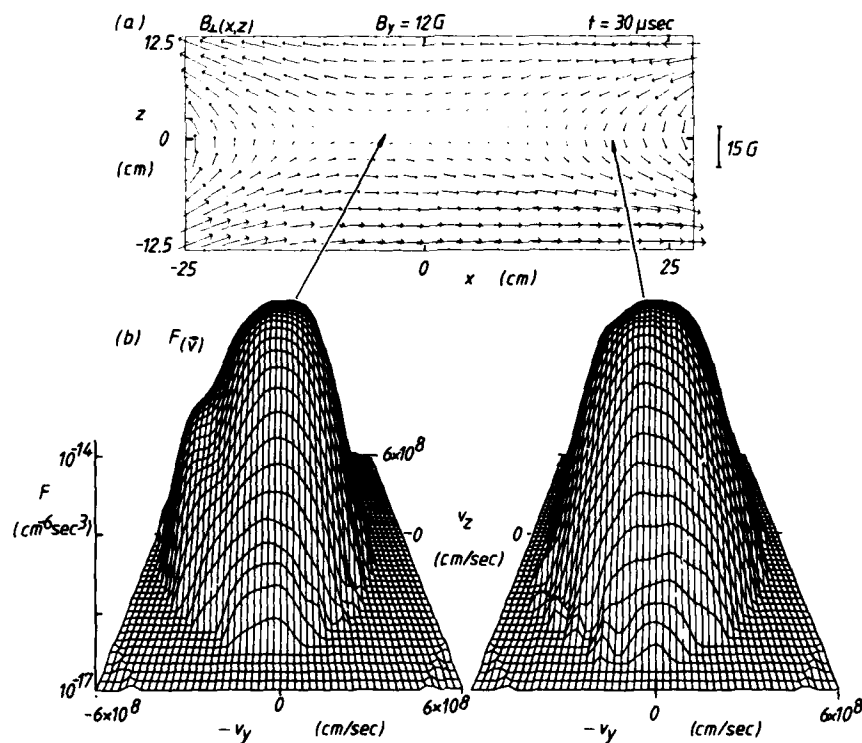

Fig. 11. Spatial variation of the distribution function in the neutral sheet. (a) Magnetic field topology with locations where $f(v)$ was measured. (b) Electron distribution $f(v_y, v_z)$ on a logarithmic scale with reference plane three orders of magnitude below the maximum. Note the presence of an energetic electron tail in the middle of the neutral sheet and absence of runaway electrons at the sheet edge.

arrows in the simultaneously measured magnetic field map $B_\perp(x, z)$ of fig. 11a. It is interesting to note that the bulk electron temperature is higher at the side of the neutral sheet than in the middle where the energy is transferred to runaway electrons.

The presence of runaway electron tails in a current carrying plasma can give rise to various kinetic instabilities. For example, the emission of plasma waves and lower hybrid waves in low density tokamak discharges is well known [30]. Auroral kilometric radiation is associated with energetic electron precipitation [31]. Oblique whistler waves can be excited by parallel beams [32]. Here, we are particularly interested in low frequency electromagnetic instabilities ($0.1 < f < 1$ MHz) in order to establish the relation with the observed unstable whistler modes. Whistler instabilities arise from wave-particle interactions by cyclotron resonance [$(\omega - n\omega_c)/k_\parallel \approx v_\parallel$] and Cerenkov resonance [$\omega/k_\parallel = v_\parallel$] [33]. We have, therefore, investigated low frequency fluctuations in the distribution function in the velocity regime satisfying wave–particle resonance.

Fig. 12 (color plate) displays in the bottom plane [$(v_\parallel, v_\perp) = (v_y, v_z)$] the rms fluctuations of the electron distribution, given by

$$f_{rms}(v) = \left\{ \frac{1}{N} \sum_{i=1}^{N} [f_i(v) - \langle f(v) \rangle]^2 \right\}^{1/2} \qquad (7)$$

The average distribution, $\langle f(v) \rangle = (1/N) \sum_{i=1}^{N} f_i(v)$, is shown for comparison as a contour plot in the middle plane and topographically in the upper plane. The distributions are displayed on a logarithmic scale so as to obtain a wide dynamic range in $f(v)$ (1000:1, 3 dB per contour, $f_{rms\,max}/\langle f(0) \rangle \approx 0.2$). The observations show that near the runaway electron tail of $\langle f(v) \rangle$ the fluctuation level is enhanced as expected from kinetic instability theories. The characteristic velocity of the tail particles is $v_\parallel \approx 3.5 \times 10^8$ cm/s close to the fundamental ($n = 1$) cyclotron resonance ($\omega_c/k_\parallel \approx 4 \times 10^8$ cm/s). Neither the second resonance ($n = 2$) nor the Cerenkov resonance

($n = 0$, $\omega/k_\parallel \approx 1.5 \times 10^7$ cm/s) involves a significant number of resonant particles. Thus, it appears that the tail electrons excite whistlers by cyclotron resonance. This plausible model awaits a final proof, i.e., the cross correlation between particle and wave fluctuations, $\langle \delta f \delta B \rangle$.

5. Discussion and conclusion

In the present experiment the classical reconnection problem has been investigated. Because of a well-controlled laboratory plasma, refined plasma diagnostics and the power of digital data processing we could extract information previously not available. We found that, to first order, the magnetic field topology and fluid flow are established in accord with theory. However, measurements of the resistivity and fluid acceleration showed orders of magnitude discrepancies with classical fluid parameters [12, 13]. A study of the microscopic processes such as fluctuations and distributions has been undertaken. The electron distribution in the current sheet is found to be anisotropic due to a tail of runaway electrons. This is a very important result since it shows that MHD theories break down in the neutral sheet. For example, the resistivity now is determined by the collisionality of the runaway electrons rather than the bulk electron temperature. The resistivity may become spatially very inhomogeneous due to changes in the distribution function.

Runaway electrons are a source of various microinstabilities one of which has been analyzed in great detail. The magnetic fluctuations have been identified from their dispersion and polarization to consist of a broad spectrum of whistler modes. The growth of the wave spectrum modifies, in turn, the electron distribution. The tail electrons lose some of their energy and momentum to the waves which results in an effective resistivity for the plasma current. The background electrons acquire energy through wave absorption which saturates the instabilities [34]. Ions are coupled to electrons by space charge electric fields.

Thus, the energy transfer during reconnection in collisionless plasmas involves various nonlinear wave–particle processes which cannot be analyzed in the framework of fluid theory. Refined experiments are necessary to clarify these "anomalous" transport processes.

Acknowledgments

Appendix A

In order to view figs. 4–8 and 10 stereoscopically, a simple viewing device is helpful. It consists of two identical lenses of focal length $f \approx 15\,cm$ and diameter $d \approx 2.5\,cm$, mounted approx. 7 cm apart and held about 10–15 cm symmetrically above the figure. A divider between the two figures and lenses may be helpful in separating the two images.

A commerically made inexpensive viewer has been purchased by the authors from the Taylor Merchant Corporation, 212 W. 35th Street, New York, N.Y. 10001 (Stereopticon Model 707).

References

[1] E.R. Priest, Solar Phys. 47 (1976) 41.
[2] S.-I. Akasofu, Physics of Magnetospheric Substorms (Reidel, Dordrecht, Holland, 1977).
[3] D.S. Spicer, Space Science Revs. 31 (1982) 351.
[4] H. Alfvén, J. Geophys. Res. 81 (1976) 4019.
[5] J.W. Dungey, Cosmic Electrodynamics (Cambridge Univ. Press, London, 1958).
[6] B.U.Ö. Sonnerup, in: Space Plasma Physics: The Study of the Solar System, vol. 2 (National Academy of Sciences, Washington D.C., 1979), p. 879.

[7] H.P. Furth, J. Killeen and M.N. Rosenbluth, Phys. Fluids 6 (1963) 459.
[8] R.W. Fredricks, Space Sci. Revs. 17 (1975) 449.
[9] T.J. Dolan, Fusion Research (Pergamon Press, New York, 1982).
[10] R.L. Stenzel and W. Gekelman, J. Geophys. Res. 86 (1981) 649.
[11] W. Gekelman and R.L. Stenzel, J. Geophys. Res. 86 (1981) 659.
[12] W. Gekelman, R.L. Stenzel and N. Wild, J. Geophys. Res. 87 (1982) 101.
[13] R.L. Stenzel, W. Gekelman and N. Wild, J. Geophys. Res. 87 (1982) 111.
[14] R.L. Stenzel, W. Gekelman and N. Wild, J. Geophys. Res. 88 (1983) 4793.
[15] W. Gekelman and R.L. Stenzel, UCLA Plasma Physics Group Report PPG 737 June 1983 (to appear in J. Geophys. Res.).
[16] P.J. Baum and A. Bratenahl, in: Advances in Electronics and Electron Physics, vol. 54, C. Marton, ed. (Academic Press, New York, 1980), pp. 1–67.
[17] A.G. Frank, in: Neutral Current Sheets in Plasmas, vol. 74, Proceedings of the P.N. Lebedev Physics Institute, N.G. Basov, ed. (Consultants Burea, New York, 1976), p. 107.
[18] N. Ohyabu, S. Okamura and N. Kawashima, J. Geophys. Res. 79 (1974) 1977.
[19] R.L. Stenzel and W.F. Daley, United States Patent No. 4,216,405, August 1980.
[20] R.L. Stenzel, W. Gekelman, N. Wild, J.M. Urrutia and D. Whelan, Rev. Sci. Instrum. 54 (1983) 1302.
[21] V.M. Vasyliunas, Rev. Geophys. Space Phys. 13 (1975) 303.
[22] R.L. Stenzel, W. Gekelman and N. Wild, Geophys. Res. Lett. 9 (1982) 680.
[23] T. Sato and T. Hayashi, Phys. Fluids 22 (1977) 1189.
[24] T.W. Speiser, Planet. Space Sci. 18 (1970) 613.
[25] J.S. Bendat and A.G. Piersol, Random Data: Analysis and Measurement Procedures (Wiley Interscience, New York, 1981).
[26] R.A. Helliwell, Whistlers and Related Ionospheric Phenomena (Stanford Univ. Press, Stanford, 1965).
[27] J.C. Lee and F.W. Crawford, J. Geophys. Res. 75 (1970) 85.
[28] T.R. Sanderson and J. Henrion, Space Science Instrum. 1 (1975) 351.
[29] R.L. Stenzel, R. Williams, R. Aguero, K. Kitazaki, A. Ling, T. McDonald and J. Spitzer, Rev. Sci. Instrum. 53 (1982) 1027.
[30] Z.G. An, C.S. Liu, Y.C. Lee and D.A. Boyd, Phys. Fluids 25 (1982) 997.
[31] J.E. Maggs, J. Geophys. Res. 83 (1978) 3173.
[32] H. Matsumoto and Y. Yasuda, Phys. Fluids 19 (1976) 1513.
[33] A.B. Mikhailovskii, Theory of Plasma Instabilities, vol. 1 (Consultants Bureau, New York, 1974).
[34] D.A. Whelan and R.L. Stenzel, Phys. Rev. Lett. 50 (1983) 1133.

Magnetic Field Line Reconnection Experiments
6.   Magnetic Turbulence

W. GEKELMAN AND R. L. STENZEL
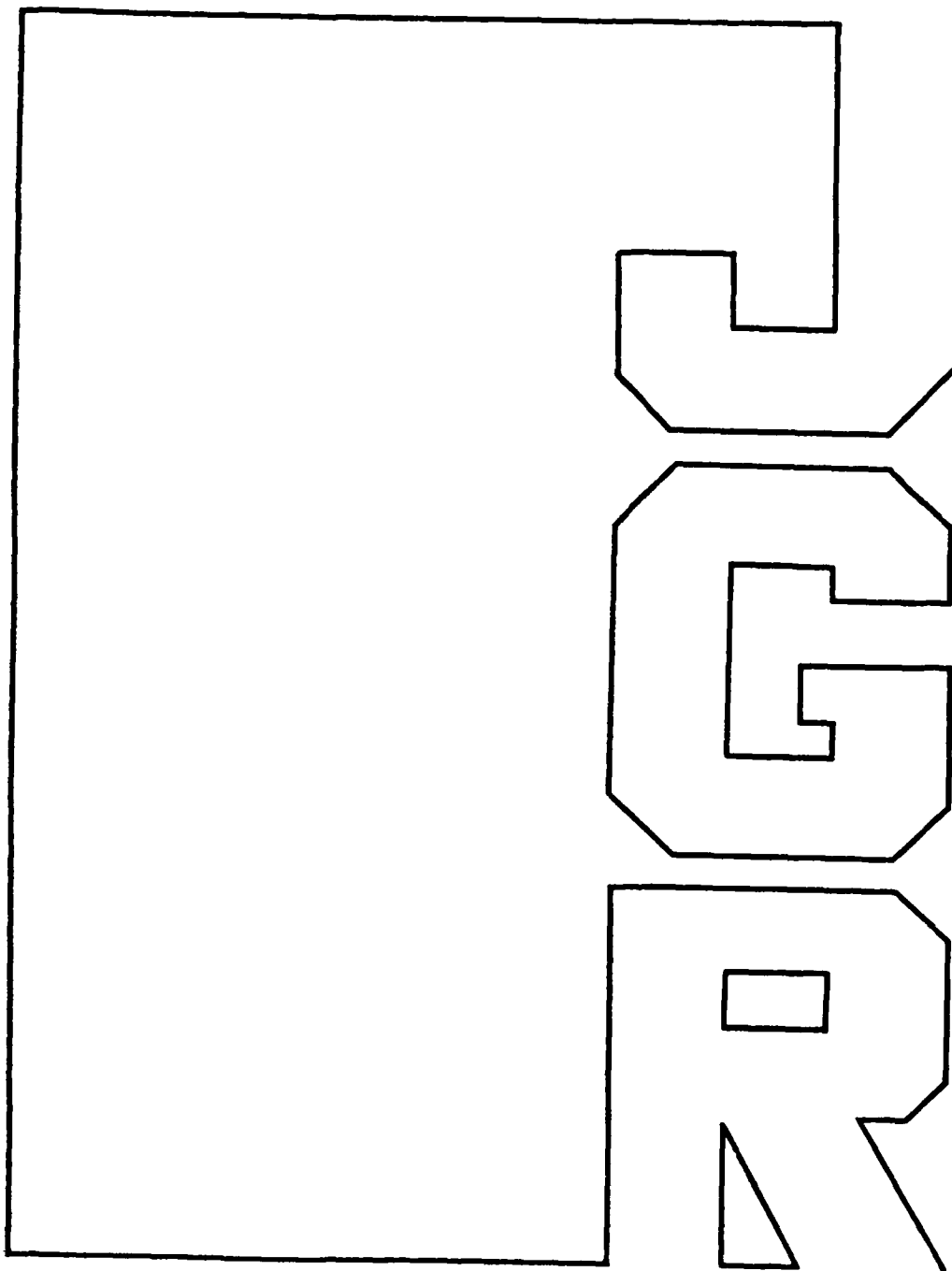
Magnetic Field Line Reconnection Experiments
6. Magnetic Turbulence

W. Gekelman and R. L. Stenzel

Department of Physics, University of California, Los Angeles

Extensive statistical analysis of the vector components of fluctuating magnetic fields have been performed in a time dependent neutral magnetic sheet. Cross spectral analysis indicates a variety of wave numbers present for each frequency investigated. Comparison of Fourier components of the cross spectral function with dispersion surfaces in **k** space demonstrates the waves are large amplitude whistlers; this is verified by polarization analysis, which shows the random waves' magnetic fields to be right-hand circular. Ion acoustic and Langmuir turbulence are also observed along with bursts of microwave radiation. Measurements of the electron distribution function $f(\mathbf{v}, \mathbf{r}, t)$ and its fluctuations in velocity space relate wave and particle activity.

Introduction

Fluctuations are a pervasive property of any active medium. Noise that may be considered to be a superposition of many waves has been long observed in both laboratory and space plasmas. When free energy is available, as in a non-Maxwellian particle distribution, wave amplitudes can grow and turbulence ensues.

Magnetic fluctuations have been observed by satellites in the plasma sheet and its boundary layer [*McFerron*, 1979] and in the magnetopause [*Sonnerup*, 1976; *Russell and Elphic*, 1978; *Gurnett et al.*, 1979a; *Anderson et al.*, 1982]. "Lion roars" or intense bursts of electromagnetic radiation have been explored in the magnetosheath [*Tsurutani et al.*, 1982; *Sudan and Denavit*, 1973] and have been identified as whistler waves [*Smith and Tsurutani*, 1976]. In addition, whistlers have been observed in the bow shock [*Coroniti et al.*, 1982]. Satellites have detected fluctuating magnetic fields in the magnetosphere [*Russell et al.*, 1972]. The Voyager 1 spacecraft data established the presence of whistler waves in the Jovian magnetosphere [*Scarf and Gurnett*, 1977]. These waves may be caused by a powerful perturbation such as a lightning stroke [*Gurnett et al.*, 1979b] or by an anisotropy in the electron distribution function [*Sentman et al.*, 1983]. The underlying physics of whistler waves has been treated in the classical works of *Storey* [1953] and *Helliwell* [1965].

The electron distribution function in a current carrying plasma may often develop into non-Maxwellian; such a plasma is subject to a variety of instabilities [*Kadomtsev*, 1965]. The ion acoustic instability and ion sound turbulence has been extensively investigated in the laboratory [*Gekelman and Stenzel*, 1978, and references therein] and observed in the solar wind [*Gurnett and Frank*, 1978].

In this paper we wish to report observations of these instabilities as well as Langmuir turbulence in a magnetic field line reconnection experiment containing a neutral sheet. Although these waves are not unique to the present magnetic field topology, they are a natural consequence of the currents along the neutral sheet and the anisotropic distribution functions therein. These, in turn, are in part due to the sheared magnetic fields. Once these waves become unstable their feedback onto

the reconnection event is quite important. Ion sound turbulence can cause turbulent electron heating [*Dum*, 1978] and dramatically raise the resistivity above the classical Spitzer value in the reconnection region [*Wild et al.*, 1981]. In these experiments the Hall term (**V** × **B**) in Ohm's law was measured and found to be negligible with respect to other terms. An estimate of the inertial conductivity places it orders of magnitude larger than that due to Coulomb oscillations. The resistivity governs the reconnection rate [*Vasyliunas*, 1975; *Sonnerup*, 1979]; in fact, without finite resistivity, the field lines, in accord with Maxwell's equations, would pile up at the separatrix and never reconnect at all. To simulate reconnection on computers, ad hoc resistivities are introduced [*Sato and Hasegawa*, 1982] and are required for theoretical tearing mode calculations [*Furth et al.*, 1963].

The fluctuating magnetic fields associated with the turbulent whistlers affect the electron orbits. Although the ions near the neutral sheet are essentially unmagnetized, they are coupled to the electrons through space charge fields such that the ion collision rate may become anomalously high [*Stenzel and Gekelman*, 1981a].

In a controlled laboratory experiment it is possible to study the structure of the magnetic and electrostatic turbulence in great detail. The variety of things happening simultaneously in a turbulent plasma implies that an overwhelming amount of data must be taken to sort them out. The introduction of relatively inexpensive, fast computers has led to a quantum jump in what is possible experimentally. Fully three-dimensional measurements of the electron velocity distribution have been performed [*Stenzel et al.*, 1983a] and will be discussed here and in a forthcoming paper in this journal. We point out that spacecraft measuring wave activity detect the waves at a Doppler shifted frequency owing to a combination of their motion and possible fluid drifts relative to the earth. Single probes take data at one spatial location and cannot determine the wave number spectra from correlation analyses such as those reported in this work.

The present reconnection experiment has already shown detailed diagnostics of the space time evolution of the magnetic fields [*Stenzel and Gekelman*, 1981b], the plasma parameters [*Gekelman and Stenzel*, 1981], the fluid dynamics [*Gekelman et al.*, 1982a], the energy flow [*Stenzel et al.*, 1982], and current disruptions with double layer formations [*Stenzel et al.*, 1983b]. These will be referred to throughout the text as JGR parts 1–5. An overall review of these experiments is given in a recent issue of *Physica Scripta* [*Gekelman et al.*, 1982b].
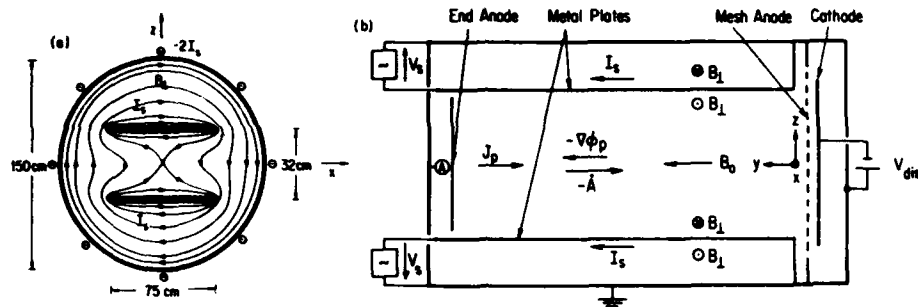
Fig. 1. Schematic view of the experimental device. (a) Cross-sectional view with transverse magnetic field line pattern in vacuum. (b) Side view with characteristic fields and currents. Note that the axis of the device is in the y direction while the transverse coordinates are x, z, as customary in magnetospheric physics.

EXPERIMENTAL ARRANGEMENT

The reconnection experiments are performed in a cylindrical vacuum chamber (1.5-m diameter, 2-m length) in which a low pressure ($p \lesssim 10^{-4}$ torr, A, H_2, He) discharge is produced with a 1-m diameter oxide-coated cathode (Figure 1). The emission properties of such special cathodes [Stenzel and Daley, 1980] provide a high-quality laboratory plasma of the following properties: Uniformity over large scale lengths ($\Delta n/n \simeq 10\%$ over 80 cm across B_0, 180 cm along B_0), nearly collisionless, high beta parameters (density $n_e \approx 10^{12}$ cm^{-3}, temperature $kT_e \simeq 10$ eV, electron-ion mean free path $l_{ei} \simeq 200$ cm, axial magnetic field $B_{y0} \simeq 12$ G, $\beta = nkT(B^2/2\mu_0) \simeq 2$), high repetition rate ($t_{rep} \simeq 2$ s), and good reproducibility ($\delta n/n \lesssim 5\%$) of the pulsed discharge ($V_{dis} \simeq 40$ V, $I_{dis} \simeq 1500$ A, $t_{dis} \simeq 5$ ms). The discharge pulse length is more than sufficient to reach steady-state plasma conditions, at which time the reconnection experiment is initiated. This involves establishing a transverse magnetic field $\mathbf{B}_\perp = (B_x, B_z)$ with a null point. Note that we have adopted x, y, z coordinates commonly used for the magnetotail where the y direction is along the separator, x is along the neutral sheet, and z is normal to it. A large sinusoidal current pulse ($I_s \simeq 20$ kA, rise time $t_r \simeq 100$ μs) is drawn axially through two parallel aluminum plates (75 cm wide, 33 cm spacing, 180 cm length) located on top and bottom of the plasma column. The plates are insulated from the plasma, which is confined to the space between them. Axial and average transverse magnetic fields are of comparable strength.

The transverse magnetic field geometry in vacuum is shown schematically in the cross sectional view of the device (Figure 1a). Without plasma there is an X type neutral point on the axis of the device. However, with plasma, axial plasma currents are induced ($I_p \gtrsim 1000$ A) that modify the magnetic field topology. The self-consistent current distribution and field topology can result in the formation of a classical neutral sheet [Dungey, 1958]. The plasma current driven by inductive and space charge electric fields ($\mathbf{E} = -\dot{\mathbf{A}} - \nabla\phi_p$) is mainly carried by the electrons. During the initial phase of external current rise ($dI_s/dt > 0$, $0 < t \lesssim 100$ μs) the electrons drift from the cathode toward the end anode. The current closes via the grounded chamber walls to the cathode. No net current flows to the insulated plates or to the radial chamber walls which are well separated from the plasma column.

The cathode emits as many electrons as are collected at the end plate so as to maintain approximate space charge neutrality prior to the reconnection event. However, as the applied inductive electric field ($\dot{A} \lesssim 0.5$ V/cm) can exceed the

classical runaway field [Dreicer, 1959] ($E_r \simeq m_e v_{ei} v_e/e \simeq 0.1$ V/cm, where $v_e^2 = 2kT_e/m_e$) and since the space charge limited emission [Langmuir, 1929] does not provide for current densities $j \gtrsim nev_e$ the plasma sets up an axial space charge electric field $-\nabla\phi_p$ opposite to the induced field. This shielding effect limits the electron drift to $v_d < v_e$, at least on the average over the entire plasma cross section. However, by decreasing the plasma density, the space charge contribution may be substantially lessened.

The evaluation of statistical quantities such as rms field fluctuations and correlation tensors is made possible through a data acquisition system and processor. The wave forms are digitized by fast (Transiac 100 MHz, LeCroy 20 MHz) analog to digital (A/D) converters that are controlled by an LSI 11/23 computer. The computer also drives stepping motors that position probes within the device. The computer is too slow to perform the necessary arithmetic such as fast Fourier transforms, digital filtering, and correlations during the 1.5 s between shots. An array processor (CSPI Map 200), therefore, has been interfaced to the computer. Upon performing all the calculations, the MAP places the results in the core of the LSI 11; it is subsequently placed on disc. Upon completion of a data run the final data set is shipped via a direct link to large (Cray, CDC 7600) offsite computers.

PREVIOUS EXPERIMENTAL RESULTS

Before addressing ourselves to fluctuations it is helpful to review the average magnetic field topology (part 1) as well as other macroscopic properties. Plate 1 is a stereo slide pair that should be examined with a proper viewer. (Note: Plates 1-3, Plates 5 and 6, and Figure 15 are best viewed in three dimensions because of the complexity of the data. This may be accomplished with a viewer available through the Taylor Merchant Corporation, 212 W. 35 Street, New York, New York 10001 (Stereopticon 707). One may be constructed out of two 14-cm focal length, 2.5-cm diameter lenses and cardboard. The lens centers should be placed 7 cm apart and 13.5 cm above the page, with a cardboard divider midway between them. Color reprints of this article and viewers are available for $4.50 U.S., in care of the authors at Department of Physics, University of California, Los Angeles, 405 Hilgard Avenue, Los Angeles, California 90024.)

The vector potential has an axial component $A_y = \int B_z dx - \int B_x dz$, $\partial/\partial y \simeq 0$, which is calculated from the transverse components of the magnetic field and displayed on the lower x-z plane. Small (1 cm in diameter) orthogonal magnetic loops

(a)

(b) 1 shot   x = 4cm, z = -4cm

(c) 3 shots ⊢ 1G ⊣

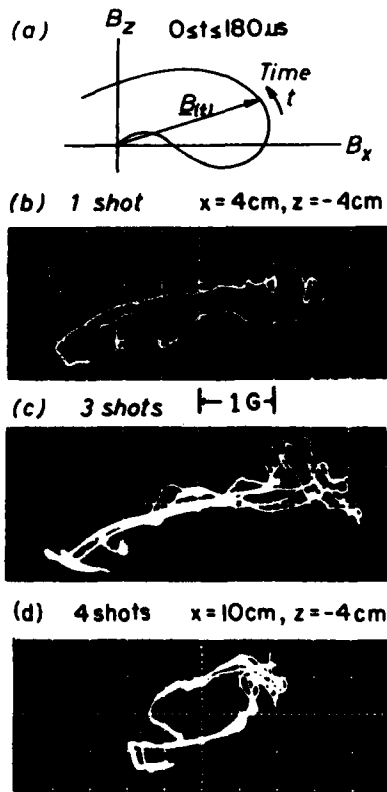**(d) 4 shots   x = 10cm, z = -4cm**

Fig. 2. (a) Schematic view of recording the magnetic field versus time in form of a hodogram. (b) Single shot hodogram taken near the neutral sheet identifies the fluctuations as loops, i.e., a rotating field component associated with hydromagnetic waves. (c) Superposition of three hodograms taken at same position as (b) shows dominance of magnetic fluctuations. (d) Superposition of four hodograms when probe is removed from neutral sheet region. He 3×10^{-4} torr, $B_{yo} = 20$ G, $y = 0$.

detect the changing **B** field, which is recorded at each of 300 spatial locations (x, z) as a function of time (1024 time steps, $\Delta t = 100$ ns) and averaged over an ensemble of 25 shots. One sees that a classical neutral sheet topology, associated with an axial current sheet, $J_y = (\nabla \times \mathbf{B}_\perp)/\mu_0$, has been formed.

Superimposed upon the transverse magnetic field is a constant axial bias field ($B_{yo} = 12$ G) such that the total magnetic field is sheared. This is illustrated as a three-dimensional vector field $\mathbf{B}(x, y, z) = \mathbf{B}_{yo} + \mathbf{B}_\perp$ in Plate 1. For clarity, only a fraction of the vectors are plotted. In the center of the neutral sheet the vectors are vertical since the transverse component of **B** vanishes, and at the boundaries ($z = \pm 12$ cm) the vectors are inclined at 45° since $B_\perp \simeq B_{yo}$.

From rapidly swept planar Langmuir probe traces analyzed with our digital data acquisition system, the ensemble averaged density and electron temperatures are mapped as a function of space and time (part 2). The electron temperature increases strongly but nonuniformly during the reconnection process, ranging from $T_e \simeq 5$ eV in the center of the neutral sheet to $T_e \simeq 15$ eV in argon (30 eV in helium) near the horizontal edges of the neutral sheet. A density minimum develops in the center of the neutral sheet ($n_e \lesssim 10^{12}/\mathrm{cm}^3$) and maxima ($n_e \approx 2 \times 10^{12}/\mathrm{cm}^3$) near horizontal edges of the neutral sheet. By combining density and temperature to form the plasma pressure we found that the forces on the fluid are not in balance ($\mathbf{J} \times \mathbf{B} - \nabla p \neq 0$). This leads to an acceleration and jetting of fluid from the neutral sheet. The resulting flow fields were measured with differential ion velocity analyzers (part 3) and found to be highly turbulent in space and time during the first 30 μs of the experiment when the induced electric field is large. When the turbulence level has decreased (the neutral sheet topology is present throughout this time) the classical $\mathbf{J} \times \mathbf{B}$ flow establishes itself with inflow velocities $v_z \simeq 0.2\ v_A$ and outflow velocities $v_x \simeq 0.5\ v_A$, where v_A is the local Alfvén speed based on the total magnetic field. From the measured fluid flow, pressure, fields, and currents we have quantitatively obtained the phenomenological scattering term $\Delta f = mnv^*\mathbf{v}$ in
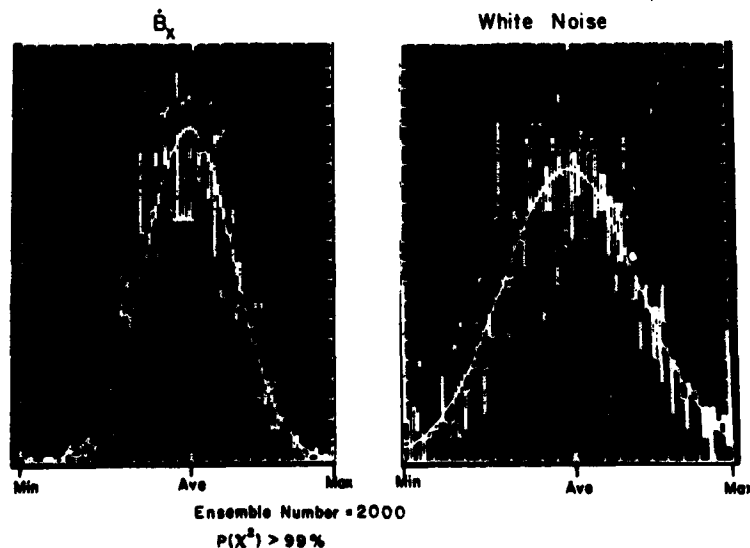
HISTOGRAMS

Ensemble Number = 2000

$P(X^2) > 99\%$

Fig. 3. Histograms, which compare the number of occurrences of a fluctuation as a function of its amplitude, are displayed for the magnetic field $\dot{B}_x$, and white noise using an ensemble of 2000 events. Both variables may be fit to the superimposed Gaussian distributions with 99% confidence.

47

the fluid equation

$$mn \frac{d\mathbf{v}}{dt} = (\mathbf{J} \times \mathbf{B} - \nabla p) - \Delta \mathbf{f} \qquad (1)$$

The components of the collision tensor $\mathbf{v}^*$ were evaluated and found to be large within the neutral sheet during times of turbulent flow and subsequently vanish.

MAGNETIC FIELD FLUCTUATIONS

Although the initial plasma parameters and applied currents are highly reproducible from shot to shot, we observe magnetic field fluctuations inside the plasma. Figure 2 shows a magnetic field hodogram, i.e., the trajectory of the vector tip $\mathbf{B}_\perp$ versus time during a 180-μs time interval. Just as in a satellite measurement, the hodogram is taken at a single spatial position that, in Figures 2b and 2c, is within the neutral sheet where the noise is largest. The fluctuations manifest themselves, in part, as small loops in the vector plot (Figure 2b). These can be interpreted as a rapidly rotating magnetic field component associated with a wave. The random nature of these waves is evident in Figure 2c, which has hodograms from three repeated events superimposed. At this location the fluctuations are comparable to the average value of $B_\perp$. If the probe is removed from the neutral sheet (Figure 2d) the irreproducible segment of the hodogram collapses. From Figures 2b and 2c one can estimate the fluctuating magnetic field to be of order 1–2 G and, therefore, $\delta B/B_{\text{TOTAL}} = 10$–20%.

The spatial properties of the fluctuations within one shot cannot be explored with a single probe. Correlation functions that require taking a large number of shots at many positions necessitate the use of a digital data acquisition system. For example, we have recorded 25 shots of $\mathbf{B}(t)$ at each of 300
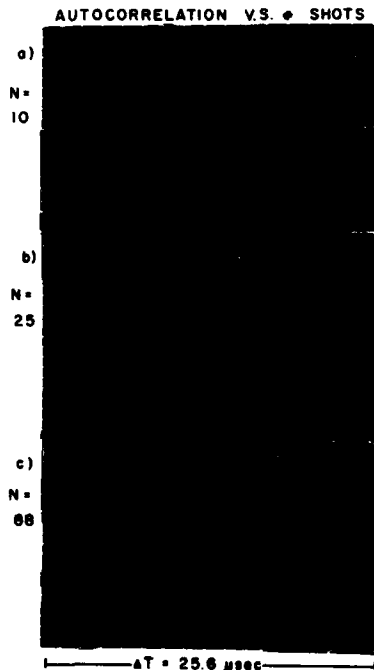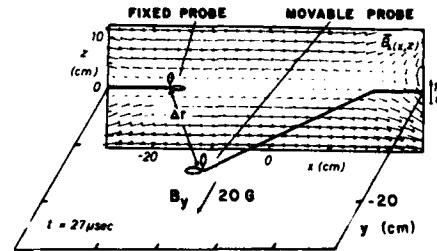
Fig. 5. Schematic of probe arrangement for correlation measurements. A fixed reference probe is located in the x, z plane at y = 0 cm. A second probe is mounted to move in the x-z plane ($x > x_{\text{fixed}}$, y = 0, -12 cm $\leq z \leq 12$ cm) or in the x, y plane ($x > x_{\text{fixed}}$, -26 cm $< y < +26$ cm, z = 0). For reference a linear vector plot of $\mathbf{B}_\perp$ is placed in the x, z, y = 0 cm plane. He 3×10^{-4} torr, $B_{y0} = 20$ G, $t = 27$ μs. The current carrying sheets are located at $z = \pm 16$ cm. The cathode is located at y = -137 cm.

positions and calculated on-line both the ensemble mean values of the field magnitude $\langle B_\perp \rangle$, direction $\langle \theta \rangle$ and the root mean square values B_{rms} and θ_{rms}. The rms fluctuation or autocorrelation that contains all frequencies within the probe and amplifier bandwidth (1 kHz $\leq f \leq$ 2 MHz) maximizes within the neutral sheet, which is also the location of large current density. These are of order $B_{\text{rms}}/\langle B_\perp \rangle \simeq 1$. The spatial extent of the magnetic waves is frequency dependent; for 1 MHz the disturbance fills the entire transverse plane.

NONSTATIONARY TURBULENCE

Since the magnetic turbulence affects the particle motion and ultimately the transport properties, detailed studies of it have been undertaken. The analysis involves measurements of cross correlation functions. If the time averaged mean value of a fluctuating magnetic field $\langle B(t) \rangle$ is independent of the choice of the averaging interval, the random variable $B(t)$ is stationary. In this case the correlation function may be calculated from a sufficiently long temporal record of each field component. If a single damped mode is a part of the random variable, there exists a technique developed by *Matthaeus and Goldstein* [1982] that subtracts this mode and treats the remainder as stationary noise. A process is called weakly non-stationary when the mean values of $\mathbf{B}(x, y, z)$ change slowly in comparison with the fluctuation frequencies as the neutral sheet is formed. For nonstationary processes the statistical properties such as correlation functions must be calculated from ensembles of random events that we establish by repeating the experiment under identical initial conditions.

Each component of the fluctuating magnetic field is a random variable whose probability distribution should approach a Gaussian with increasing number of events [*Loeve*, 1960]. This basic property has been verified by generating a histogram of $\dot{B}_x$, taken by a probe in the center of the neutral sheet, shown in Figure 3a, for an ensemble of 2000 events. Superimposed on the data is a Gaussian distribution with the same mean and standard deviation. A chi square test [*Taylor*, 1982] indicates the distribution of $\dot{B}_x$ to be normal with a 99% probability. Shown in the adjacent Figure 3b is the result using white noise as the input signal, which is essentially identical to that of $\dot{B}_x$.

In evaluating the correlation functions, one must determine how many events constitute an adequate ensemble. The result determines the data acquisition time and required computer memory.
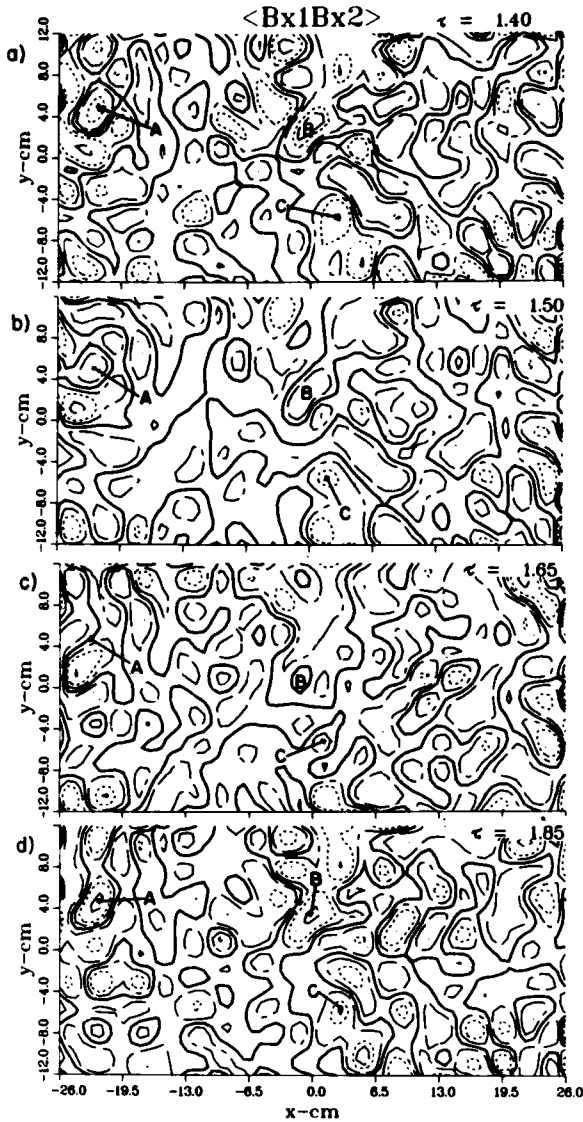

AUTOCORRELATION V.S. ⊕ SHOTS

a)

N =
10

b)

N =
25

c)

N =
68

|————— ΔT = 25.6 μsec —————|

Fig. 4. The autocorrelation function for digitally filtered ($Q = 6$) white noise as a function of N, the number of shots in an ensemble. As $N \to \infty$, the 373-kHz correlation signal should decay to $1/e$ in six periods. An 80-member ensemble chosen experimentally always guaranteed convergence.

$\langle Bx1Bx2 \rangle$ $\tau = 1.40$

a)

b) $\tau = 1.50$

c) $\tau = 1.65$

d) $\tau = 1.85$

Fig. 6. Contours of a component $\langle B_{x1}B_{x2}\rangle$ of the CSF tensor ($f = 1$ MHz) at four delay times τ in μs with respect to the measurement $t = 33.2$ μs into the reconnection event. The peaks oscillate at the wave frequency but do not propagate, which is characteristic of a standing wave. The average wavelength is of order 10 cm. The locations of the peaks referred to in the text $A = A(x, y) = A(-22.2, 4.3)$, $B = (0.0, 3.3)$, $C = (2.5, -5.5)$.

This was approached heuristically by a convergence test. Output from a white noise generator (20 kHz $\leq f \leq 1$ MHz) was fed into the 20-MHz analog to digital converters and digitally filtered [*Liu*, 1975] in the same way as the magnetic fluctuations. The quality factor $Q = \omega/\Delta\omega$ of a filter determines the number of periods it rings during an e folding decay time in response to a pulsed input. The normalized autocorrelation function is given by

$$R(\tau) = \frac{\frac{1}{N}\sum_{n=1}^{N} C_n(t_0)C_n(t_0 + \tau)}{\left\{\left[\frac{1}{N}\sum_{n=1}^{N} C_n^2(t_0)\right]\left[\frac{1}{N}\sum_{n=1}^{N} C_n^2(t_0 + \tau)\right]\right\}^{1/2}} \quad (2)$$

where $C(t_0 + \tau)$ is a signal with no mean values, measured at

delay time τ with respect to the start of measurement and N is the number of records of the ensemble. For delay times $\tau > Q(2\pi/\omega)$ and the ensemble numbers large enough for phase mixing to occur the correlation decays, $R(\tau) \to 0$. This is illustrated in Figure 4, where the autocorrelation is displayed for three ensemble sizes. The input signal is white noise digitally filtered at 373 kHz with $Q = 6$. $R(0)$ is one as expected but only for $N \geq 50$ $R(\tau)$ decays properly. It was therefore decided to use an 80 shot ensemble for the cross spectral analysis since this represented an upper limit on the computer memory for storage of four components and seemed to converge well.

CROSS SPECTRAL FUNCTION ANALYSIS

Assuming the noise to be composed of a large number of randomly generated waves, a correlation analysis is performed in order to identify modes from their dispersion relation $\omega(\mathbf{k})$ and polarization properties.

Two identical probe sets are used to measure the vector components of $\mathbf{B}_\perp(\mathbf{r}, t)$ at two different positions $\mathbf{r}$. During each reconnection event the signals are digitized by four 20-MHz analog to digital converters, then fast Fourier transformed (FFT) and digitally filtered by the on-line array processor (MAP200). An inverse FFT is done to generate the time history of the filtered signals in the frequency band of interest. Eighty consecutive shots are stored in the MAP memory, and the following operations are performed on the signals filtered at frequency ω with a filter $Q = 10$

$$B_{i,\omega,n}(t) = B_{i,\omega,n}^{\text{tot}}(t) - \langle B_{i,\omega}(t)\rangle \quad (3)$$

where $i = x, z$ denotes the vector component, B_n^{tot} is the total field measured during the nth shot, and $\langle B_i \rangle = (1/N)\sum_{n=1}^{N} B_{in}^{\text{tot}}$ is the average field at a time t. As discussed in the previous section, an ensemble number $N = 80$ is sufficiently large for a convergence of the mean values.

The cross-spectral function for nonstationary fluctuations [*Bendat and Piersol*, 1971] calculated on-line is given by

$$\langle B_{i2}B_{j2}\rangle_\omega(\Delta\mathbf{r}, t, \tau) = \frac{1}{80}\sum_{n=1}^{80} B_{i1,n,\omega}(\mathbf{r}, t)B_{j2,n,\omega}(\mathbf{r} + \Delta\mathbf{r}, t + \tau)$$

$$(4)$$

Here 1 and 2 refer to the two probe sets. The correlation is large if in moving from the fixed probe 2 over distance $\Delta\mathbf{r}$ a signal arrives after time τ in (or 180° out of) phase at probe 1. If there is a decay of the signal strength, a rotation of the field vector, or a loss of coherence with $\Delta\mathbf{r}$ and τ, the correlation will die out.

The cross-spectral function (CSF) may be normalized in the form

$$\rho_{ij}(\Delta\mathbf{r}, t, \tau, \omega) = \frac{\langle B_{i1}B_{j2}\rangle(\Delta\mathbf{r}, t, \tau, \omega)}{\langle B_{i1,\omega}^2(\mathbf{r}, t)\rangle^{1/2}\langle B_{j2,\omega}^2(\mathbf{r} + \Delta\mathbf{r}, t + \tau)\rangle^{1/2}}$$

$$(5)$$

so that it lies between $\rho = \pm 1$. Since the two terms in the denominator are stored separately, it is possible to evaluate both the normalized and the unnormalized correlation functions.

The normalized CSF magnifies the low level waves since the denominator of (5) is proportional to $B_{1\text{rms}}$ $B_{2\text{rms}}$, which can be misleading in estimating the spatial properties.

We point out that the filtered signal from a pickup loop is proportional to ωB, where ω is the center frequency of the

digital filter. The signals, therefore, were not integrated since the common factor ω drops out in (5) and is an overall multiplicative constant for the unnormalized CSF (equation (4)).

As observed with a single pickup loop, the fluctuations in B_x and B_z are of comparable amplitude. The individual probes are connected to isolation transformers and differential amplifiers that exhibited slightly different responses at higher frequencies such as 1 MHz. The magnitudes and delay time τ of the CSF were therefore corrected by a calibration magnetic field set up by a test wave to be described below.

With two vector components for each probe the CSF becomes a tensor of rank 2, given by

$$\rho = \begin{pmatrix} \rho_{x1x2} & \rho_{x1z2} \\ \rho_{z1x2} & \rho_{z1z2} \end{pmatrix} \quad (6)$$

The off-diagonal elements are large if over the displacement $(\Delta\mathbf{r}, \tau)$ an x component of the field rotates into the z direction or vice versa. The trace describes the correlation of the field strengths and converges for $\Delta\mathbf{r} = \tau = 0$ to Tr $\langle \mathbf{B}_1 \mathbf{B}_2 \rangle = B_{rms}^2$. The total number of on-line calculations to get ρ_ω at 300 spatial positions in a plane, 64 delay times τ, eight starting times t of intervals $\Delta T \simeq 3.2$ μs is staggering ($> 2 \times 10^8$). Nevertheless, we have measured ρ_ω at several frequencies and in two orthogonal planes.

The experimental layout for this measurement is shown in Figure 5. A stationary reference probe is positioned at $z = 0$ in a transverse plane located 137 cm from the cathode. Shown to scale is a measured vector plot of the transverse magnetic field. A second probe is free to move everywhere in either the same transverse x-z plane or in the orthogonal x-y plane containing the neutral sheet. Each probe shaft has two loops oriented to measure B_x and B_z.

Plate 2 shows the cross-spectral intensity $\langle B_{x1} B_{x2} \rangle$ at $f = 1$ MHz in the horizontal x-y plane. The measurements were insensitive to the absolute position of the fixed reference probe 2 within the neutral sheet. For all the data described here the fixed probe is located at $(x, y, z) = (-20$ cm, $0, 0)$ to maximize the area scanned. Note that the axis of the device goes through the center of the plane of Figure 5. The cathode in this coordinate system is at $y = -137$ cm. The three-dimensional display in the upper part and its two-dimensional projection as a contour map are taken at $t = 36.4$ μs after the start of the reconnection pulse with signal B_{x2} delayed by $\tau = 1.3$ μs with respect to B_{x1}. The observations, Plate 2, show a wavelike pattern in the x-y plane. Variations in the delay
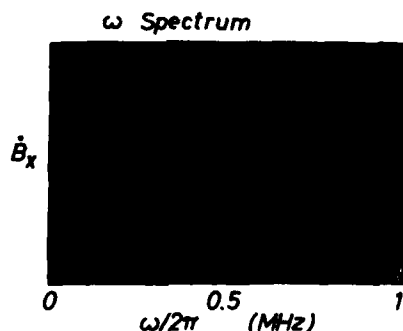

Fig. 7. Frequency spectra $\dot{B}_x$ during a single reconnection event obtained from an on-line fast Fourier transform. The magnetic noise extends to the limiting frequency of the detector $f_{lim} \cong 2$ MHz and is a factor of 10 above instrumental noise at 1 MHz. The lower hybrid frequency is 200 kHz, $f_{ci} \cong 1$ KHz, $f_{ce} = 28$ MHz.
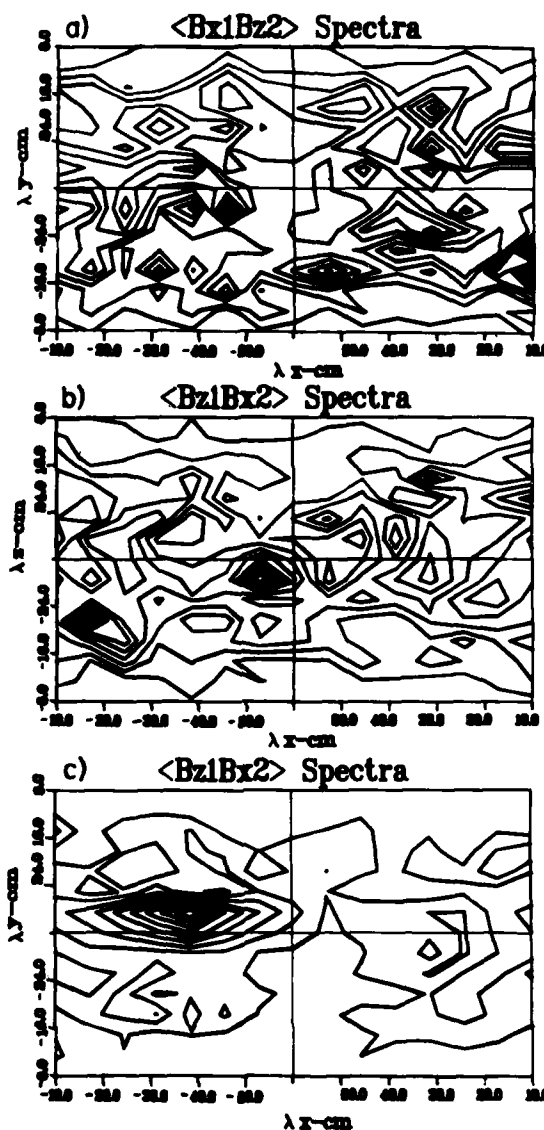

Fig. 8. Wave number spectra obtained from a two-dimensional spatial Fourier transform of the cross spectral function as shown in Plate 2. In general, the data indicate a spread in k space even at a single frequency component of the magnetic fluctuation spectrum and are multimode in both the x-y and x-z planes. Two tensor components $\langle B_{x1} B_{z2} \rangle$ and $\langle B_{z1} B_{x2} \rangle$ part (C) have a dominant mode in at least one plane. This feature makes possible an unambiguous polarization analysis of the mode. The spectra are normalized such that $0 \leq$ CSF$(k) \leq 1$ with 10% increments.

time indicate no preferred direction of wave propagation. The other components of the tensor have similar spatial properties. The fluctuations in B_x and B_z are of equal amplitude when observed with a single pickup loop.

In the simplest case of a single wave number and frequency, the expected pattern would be a succession of wave fronts with a maximum amplitude at the reference probe location [Gekelman and Stenzel, 1978]. If the wave propagation were spatially isotropic, the pattern would appear like the ripples in a pond after a pebble was dropped into it. Since the present case is more complicated, we begin to make further inferences about the waves by analyzing the CSF contours as a function of delay time τ.
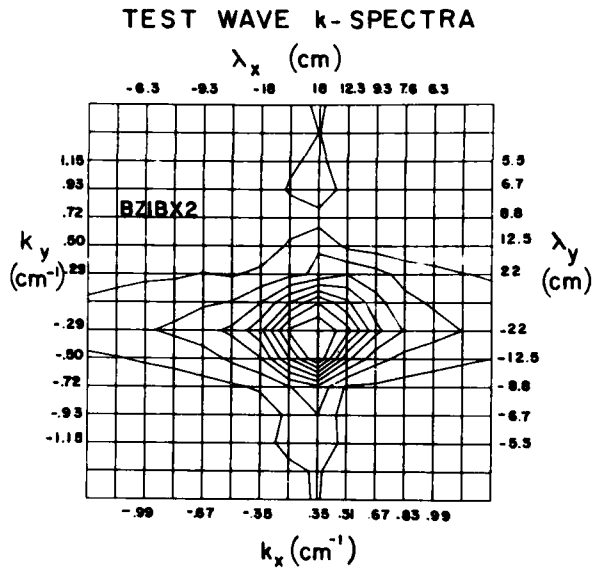
TEST WAVE k- SPECTRA

Fig. 9. Wave number spectra of a test wave in the plane containing the axial magnetic field, $B_{y0} = 10$ G, and neutral sheet ($z = 0$), generated from a two-dimensional spatial Fourier transform of the CSF displayed in Plate 4a. A dominant broadband mode $k_x = 0.35$ cm^{-1}, $k_y = -0.29$ cm^{-1} propagates at $\theta = \tan^{-1} k_y/k_x = -40°$. The spectrum in the transverse, x-z plane is similar but centered at the origin, $k_x = k_z = 0$, indicating no preferred direction of propagation.

Figure 6 is a contour map of the CSF tensor component $B_{x1}B_{x2}$ at 1 MHz versus τ. The start time is 33.2 μs into the reconnection event. To aid the eye, three peaks labeled A, B, and C have been singled out and are seen to diminish in amplitude in the 100 ns between Figures 6a and 6b. Roughly a quarter period after the sequence start (Figure 6c), peak A has entirely vanished; B and C are nearly gone. At approximately a half cycle from the outset (Figure 6d) the peaks have reversed sign but none of them have moved spatially. The CSF pattern has the characteristics of a standing wave, the interference of oppositely propagating modes at this frequency. There is no preferred direction; on the average, waves travel toward and away from the fixed probe with equal probability. Measurement of the separation between adjacent minima and maxima permits an estimate of the average wavelength, $\langle \lambda \rangle \simeq 10$ cm. Frequency and wavelength are typical for whistler waves in the present parameter regime.

Since the digital filter in this experiment has a value $Q = 10$, a significant amplitude decay of the CSF is not seen during the 3-μs delay time with respect to each start time t. The average amplitude of the CSF does, however, diminish as the reconnection event progresses. All components are a factor of 2 smaller at $t = 50$ μs since the induced electric field and neutral sheet current also decay in time.

Data taken in the x-z plane have a similar structure to those of the x-y plane. In principle, a three-dimensional correlation measurement in a volume of space would be required to determine the true wave number. Because of the nearly isotropic wave propagation two orthogonal planes are adequate.

At lower frequencies the wavelengths approach the system boundary size. The set of data at $\omega/2\pi = 500$ kHz had a similar structure to that in Figure 6; however, the wavelengths were longer and for $\omega/2\pi = 200$ kHz, which is just above the average lower hybrid frequency, the CSF is largest in the neu-

tral sheet region and appears to be a standing wave. To avoid any complications due to bounded modes, most of the analysis was focused on the highest frequency (1 MHz) mode.

WAVE NUMBER SPECTRA

The analysis of the spatial structure of the CSF does not lead to a positive identification of the modes. Our study proceeds with a two-dimensional Fourier transformation of the spatial distribution so as to obtain a wave number spectrum $\langle B_{i1}B_{j2} \rangle$ (k, τ) at a given frequency ω. This information is complementary to the frequency spectrum, a typical example of which is shown for $\dot{B}_x$ in Figure 7.

At each sample time t the CSF is calculated for 64 delay times τ ($\Delta\tau = 50$ ns). There is sufficient temporal resolution so as to calculate terms of the form $e^{i(\mathbf{k}\cdot\mathbf{r} - \omega t)} = \cos(\mathbf{k}\cdot\mathbf{r} - \omega t) + i \sin(\mathbf{k}\cdot\mathbf{r} - \omega t)$, from data points one quarter period out of phase. Using a complex kernel in the two-dimensional FFT enables the wave number spectrum to be calculated in a plane without symmetry assumptions. The two-dimensional wave number spectra of the tensor components $\langle B_{x1}B_{x2} \rangle$ and $\langle B_{z1}B_{x2} \rangle$ are displayed in Figure 8. The data in Figures 8a and 8c refer to the x-y plane, which contains the axial guide field ($B_{y0} = 12$ G) and runs along the center of the neutral sheet ($z = 0$). This k spectrum is acquired at $t = 33.2$ μs into the reconnection event when the turbulence is fully developed. The center axis of the grid corresponds to $k_x \simeq k_y = 0$. Since it is not possible to measure infinite wavelengths, the values on these axes correspond to averages taken from those above and below. We point out that the intervals along the abscissa and ordinate are not equal because the data are taken on a rectangular grid (3.14 cm $\leq |\lambda_x| \leq 24$ cm; 6.85 cm $\leq |\lambda_y| \leq 50$ cm in this display). The probes can resolve structures of order 1 cm. The wave number spectrum obtained from the x-y plane exhibits a dominant mode, as shown in Figure 8c for $\langle B_{z1}B_{x2} \rangle$.

The magnetic turbulence exhibits a broad range of κ values even at a single frequency ω. In the frequency regime between the lower hybrid and the electron cyclotron frequency ($\omega_{LH} < \omega \ll \omega_c$, where $\omega_{LH}/2\pi \simeq 0.1$ MHz, $\omega_c/2\pi \simeq 28$ MHz) oblique whistler modes have the properties of exhibiting a broad range of wave numbers depending upon the angle of wave propagation with respect to the magnetic field; they are right-hand circularly polarized electromagnetic modes [Helliwell, 1965].

The data are still too complex for comparison with theory, so that a further mode selection is required. The cross spectral functions are filtered in k space. The dominant modes of the CSF components are selected and individually examined after an inverse Fourier transformation into coordinate space. Plate 3a displays in real space a single mode ($\lambda_x = 48$ cm, $\lambda_y = 5$ cm) of $\langle B_{x1}B_{x2} \rangle$ from a multimode spectrum not unlike those of Figure 8. The function is sinusoidal with phase fronts nearly parallel to B_{y0}. As will be discussed below, the phase fronts may be easily tracked as a function of τ and the propagation studied. If a second mode is included (Plate 3b) the interference becomes obvious, although the contour plots projected below are still symmetric. For four modes (Plate 3c) the pattern begins to approach that of Plate 2, and tracking the motion of peaks as well as comparison with other tensor components of the cross-spectral function becomes as arduous as what was previously described. By transforming away all modes save one, spatial randomness is lost although the propagation direction, wavelength, and frequency are known with certainty. We are now in a position to analyze the wave polarization by comparing amplitudes and phase of two orthogonal

51

Plate 1. A stereo pair that illustrates the sheared magnetic field $\mathbf{B}(x, y, z) = \mathbf{B}_\perp(x, z) + \mathbf{B}_{y0}$. The projection of the three-dimensional field lines A_y is drawn in the x-z plane. The transverse magnetic neutral sheet within which $\mathbf{B}_\perp \cong 0$ is clearly visible. He 3×10^{-4} torr. $B_{y0} = 12$ G.

Plate 2. Stereo pair illustrating the wave pattern of the cross spectral function at 1 MHz in the x-y plane ($\mathbf{B} = B_{0y}$, $z = 0$). The complex pattern is due to the spatial interference of many oblique modes. The x and y axes have been shifted by $+24$ and $+10$ cm in this display.
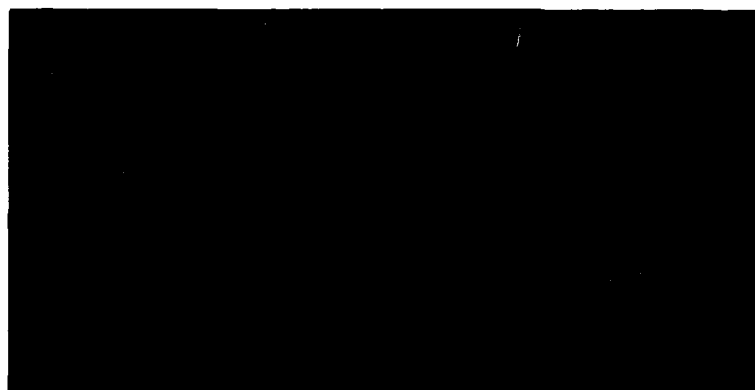
Plate 3a

Plate 3b

Plate 3c

Plate 3. Spatial variations of one or a few wave vector components of the cross-spectral function. These are selected from the peaks of Figure 6 and inverse Fourier transformed. (a) Mode A with $\lambda_x = 48$ cm, $\lambda_y = 5$ cm. (b) Mode A and mode B ($\lambda_x = 10$ cm, $\lambda_y = 12.5$ cm). (c) Modes A, B, C ($\lambda_x = 8.3$ cm, $\lambda_y = 10$ cm), and D ($\lambda_x = 7.14$ cm, $\lambda_y = 5$ cm). The decomposition allows one to investigate the polarization of single modes by comparing orthogonal tensor components. The x and y axes have been shifted by $+24$ and $+10$ cm, respectively, in this display.
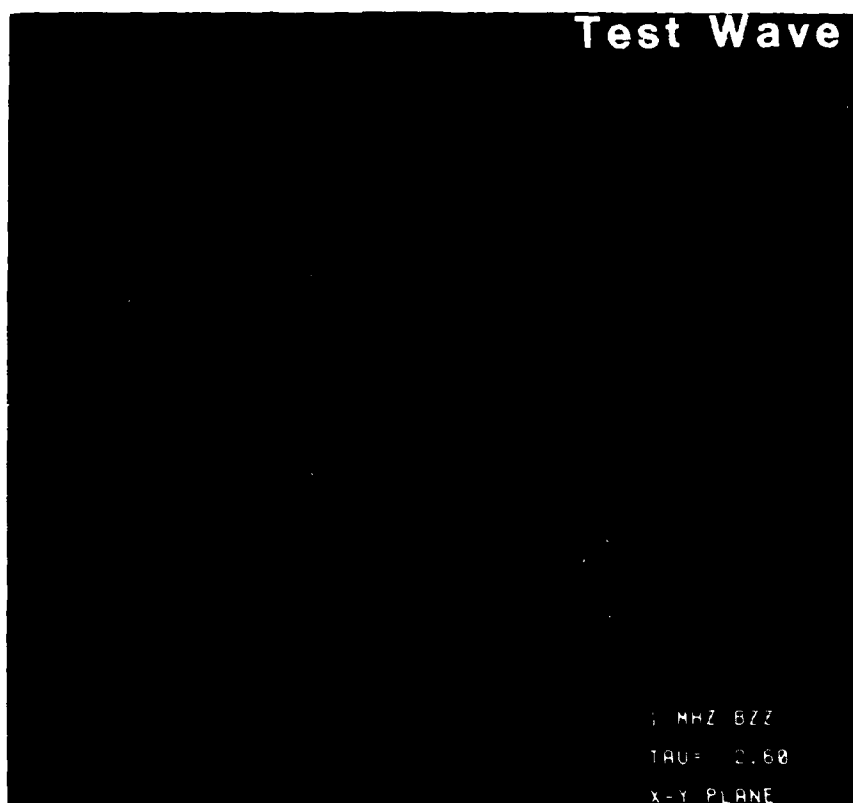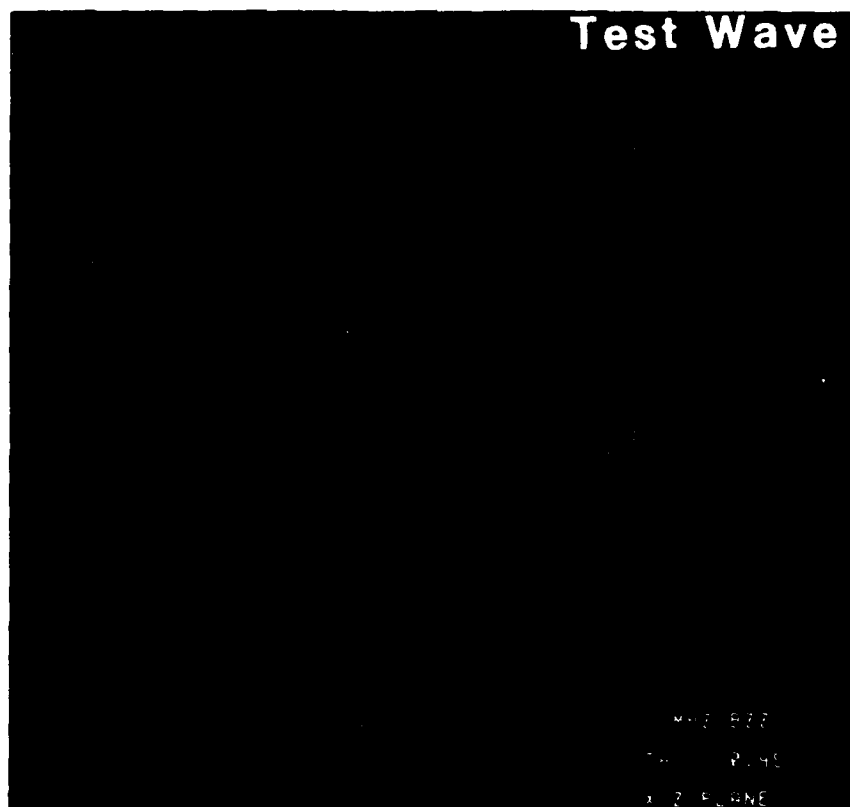
Plate 4a

Plate 4b

Plate 4. Two dimensional interferometer traces of the B_z components of a magnetic wave at $f = 1$ MHz. The wave is excited at $x = -20$ cm, $y = 0$, $z = 0$, and $t = 21.4$ μs into the reconnection event by a magnetic loop antenna with $\mathbf{B} = (0, 0, B_z)$ (a) propagating in the x-y plane; $B_{y0} = 10$ G, (b) propagating in the x-z plane.
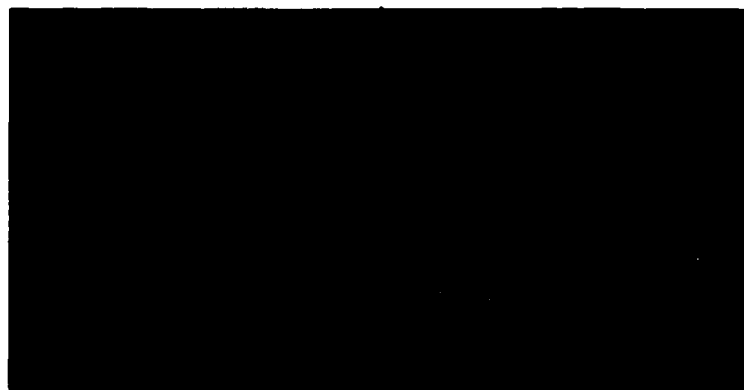
Plate 5a

Plate 5b

Plate 5.   Color stereo pairs of the three-dimensional wave number spectra at $f = 1$ MHz. The vertical green contour map is of the wave spectra in the k_y-k_x plane, the lower contour map is transverse k_z-k_x plane. The yellow markers with size proportional to amplitude are projections of the peaks into 3 space. The magenta surfaces are the cold plasma dispersion curves for oblique whistler waves at $B_y = 10$ G, $n_e = 4.9 \times 10^{12}$/cm^3. The vertical white line is drawn through $k_x = k_y = 0$ and a blue diamond at the origin $\mathbf{k} = 0$. (a) Spectrum of $\langle B_{x1}B_{x2} \rangle$ illustrating prolific mode structure. All fall within the limiting dispersion surface. (b) Spectrum for $\langle B_{z1}B_{z2} \rangle$. There are only three peaks present. It is possible to single out one mode (also see Figure 8c) for polarization analysis in this case ($t = 33.2$ μs).
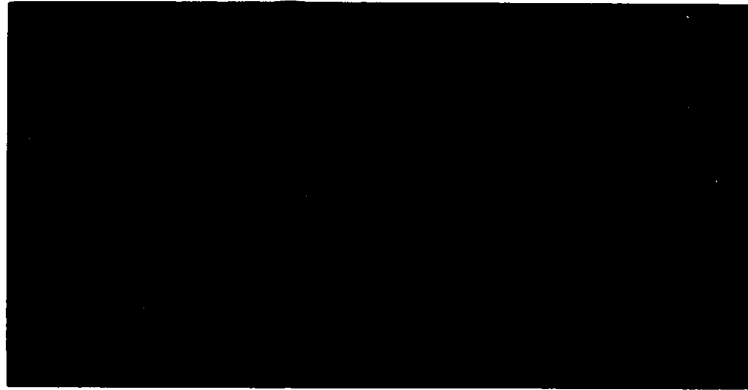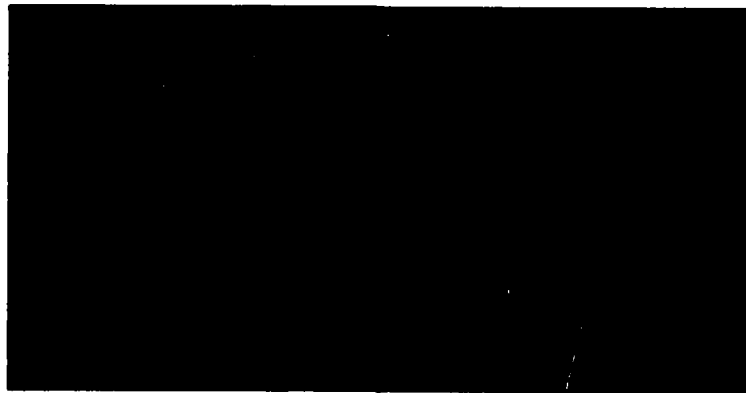
Plate 6a

Plate 6b

Plate 6.   Electron distribution functions. (a) At the edge of the neutral sheet ($\lambda = 20$ cm, $z = 0$) where no tails exist, and (b) in the center of the neutral sheet ($x = 0$, $z = 0$) where runaway electrons are observed. Upper panels show ensemble average values of $f(v_{\parallel})$, $f(v_{\perp})$, the surface is $f(v_{\parallel}, f_{\perp})$ on a logarithmic scale ($10^{-17} < f < 10^{-14}$ cm^{-6} s^3, $0 \leq |v| \leq 7 \times 10^8$ cm/s). Bottom plane shows rms fluctuation $f_{rms}(v_{\parallel}, v_{\perp})/f(0) = $ constant (3 dB/contour).

56

tensor components of the CSF. This analysis is not possible in a multimode pattern such as is shown in Figure 8a.

Prior to the polarization analysis we wish to review some basic properties of monochromatic whistlers excited by antennas in the neutral sheet.

TEST WAVE EXPERIMENTS

The CSF of the random 1-MHz waves exhibit good correlations through the entire x-y plane. Besides weak damping, this fact suggests that the excitation sources are extended so as to excite plane waves. For comparison, we now launch whistler waves at the same frequency under identical conditions from an antenna placed into the neutral sheet. Such wave experiments have been performed earlier in a quiescent, uniformly magnetized plasma with similar parameters ($\omega_p \gg \omega_c$, $\omega_{LH} < \omega < \omega_c$) except without a current sheet [Stenzel, 1975]. In these experiments a magnetic loop launched whistlers with diverging phase fronts, which causes an amplitude decay due to the divergence of the wave energy. The presence of a density gradient causes considerable wave refraction and amplitude variations. In the reconnection geometry the magnetic field is sheared (Plate 1) and the density within the neutral sheet is highly nonuniform (part 2). In order to facilitate comparison with the random waves, the test signal is launched near the center of the neutral sheet during the reconnection event.

The exciter is a 6-cm diameter, five turn loop, launching a wave with $B_z \approx 3$ G at 1 MHz. The applied signal is attenuated and is used as the reference signal in the correlation setup that is identical with an interferometer circuit. Owing to the phase coherence the test wave signal is easily distinguished from the 1-MHz background fluctuations. Surfaces of constant interferometer output [$\propto B(r) \cos (\mathbf{k} \cdot \mathbf{r})$] taken approximately 30 μs into the reconnection event are shown in the x-z plane in Plate 4b. Since the movable probe could not be positioned beyond the exciter loop, the data are symmetrized in the x direction about the z axis going through the antenna location. The radiation pattern in the x-y plane along the dominant axial magnetic field component B_{y0} is shown in Plate 4a. It indicates how the nonplanar phase fronts spread out along and across B_{y0}. The wave motion in time is best seen in a computer-generated movie that displays the measured τ dependence of Plate 4. A dominant oscillation with rapid spatial amplitude decay is observed in the transverse plane (Plate 4b). From these results one can estimate the typical wavelength to be $\langle \lambda \rangle \approx 10$ cm.

Wave number spectra generated by Fourier transforming the x, y dependence of B_z are shown in Figure 9. Unlike the corresponding fluctuation spectra there is one peak elongated along B_{y0} in the k_x-k_y plane. The contours are nearly circular in the transverse k_x-k_z plane. The dominant mode in the k_x-k_y plane moves at an angle of $\theta = -32°$ with respect to the magnetic field B_{y0}. In Plate 4b the exciter antenna at $x = -20$ cm is always to the left of the receiver antenna. The dominant modes in the k_x-k_y plane are therefore peaked at $k_x > 0$, describing the outward wave propagation. The waves of largest amplitude have axial wavelengths in the range $10 \leq \lambda_y \leq 20$ cm, in reasonable agreement with the dispersion relation for whistler waves given by

$$\left(\frac{kc}{\omega}\right)^2 = 1 - \frac{\omega_p^2}{\omega(\omega - \omega_c \cos \theta)} \approx \frac{\omega_p^2}{\omega(\omega_c \cos \theta - \omega)} \quad (7)$$

where ω_p, ω_c, and ω are the electron plasma, cyclotron, and wave frequencies, respectively. The same wavelength regime
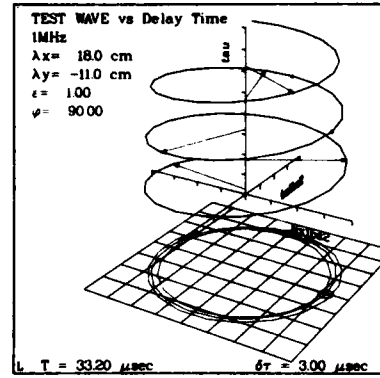

Fig. 10. Phasor diagram for the test wave generated by plotting two components of the CSF tensor $\langle B_{x1}B_{z2}\rangle$ and $\langle B_{z1}B_{z2}\rangle$ as a function of delay time τ, $0 < \tau < 3.0$ μs, rotated into the frame in which $\mathbf{k} \perp \mathbf{B}_{wave}$ ($k_z \cong 0$). The signal used to launch the wave is the common reference signal B_{z2} in the interferometer. The obliquely propagating mode is right-hand circularly polarized ($\epsilon = 1$, $\phi = 90°$), as seen by the projection onto the grid below. The arrows indicate the magnitude and direction of $B(\tau)$ at several of the 64 measured delay times. The dots on the trajectory indicate that the measurement of polarization was made on the second cycle and are projected below.

was found from the CSF analysis of the fluctuations that establish the connection between test whistler waves and the unstable modes.

The test wave exciter does not generate plane waves. Owing to geometric spread of the wave energy from a point source, the wave amplitude decreases rapidly with distance from the exciter. In contrast, the unstable waves exhibit a small amplitude decay. One can therefore conclude that the random waves are generated by extended sources; for example, long current filaments within the neutral sheet.

WAVE POLARIZATION

We consider the theoretical dispersion and polarization properties of whistlers in the quasi-longitudinal approximation [Ratcliffe, 1959]. It is valid when the angle of wave propagation satisfies

$$\frac{\sin^2 \theta}{\cos \theta} < \frac{2\omega_p^2}{\omega\omega_c} \quad (8)$$

For our parameters the right-hand side exceeds 10^6 so that the approximation is valid for essentially all angles ($\theta < 89.9°$). In the quasi-longitudinal approximation, the polarization of the wave magnetic field in the plane perpendicular to $\mathbf{k}$ is right-hand circular irrespective of the angle of wave propagation [Helliwell, 1965; Formisano and Kennel, 1969]. The polarization of the electric fields is different and will not be considered here.

First, we analyze the polarization of the test wave. The peak mode at $\mathbf{k} = (0.35 \text{ cm}^{-1}, -0.286 \text{ cm}^{-1})$ is chosen from the k_x-k_y spectrum of Figure 9. This mode fairly well satisfies the dispersion relation (equation (7)) for $n_e = 1.3 \times 10^{12}$ cm^{-3} $\pm 20\%$, $B_{y0} = 12$ G, the experimental conditions.

For analyzing the polarization we consider two orthogonal magnetic field components, B_x and B_z. The third component B_y does not have to be measured since it is determined by $\mathbf{k} \cdot \mathbf{B} = 0$. Both components are digitally filtered at $k_x = 2\pi/18$ cm^{-1} and $k_y = -2\pi/22$ cm^{-1}, and the signals are subsequent-
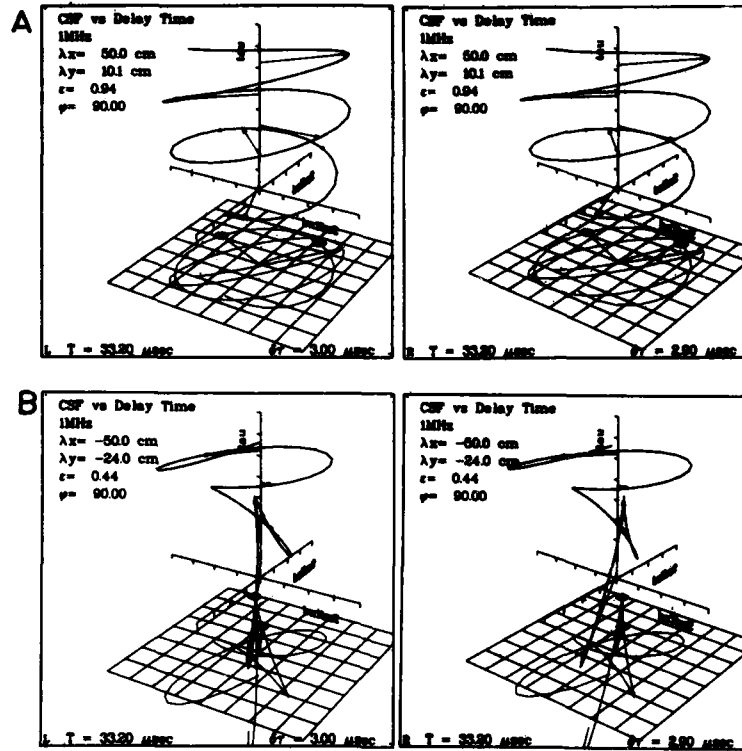
Fig. 11.   Stereo pairs of phasors generated from random waves. The display is as in Figure 10; however, B_{z2} is the random wave signal to the common reference probe. (a) Mode with $k \cong k_y = 0.79$ cm^{-1}. It is nearly circularly polarized, right handed, and satisfies the whistler dispersion relation. There is insufficient information to transform oblique modes properly, such as is shown in (b), $\theta \cong 26°$ to the frame with $\mathbf{k} \perp \mathbf{B}'$. The phasors exhibit bizarre motions in this case.

ly inverse Fourier transformed so as to obtain

$$\underset{x(x,y,\tau)}{B(\omega, k)} \qquad \underset{z(x,y,\tau)}{B(\omega, k)}$$

Amplitude and phase of each component is retained as a function of delay time τ so that we can plot the phasor $\mathbf{B}_{(\tau)}$. Because we consider the magnetic field polarization in the plane perpendicular to $\mathbf{k}$ the field components in the laboratory coordinate system (x, y, z) must be projected into a rotated frame (x', y', z') with y' along $\mathbf{k}$. This transformation yields

$$B_x' = B_x/\cos \theta \qquad B_z' = B_z \qquad B_y' = 0 \qquad (9)$$

where the primes refer to the rotated coordinate system.

Figure 10 is a phasor diagram $\mathbf{B}_{(\tau)}'$ for the test wave. The vector components are normalized in amplitude as discussed in the previous section, and one component is delayed with respect to the other one by 50 ns which was the digitization time, hence corresponds to an error of only one synchronization pulse. The data refer to a start time of 33.2 μs into the reconnection event and display the phasor $\mathbf{B}_{(\tau)}'$ for delay times $0 \leq \tau \leq 3$ μs. The vector tip sweeps out a right-handed spiral in time whose projection into the B' plane is a circle. At five discrete time steps the vector $\mathbf{B}_{(\tau)}'$ is indicated. The figure also presents values for ε, the ratio of the semimajor to semiminor axis, and ϕ, the phase difference between the vector components measured between successive maxima B_{smax} and B_{smax} in one of the cycles. All the test wave modes in the vicinity of the spectral peak (Figure 9) are right-handed circular whistler waves.

The random modes have. in general, three wave vector components that must be known in order to find the polarization in the plane orthogonal to $\mathbf{k}$. This would require that CSF be measured throughout a volume so that one can perform a three-dimensional spatial Fourier transformation. However, it is often sufficient to consider two orthogonal planes if certain symmetries in the wave propagation exists. For example, one may consider the polarization of all the waves along the lines $k_x = \pm 0.126$ cm^{-1} $(\lambda_x = \pm 50$ cm) in the k_x-k_y plane, Figure 8a. These are modes that travel at small angles with respect to the uniform magnetic field B_{yo}. The spectrum in the k_x-k_z plane is roughly symmetric about k_y, and as an approximation we choose for the average wave number $\langle k_z \rangle \approx 0$ for purpose of investigating the polarization of modes in the k_x, k_y plane. The polarization at different values k_y should be right-hand circular for waves that fit the dispersion relation (equation (7)). More than 80% of the modes tested are confirmed to be right-hand polarized. For example, Figure 11a shows a phasor diagram for a random mode with $k \simeq k_y = 0.63$ cm^{-1} with ellipticity $\varepsilon = 0.94$ in the first cycle, i.e., with nearly right-hand circular polarization. Most of the random waves exhibit changes in ε and orientation of the major axis as a function of delay time τ. The CSF (Figure 6) and resulting k spectra are weakly time dependent, and it is possible that the third component k_z enters in time and affects the calculated polarization. Whether indeed all the waves are right-hand polarized can only be resolved by performing a fully three-dimensional Fourier analysis that permits a proper transformation of $\mathbf{B}$ into the plane orthogonal to $\mathbf{k}$. We interpret the nearly circu-

lar polarizations, seen mainly for parallel wavelengths of order 10 cm as cases of whistler waves with $k_z \approx 0$.

Examination of modes that are more oblique reinforces this picture. Figure 11b is a phasor plot of a wave propagating at $\theta = 26°$ with respect to the magnetic field B_{y0}. The phasor diagram is very complicated and is best appreciated in a stereoscopic view, as shown. The polarization appears highly elliptical and is seen to reverse as a function of τ. The projection onto the lower grid resembles the fluctuating component of the hodogram in Figure 2c as if everything save the loops visible in Figure 2b have been averaged away. This type of phasor is representative of all waves propagating at large angles with respect to B_{y0}. This does not necessarily mean that these waves are elliptical but that there may be insufficient information to transform B into the proper frame. If there were more data points available, a statistical analysis for the polarization as a function of propagation angle could be undertaken in order to check this assumption. The present data, however, strongly suggest that the random waves are whistler waves propagating at all angles up to the resonance cone ($\theta \approx \cos^{-1}(\omega/\omega_c) = 88°$).

The polarization sampling procedure was relegated to waves moving, on the average, at small angles with respect to the background magnetic field. The spectrum of $\langle B_{z1}B_{x2}\rangle$ in the k_x-k_y plane has one intriguing highly oblique mode (Figure 8c). An estimation of its polarization is possible, but best follows a discussion of the three-dimensional spectra.

THREE-DIMENSIONAL WAVE PROPAGATION

Wave number data acquired in two orthogonal (k_x-k_y) and (k_x-k_z) planes make a three-dimensional reconstruction of the wave vector structure possible. Such a diagram is shown in Plate 5 as a stereoscopic pair for $\langle B_{x1}B_{z2}\rangle$. Wave number spectra are shown as contour plots projected to the bottom and to the side of a rectangular volume in k space ($|k_x| \leq 0.69$ cm^{-1}, $|k_y|$, $|k_z| \leq 1.35$ cm^{-1}). Each point α in the volume is tested to insure the mode associated with it is well above the noise; CSF $[(k_x, k_z)_\alpha, (k_x, k_y)_\alpha] \geq 0.45$, where the largest value of the combined spectra is normalized to be 1.00. The mode is then projected into three-dimensional k space as a yellow marker with size proportional to the amplitude to which it corresponds. Also drawn in magenta are the dispersion surfaces $k(\theta)$ (equation (7)) for obliquely propagating whistler waves at a fixed density, in argon, $n_e = 4.9 \times 10^{12}/cm^3$, magnetic field, $B_{y0} = 10$ G, and frequency $\omega/2\pi = 1$ MHz. A vertical line through the symmetry axis ($k_x = k_y = 0$) is drawn to aid the eye. A blue diamond marks the origin in k space.

The density within the neutral sheet is nonuniform (part 2) and may be 2.5 times larger at the second-order contact points of the separatrix than in the center of the neutral sheet. Waves in lower density regions in turn give rise to points in Plate 5a that lie closer to $k_y \simeq 0$ for nearly perpendicular propagation. The magnetic field is constant to within 10% along the y direction but increases in the x-z plane as one moves away from the neutral sheet. In this situation the wave dispersion surfaces are expected to sweep through a volume. The curves that are drawn in Plate 5a may be interpreted as a reasonable outer envelope for these experimental parameters. That the majority of the modes fall within this volume of k space is strong evidence that the magnetic turbulence is comprised of whistler waves.

The large number of modes in wave number space precludes any further investigation of the CSF component shown in Plate 5a. This is, however, not always the case. There are far

fewer modes observed for tensor element $\langle B_{z1}B_{x2}\rangle$ as illustrated in Plate 5b. The dominant mode located at $k_x = -0.62$ cm^{-1}, $k_y = 0.26$ cm^{-1}, and $k_z = -0.26$ cm^{-1} is an oblique mode with its counterpart in tensor component $\langle B_{z1}B_{x2}\rangle$. Its peaks are clearly seen in the contour lines projected onto the lower and side planes.

If the fluctuating magnetic field CSF had been measured everywhere within a volume of real space, the polarization analysis would be tedious but straightforward. The three-dimensional Fourier transform into wave number space and filtration of the mode of interest would proceed analogous to the technique described in the previous section. After transformation into a plane perpendicular to k, the polarization may be traced.

Since the CSF is mapped on orthogonal planes only, the following procedure is used to estimate the polarization. Both planes have an axis (k_x) in common. The CSF modes are filtered out of the orthogonal k space planes and the components vectorially summed, i.e., $\langle B_{z1}B_{a2}\rangle = \langle B_{z1}B_{a2}\rangle(k_x, k_z) + \langle B_{z1}B_{a2}\rangle(k_x, k_y)$, where $\alpha = z, x$. The data from each of the orthogonal planes were of comparable magnitude, but their initial phase had to be equalized since they were acquired on separate runs. This did not affect the polarization calculation. Finally, we note that the probe in common for this CSF pair was the movable probe that is equivalent to replacing τ by $-\tau$.

The data were transformed by two successive rotations in k space such that $\mathbf{k}'' = (0, k_y'', 0)$ and $B_{y2}'' = 0$ since $\mathbf{k} \cdot \mathbf{B} = 0$. (For simplicity we drop the prefix B_{z1}.) The transformation is given by

$$B_x'' = B_x/\cos\theta_1 + B_z \frac{k_z}{k_y}\sin\theta_1$$

$$B_z'' = B_z\left(\frac{k_z\sin\theta_2}{(k_x^2 + k_y^2)^{1/2}} + \cos\theta_2\right) \tag{10}$$

where

$$\tan\theta_1 = \frac{k_x}{k_y} \qquad \tan\theta_2 = \frac{k_z\cos\theta_1}{k_y}$$

Here k is the wave number in the original laboratory frame. Note that in the x-y plane $k_z = 0$ and (10) reduces to the transformation given by (9).
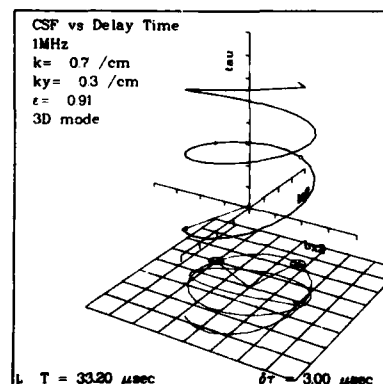

Fig. 12. Phasor generated from single CSF modes digitally filtered from the three dimensional k spectra (as shown in Plate 5b) and transformed such that $\mathbf{k} \perp \mathbf{B}_{wave}$. The highly oblique mode $\alpha = \cos^{-1} k_y/k = 64°$ is a right-hand polarized and nearly circular polarized whistler ($t = 33.2 \mu s$).

The transformed data plotted as a phasor in Figure 12 identify the dominant mode to be a right-hand, nearly circular polarized whistler wave. Although the agreement here could be fortuitous, we view this as being unlikely in light of the experiment in surveying modes in which k is not known (such as is shown in Figure 11b).

The whistler waves are not the only component of the turbulence within the neutral sheet. We have performed preliminary fluctuation studies at higher frequencies and observed a wide range of electrostatic modes.

ION SOUND AND LANGMUIR TURBULENCE

Using two electrostatic probes, we have measured with analog correlation techniques the frequency and wave number spectrum of modes along B_{y0} within the neutral sheet. The results are summarized in Figure 13. The cross spectral function at 2 MHz enables the straightforward evaluation of a single wavelength (unlike the whistler case). From different measurements of ω and k we obtain a linear dispersion characteristic for ion acoustic waves. It is well known that short wavelength ion sound modes ($\lambda \to \lambda_D$ as $\omega \to \omega_{pi}$) can produce significant scattering of electrons which manifests itself as an enhanced resistivity (part 4).

The microwave emission ($f \simeq f_p \simeq 12$ GHz) from the reconnection event is monitored with a horn antenna located outside the plasma column and connected to a sensitive microwave receiver. Figure 14 shows a large burst of electromagnetic radiation during reconnection. In this case the event is triggered late in the discharge to make the signal easily distinguishable from that due to the primary (ionizing) electrons. In a separate experiment [Whelan and Stenzel, 1981], electromagnetic radiation at the plasma frequency is observed to be generated when electron plasma waves scattered off ion acoustic fluctuations. The Langmuir waves were driven unstable by an electron beam.

MICROWAVE EMISSION

E^2

$f = f_p = $ 12 GHz

Time t ↑

Reconnection

Fig. 14. Microwave emission (arb units) at the plasma frequency observed with an external horn connected to a radiometer. The background radiation is due to primary electrons within the dc discharge. For purpose of clarity the reconnection event is switched on 1.2 ms after the discharge is initiated. The large pulse of radiation is presumed to be associated with Langmuir turbulence driven by electrons accelerated within the neutral current sheet.

In the reconnection event a runaway tail of electrons, confined to the neutral sheet, is produced by the induced electric field. Langmuir waves grow at the expense of the free energy in the tail, scatter off ion acoustic waves or convert on density gradients to generate the observed microwave emission.

ELECTRON DISTRIBUTION FUNCTIONS

Non-Maxwellian particle distribution functions may provide conditions for plasma wave growth. If these waves reach, large amplitudes particles in turn may be scattered or trapped by them. If the full distribution function were known, $f(v, r, t)$, most instabilities may be predicted theoretically or by simulations. Although a complete measurement of f is a massive undertaking in data acquisition, several steps toward it have been made. One would like to compare the observed wave phenomena and particle scattering with distribution functions to see if they are consistent. A strong modification of the distribution at a given phase velocity may be reflected by strong wave activity there. In this section some preliminary measurements will be discussed; details will be presented in a subsequent article in this journal.

The electron distribution functions are measured with a novel velocity analyzer [Stenzel et al., 1983a, c] that transmits electrons within a small acceptance angle ($\Delta\Omega = 0.036$ sr). The essentially one-dimensional velocity of the transmitted electrons is analyzed with a gridded retarding potential energy analyzer. The analyzer's mounting permits a continuous rotation about the two polar angles θ, ϕ, so as to obtain $f(v, \theta, \phi) = f(\mathbf{v})$. This involves repeated measurements at typically 200 different angles. The device may be moved to different spatial positions within the reconnection region. Temporal resolution is provided by a fast voltage sweep ($\Delta t = 2$ μs) on the analyzer grid. In principle, it is possible to determine the full electron distribution function $f_e(\mathbf{v}, \mathbf{r}, t)$.

The analyzer output is digitized with a 100-MHz A/D converter. At every angle 10 current voltage traces are recorded. The on-line array processor differentiates the I-V curves and smooths out the digital noise. It then calculates the distribution function as well as the rms fluctuations at every angle.

(a) Ar, 2×10^{-4} Torr $x = z = 0$
$\frac{\delta n}{n}$ $t = 40$ μsec
10 dB
$\sim f_{pi}$
0   10   20   30
FREQUENCY f (MHz)

(b)
$\frac{\omega}{2\pi}$ (MHz)
$C_{12}(\Delta y)$
$f = 2$ MHz
Δy
$\omega = k c_s$
($T_e = 5$ eV)
2 mm
0   50   100   150
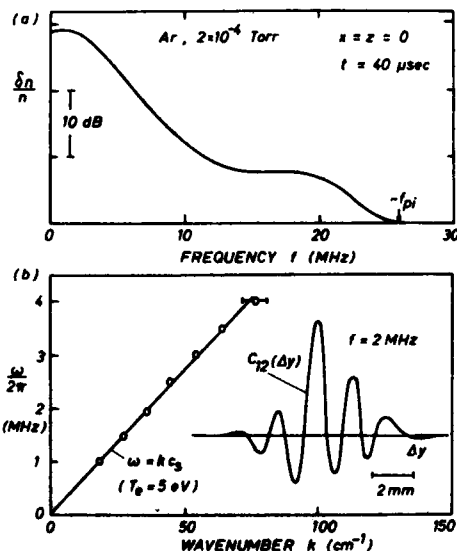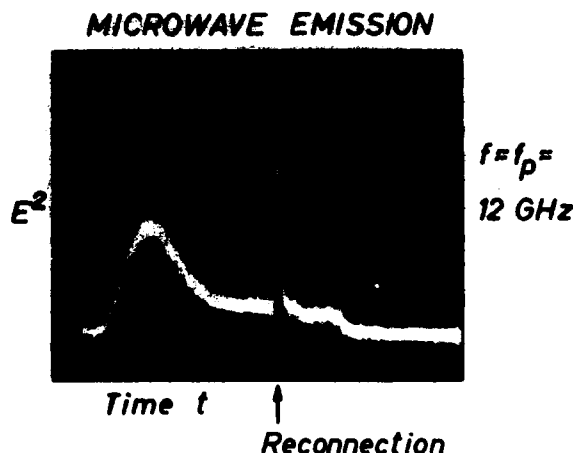WAVENUMBER k (cm^{-1})

Fig. 13. Characteristics of electrostatic fluctuations during reconnection. (a) The frequency spectrum of density fluctuations extends up to the ion plasma frequency f_{pi}. Integrated fluctuation levels are on the order of $\langle \delta n/n \rangle_{rms} \simeq 5\%$. (b) Wave number spectrum of low-frequency fluctuations exhibits the dispersion of the ion sound waves. The spatial noise properties are obtained from two-probe cross power spectral functions $C_{12}(\Delta r)$, an example of which is inserted.

The distribution functions are displayed as three-dimensional stereo pairs, for ease of viewing, in Plate 6. The upper surface shows the distribution function $f(v_{\parallel}, v_{\perp})$ taken 33.2 μs into the reconnection event, at the edge of the neutral sheet ($z = -22.5$ cm, Plate 6a) and within it ($z = 7.5$ cm, Plate 6b). Here $v_{\parallel}$ denotes velocity along the uniform guide field B_{yo}. The velocity range is $|v_{\perp}, v_{\parallel}| \leq 6 \times 10^8$ cm/s. The distribution function is plotted logarithmically over three orders of magnitude, $10^{-17} \leq f(v, z = 7.5 \text{ cm}) \leq 10^{-14}$ cm^{-6} s^3, $f(v = 0, z = -22.5 \text{ cm}) = 1.3 f(v = 0, z = 7.5 \text{ cm})$. In drawing these graphs it is assumed that the curve is symmetric about the azimuthal angle ϕ. Full three-dimensional data sets indicate that the symmetry is only approximate. The distribution function is best examined by using computer generated films of successive surfaces of $f(v) = $ constant. On the plane projected immediately below the distribution surface are ten (green) contours log $f(v) = $ const (3 dB/contour). We observe a high-energy electron tail (Plate 6b) that carries the plasma current and extends to energies in excess of 75 eV. Since most of the energetic electrons in the discharge have energies $eV_{dis} = 45$ eV, we conclude they have been freely accelerated by the electric field.

The shaded violet projections on the rear surfaces indicate what would be measured by probes directly along $(f_{\parallel})$ across $(f_{\perp})$ the uniform background field. Anisotropic distributions cannot be resolved by using single-sided planar Langmuir probes since they integrate $f(v, \theta, \phi)$ over $\Delta\theta, \Delta\phi = \pi$ in velocity space.

At the current sheet edge near the contact points of the Y shaped separatrix (Plate 1, Figure 5) there is a vertical magnetic field component ($B_z \sim 2$ G) that prevents runaway tail formation (Plate 6a).

The velocity space rms fluctuations of the distribution functions are shown as blue contours in the lowest plane of Plate 6. The Doppler shifted whistlers have phase velocities $|v_{\parallel}| = |\omega - \omega_c|/k_{\parallel}$ ($\simeq 2.5 \times 10^8$ cm/s) that fall into the velocity range of large rms fluctuations. The phase velocity of beam driven Langmuir waves also fall into this regime $\omega/k_{\parallel} \gg v_{the} \gtrsim 10^8$ cm/s. No detailed measurement of this high-frequency turbulence has been made thus far.

The ion acoustic modes have phase velocities $\omega/k = c_s = 3.5 \times 10^5$ cm/s that place them near the origin of the plots in Plate 6, where measurement errors limit the resolution of $f(v)$.

SUMMARY AND CONCLUSIONS

We have approached sorting out the complex net of interwoven processes that constitute magnetic field line reconnection with measurements taken from three perspectives. The first level is macroscopic in which ensemble averaged properties such as density, temperature, and embedded electric and magnetic fields were mapped out as a function of space and time. This is somewhat analogous to the fluid approach in theoretical physics, and constitutes the bulk of measurements described in JGR papers 1-5. Although turbulence may manifest itself in the form of anomalous resistivity and enhanced fluid scattering (parts 3 and 4), a second, statistical approach is necessary to probe the underlying structure of it. In this work extensive digital data acquisition and statistical computation have been brought to bear on magnetic turbulence and enabled the unfolding of the frequency and wave number spectrum of unstable whistler waves. Statistical studies of the wave polarization vis à vis the cross spectral tensor indicate the waves are right handed and nearly circular. Analysis of whis-

tler polarizations made on the earth's surface of waves which entered the ionosphere [Tsuruda and Ikeda, 1979] are also statistical surveys from which the direction of the incoming wave must also be estimated. The propagation direction k and polarization for fairly monochromatic waves have been ascertained from hodograms and flux gate magnetometers on the ISEE satellites as they traversed the bow shock [Hoppe et al., 1982]. Correlation of magnetic fields measured by the satellite pair was used to find the phase velocity, again for the uncommon case of nearly monochromatic signals. Dispersive effects make such two point correlations difficult since the spacecraft are always more than several wavelengths apart. Nevertheless, these waves were found to be oblique whistlers driven unstable by ion beams reflected off the bow shock. Whistlers seem to be ubiquitous in space plasmas, having thus far been observed in the bow shock, auroras, plasma sheet, magnetosheath, and solar wind, as well as in the environs of Jupiter.

In our laboratory plasma we have established a magnetic field topology similar to that of magnetotail models. A possible difference is our axial field component B_{yo}, which at times may exist in the magnetotail but is usually ignored in theoretical and numerical models [Sonnerup, 1979]. It establishes magnetized electrons in the current sheet and whistler eigenmodes throughout the dissipation region. Our observations show that the whistler wave activity correlates with the neutral sheet current; for example, the wave intensity nearly vanishes at current reversal ($I_p \simeq 0$ at $t = 80$ μs).

In this experiment, we used two probe cross correlation techniques for analyzing magnetic turbulence. This powerful technique has not yet been employed in space physics since it requires mother-daughter satellite systems. From the correlation measurements, we have established the wave dispersion $\omega(\mathbf{k})$ and magnetic field polarization $\mathbf{B}(\tau)$. This was feasible through the use of digital data processing involving fast Fourier transforms and digital filtering on the spatial and temporal dependence of magnetic fluctuations. A dominant mode found in two components of the CSF lent itself particularly to examine the B field polarization that was found to be right-handed. A procedure to estimate the wave numbers in three dimensions for this right-hand circularly polarized wave as well as the other components of the noise enabled comparison with the dispersion surfaces of the whistlers. Full three-dimensional analysis will be possible with increased computer memory and mass storage. Higher order correlations have already been used to estimate wave-wave coupling and transport [Powers, 1974; Roth et al., 1978] in a simpler geometry and could be extended to this case.

Having established that the observed random waves are oblique whistlers sets the stage for future experiments that will explore how (or if) the whistlers feed back on the reconnection process via particle dynamics. The wave frequencies are well above the ion but below the electron cyclotron frequency: $\omega_{ci} \ll \omega_{LH} \simeq \omega < \omega_{ce} < \omega_{pi} \ll \omega_{pe}$. In this frequency regime ion motion is affected by the wave and is resonant with it at $\omega = \omega_{LH}$. The ions may also respond to space charge fields that result from nonlinear interaction of electrons with the whistlers. It is, however, not yet clear if the whistlers are responsible for the large ion scattering previously observed (part 3). Also unexplained is the observation that the number of modes in k space differs for elements in the CSF tensor. This presumably depends upon the details of growth and saturation that have not as yet been explored experimentally. To the authors' knowledge, no theory for whistlers under these conditions exists.

A stronger statement can be made about the electrons whose Doppler shifted phase velocity $v_{\parallel} = (\omega - \omega_{ce})/k_{\parallel}$ (2.5 × 10^8 cm/s) falls into the velocity space occupied by the fast electrons (Plate 6b). It is likely these electrons provide the free energy to drive the waves unstable and in turn are scattered by them. A possible mechanism could be filamentation within the current sheet (part 5) in which individual current channels act as localized antennas. Current filamentation and turbulence have been observed numerically in an MHD simulation [*Matthaeus and Montgomery*, 1981].

In an interesting particle simulation of a low average beta ($\beta = 8\pi nk\tau/B^2 \approx 0.03$) neutral sheet [*Tanaka and Sato*, 1981] electron heating, anomalous resistivity, and particle transport developed within a plasma with initial electron and ion drifts. Lower hybrid waves were observed; the nonlinear development includes both electromagnetic modes and distortions in the magnetic field.

Spacecraft observations of scattering of energetic electrons by whistlers have been made in the subauroral magnetosphere [*Carpenter and LaBelle*, 1982]. Electrons trapped by obliquely propagating whistlers may be, in turn, responsible for the generation of fast electron beams (H. Matsumoto, private communication, 1983).

It is possible to unravel the interplay of particles and waves. It must be done at the most fundamental level, the detailed measurement of particle distribution functions and the phase space correlation of wave-particle data. As reported here, techniques have been developed to measure $f(v, r, t)$ and its velocity space fluctuations, which lay the groundwork for the next phase of this investigation. As data become available, rapid theoretical progress in turbulence will surely follow [*Montgomery*, 1982].

REFERENCES

Anderson, R. R., C. C. Harvey, M. M. Hoppe, B. T. Tsurutani, T. E. Eastman, and J. Etcheto, Plasma waves near the magnetopause, *J. Geophys. Res.*, *87*, 2087-2107, 1982.
Bendat, J. S., and A. G. Piersol, *Random Data: Analysis and Measurement Procedures*, Interscience, New York, 1971.
Carpenter, D. L., and J. W. LaBelle, A study of whistlers correlated with bursts of electron precipitation near $L = 2$, *J. Geophys. Res.*, *87*, 4427-4434, 1982.
Coroniti, F. V., C. F. Kennel, F. L. Scarf, and E. J. Smith, Whistler mode turbulence in the disturbed solar wind, *J. Geophys. Res.*, *87*, 6029-6044, 1982.
Dreicer, H., Electron and ion runaway in a fully ionized gas, *Phys. Rev.*, *115*, 238-249, 1959.
Dum, C. T., Anomalous heating by ion sound turbulence, *Phys. Fluids*, *21*, 945, 1978.
Dungey, J. W., *Cosmic Electrodynamics*, Cambridge University Press, New York, 1958.
Formisano, V., and C. F. Kennel, Small amplitude waves in high β plasmas, *J. Plasma Phys.*, *3*, 55, 1969.
Furth, H. P., J. Killeen, and M. Rosenbluth, Finite-resistivity instabilities of a sheet pinch, *Phys. Fluids*, *6*, 459, 1963.
Gekelman, W., and R. L. Stenzel, Ion sound turbulence in a magnetoplasma, *Phys. Fluids*, *21*, 2014-2023, 1978.

Gekelman, W., and R. L. Stenzel, Magnetic field line reconnection experiments, 2, Plasma parameters, *J. Geophys. Res.*, *86*, 659-666, 1981.
Gekelman, W., R. L. Stenzel, and N. Wild, Magnetic field line reconnection experiments, 3, Ion acceleration, flows, and anomalous scattering, *J. Geophys. Res.*, *87*, 101-110, 1982a.
Gekelman, W., R. L. Stenzel, and N. Wild, Magnetic field line reconnection experiments, *Physica Scripta*, *T2/2*, 277-287, 1982b.
Gurnett, D. A., and L. A. Frank, Ion acoustic waves in the solar wind, *J. Geophys. Res.*, *83*, 58, 1978.
Gurnett, D. A., R. R. Anderson, B. T. Tsurutani, E. J. Smith, G. Paschmann, G. Haerendel, S. J. Bame, and C. T. Russell, Plasma wave turbulence at the magnetopause: Observations from ISEE 1 and 2, *J. Geophys. Res.*, *84*, 7043-7058, 1979a.
Gurnett, D. A., R. R. Shaw, R. R. Anderson, W. S. Kurth, and F. L. Scarf, Whistlers observed by Voyager 1: Detection of lightning on Jupiter, *Geophys. Res. Lett.*, *6*, 511, 1979b.
Helliwell, R. A., *Whistlers and Related Ionospheric Phenomena*, Stanford University Press, Stanford, Calif., 1965.
Hoppe, M. M., C. T. Russell, T. E. Eastman, and L. A. Frank, Characteristics of the ULF waves associated with upstream ion beams, *J. Geophys. Res.*, *87*, 643-650, 1982.
Kadomtsev, B. B., *Plasma Turbulence*, pp. 68-78, Academic, New York, 1965.
Langmuir, I., The interaction of electron and positive ion space charges in cathode sheets, *Phys. Rev.*, *33*, 954, 1929.
Liu, B. (Ed.), *Digital Filters and the FFT*, John Wiley, New York, 1975.
Loeve, M., *Probability Theory*, 2nd ed., Van Nostrand, Princeton, N. J., 1960.
Matthaeus, W. H., and M. L. Goldstein, Stationarity of magnetohydrodynamic fluctuations in the solar wind, *J. Geophys. Res.*, *87*, 10347-10354, 1982.
Matthaeus, W. H., and D. Montgomery, Nonlinear evolution of the sheet pinch, *J. Plasma Phys.*, *25*, 11-41, 1981.
McPherron, R. L., Magnetospheric storms, *Rev. Geophys. Space Phys.*, *17*, 657, 1979.
Montgomery, D., Major disruptions, inverse cascades, and the Strauss equation, *Physica Scripta*, *T2/1*, 83-88, 1982.
Powers, E. J., Spectral techniques for experimental investigation of plasma diffusion due to polychromatic fluctuations, *Nucl. Fusion*, *14*, 749-752, 1974.
Ratcliffe, J. A., *The Magneto-Ionic Theory and Its Applications to the Ionosphere*, Cambridge University Press, New York, 1959.
Roth, J. R., W Krawczonek, E. J. Powers, J. Y. Hong, and Y. C. Kim, Inward transport of a toroidally confined plasma subject to strong radial electric fields, *Phys. Rev. Lett.*, *29*, 1450-1453, 1978.
Russell, C. T., and R. C. Elphic, Initial ISEE magnetometer results: Magnetopause observations, *Space Sci. Rev.*, *22*, 681, 1978.
Russell, C. T., R. L. McPherron, and P. J. Coleman, Fluctuating magnetic fields in the magnetosphere, *Space Sci. Rev.*, *12*, 810, 1972.
Sato, T., and A. Hasegawa, Externally driven reconnection versus tearing mode instability, *Geophys. Res. Lett.*, *9*, 52, 1982.
Scarf, F. L., and D. A. Gurnett, A plasma wave investigation of the Voyager mission, *Space Sci. Rev.*, *21*, 289, 1977.
Sentman, D. D., M. F. Thomsen, S. P. Gary, W. C. Feldman, and M. M. Hoppe, The oblique whistler instability in the earth's foreshock, *J. Geophys. Res.*, *83*, 2048-2056, 1983.
Smith, E. J., and B. T. Tsurutani, Magnetosheath lion roars, *J. Geophys. Res.*, *81*, 2261, 1976.
Sonnerup, B. U. Ö., Magnetopause and boundary layer, in *Physics of Solar Planetary Environments*, edited by D. J. Williams, p. 541, AGU, Washington, D. C., 1976.
Sonnerup, B. U. Ö., Magnetic field line reconnection, in *Solar System Plasma Physics*, vol. III, edited by C. F. Kennel, L. J. Lanzerotti, and E. N. Parker, pp. 47-108, North-Holland, Amsterdam, 1979.
Stenzel, R. L., Whistler wave propagation in a large magnetoplasma, *Phys. Fluids*, *19*, 857-864, 1975.
Stenzel, R. L., and W. F. Daley, Large indirectly heated, oxide-coated cathode for producing uniform plasmas, United States Patent 4,216,405, August 1980.
Stenzel, R. L., and W. Gekelman, Laboratory Experiments on Magnetic Field Line Reconnection, in *Proceedings of XV International Conference on Phenomena in Ionized Gases 1981*, Part III, pp. 46-59, USSR Academy of Sciences, Minsk, USSR, 1981a.
Stenzel, R. L., and W. Gekelman, Magnetic field line reconnection experiments, 1, Field topologies, *J. Geophys. Res.*, *86*, 649-658, 1981b.

Stenzel, R. L., W. Gekelman, and N. Wild, Magnetic field line reconnection experiments, 4, Resistivity, heating, and energy flow, *J. Geophys. Res.*, *87*, 111–117, 1982.

Stenzel, R. L., W. Gekelman, and N. Wild, Electron distribution functions in a current sheet, *Phys. Fluids*, *26*, 1949–1952, 1983a.

Stenzel, R. L., W. Gekelman, and N. Wild, Magnetic field line reconnection experiments, 5, Current disruptions and double layers, *J. Geophys. Res.*, *88*, 4793–4804, 1983b.

Stenzel, R. L., W. Gekelman, N. Wild, J. M. Urrutia, and D. Whelan, Directional velocity analyzer for measuring electron distribution functions in plasmas, *Rev. Sci. Instrum.*, *54*, 1302–1310, 1983c.

Storey, L. R. O., An investigation of whistling atmospherics, *Phil. Trans. R. Soc. London Ser. A.*, *246*, 113–141, 1953.

Sudan, R. L., and J. Denavit, VLF emissions from the magnetosphere, *Phys. Today*, *26* 32–39, 1973.

Tanaka, M., and T. Sato, Simulations on lower hybrid drift instability and anomalous resistivity in the magnetic neutral sheet, *J. Geophys. Res.*, *86*, 5541–5552, 1981.

Taylor, J. R., *An Introduction to Error Analysis*, University Science Books, Mill Valley, Calif., 1982.

Tsuruda, K., and M. Ikeda, Comparison of three different types of

VLF direction finding techniques, *J. Geophys. Res.*, *84* 5325–5332, 1979.

Tsurutani, B. T., E. J. Smith, R. R. Anderson, K. W. Ogilvie, J. D. Scudder, D. N. Baker, and S. J. Bame, Lion roars and nonoscillatory drift mirror waves in the magnetosphere, *J. Geophys. Res.*, *87*, 6060–6072, 1982.

Vasyliunas, V. M., Theoretical models of magnetic field line merging, 1, *Rev. Geophys. Space Phys.*, *13*, 303, 1975.

Whelan, D., and R. L. Stenzel, Electromagnetic wave excitation in a large laboratory beam-plasma-system, *Phys. Rev. Lett.*, *47*, 95–98, 1981.

Wild, N., W. Gekelman, and R. L. Stenzel, Resistivity and energy flow in a plasma undergoing magnetic-field-line reconnection, *Phys. Rev. Lett.*, *46*, 339–342, 1981.

W. Gekelman and R. L. Stenzel, Department of Physics, University of California, Los Angeles, CA 90024.

Measurement and Instability Analysis of Three-Dimensional Anisotropic Electron Distribution Functions

W. Gekelman and R. L. Stenzel

University of California, Department of Physics, Los Angeles, California 90024

(Received 14 February 1985)

A velocity analyzer with high angular resolution ($d\Omega/4\pi = 10^{-4}$) has been used to measure the electron distribution function $f(v, \theta, \phi)$ in a neutral sheet of a large laboratory plasma. Contours of $f(v) = $ const form surfaces in velocity space. As $f(v)$ decreases, anisotropic tails form detached surfaces which send filaments out toward the main body. The highly anisotropic structures occur at the Doppler-shifted phase velocity of observed whistler-wave turbulence. Instability analysis of $f(v)$ is consistent with the observed whistler- and Langmuir-wave turbulence.

The interplay between waves and particles is one of the most fundamental processes in plasma physics. In a well-diagnosed laboratory plasma it is now possible to measure the dispersion and propagation $\omega(\mathbf{k})$ of unstable waves as well as the three-dimensional particle distribution functions. Such basic measurements are of general interest in and may be extrapolated to fusion and space plasmas (loss-cone distributions, beams, and double layers).

The experiments are performed in a large linear-discharge plasma ($\langle n_e \rangle \simeq 10^{12}/\text{cm}^3$, $kT_e \simeq 10$ eV, He pressure $= 10^{-4}$ Torr, 1-m diam ×2-m length).[1] In addition to a dc axial magnetic field $B_{0y} = 10$ G, a transverse magnetic field with a vacuum neutral line ($B_x = B_z = 0$) is applied by the pulsing of parallel currents (20 kA, 100 μs) through two external electrodes. In vacuum the topology of this field is an X point; the field lines in the center of any transverse plane intersect at 90°. When plasma is present, however, the changing magnetic field induces a current which assumes the form of a sheet ($\Delta x = 40$ cm wide, $\Delta z = 5$ cm half width, $I_p \simeq 1000$ A). The measured ensemble-averaged magnetic-field topology in the plasma [Fig. 1(a)] is that of a classical neutral sheet. The electron-distribution function is measured with a highly directional velocity analyzer[2] which can be placed at any position x within the neutral sheet or in the strong transverse-field regions [$|x| \geq 15$ cm] on its border. The mounting of the analyzer on a double shaft provides for variation in the polar angle θ while the probe rotation yields the variation in ϕ. Every second (the experimental repetition time) the digitized current-voltage trace ($\tau_{\text{sample}} = 10$ ns) is transported by a high-speed network from the data-acquisition computer (LSI 11/23) to a VAX 11/750 computer and on-line array processor (MAP 300). The data are smoothed by use of convolution techniques and differentiated; the result is proportional to $v^2 f(v)$. The plasma potential, which can fluctuate from shot to shot within the turbulent current sheet, is calculated and $f(v)$ is shifted accordingly. The procedure developed ensures that the distributions, averaged over an ensemble of ten shots, measured at 432 angles match at the origin. After completion of a run the data can be shipped over a second network for further analysis and graphics using a larger (Cray) computer.

The display of $f(v_x, v_y, v_z)$ presents a fundamental problem since four orthogonal axes are required. A reduced distribution $f(v_\parallel, v_\perp)$ can be displayed as a surface[3] but this defeats the purpose of the measurement by imposing symmetry. If one notes that in three dimensions "cuts" through $f(v, \theta, \phi)$ produce surfaces of constant $f(v)$, the distribution function may be visualized by inspection of a sequence of these surfaces. In this case $f(v)$ is measured on the center of the current sheet ($x = 0$, $z = 0$) 30 μsec into the reconnection event. In Fig. 2(a) the surface $C = f(v)/f(0) = 2.5 \times 10^{-2}$ is a sphere indicating that the bulk of the distribution is Maxwellian. As $C \to 0$ the configuration surface reflects the presence of faster particles. The detached surfaces in Fig. 2(b) denote beamlets of fast particles (an electron beam with velocity greater than a Maxwellian main body would give rise to two spheres in velocity space). A continued scan to values of C as low as 10^{-4} is possible since the electron currents are as large as $I_{\text{tail}}/I_{\text{tot}} \sim 0.3$ and the digitizers have 0.4% accuracy. (Transformation into velocity space entails a division by v^2.)

As C decreases several additional beamlets appear. The beamlets appear to "grow" filaments which connect them to each other and the main body. Inspection of these surfaces indicates that some fast particles have velocities directed oblique to the local magnetic field. The continuous development of these structures as well as rotations about various axis in velocity space is best shown in a computer-generated movie.[4] If the probe is moved into a region of appreciable transverse field ($|x| \geq 15$, $z = 0$) no fast particles are observed; the surfaces are all spherical.

Although anisotropies in velocity space have been previously observed by our group,[5] new techniques in data reduction and the ability to store and process huge
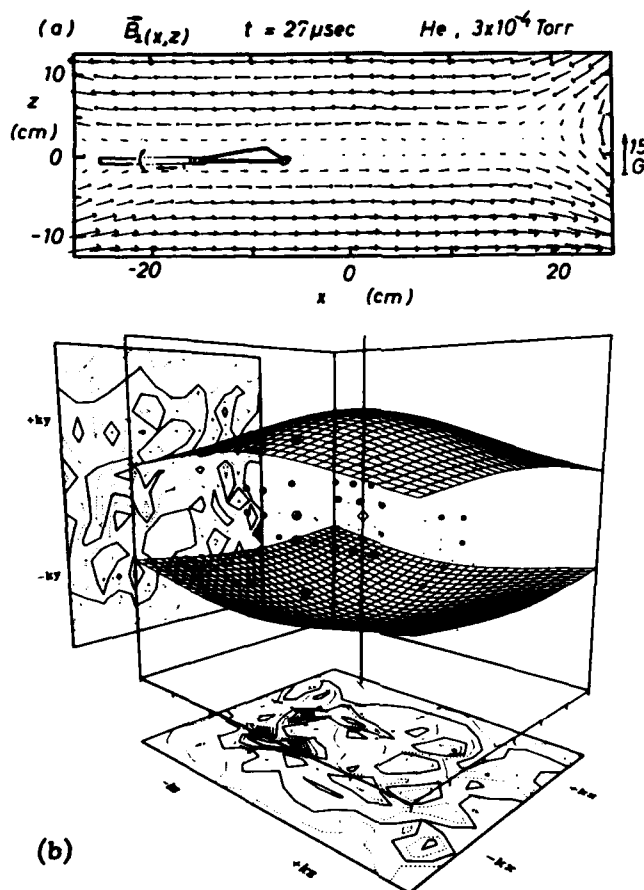
FIG. 1. (a) Linear vector plot of $\mathbf{B}_\perp$ showing the neutral-sheet magnetic field topology for a ten-shot ensemble average. Sketch shows location of velocity analyzer. (b) Three-dimensional wave-number spectrum at $f = 1$ MHz for one component of the cross-spectral-function tensor $B_{x1}B_{z2}$. The bottom and side plots are wave spectra in the k_y-k_x and k_z-k_x planes. The markers with size proportional to amplitude are projections of the peaks in k space. The bounding surfaces are the cold-plasma dispersion curves for oblique whistlers at $B_y = 10$ G, $n_e = 4.9 \times 10^{12}$/cm^3. The vertical line is drawn through $k_x = k_y = 0$. The diamond in the center is at $\mathbf{k} = 0$. The prolific mode structure falls within the limiting dispersion surfaces.

arrays of data allow us to report these detailed structures for the first time.

The number of particles per unit solid angle is $v^2 f(v)$ which strongly weights the energetic ones in calculation of the moments

$$\int_0^\infty \int_0^{2\pi} \int_0^\pi v^\alpha f(v, \theta, \phi) v^2 \sin\theta \, d\theta \, d\phi \, dv.$$

The ratio of tail to main body density $n_{\text{tail}}/n_{\text{tot}} = 0.015$ is calculated for $\alpha = 0$. The higher moments are, for $\alpha = 1$, current density $J_x = 0.72$, $J_y = -1.58$, $J_z = -0.18$ A/cm^2; for $\alpha = 2$, mean energy Tr(E) $= 10.5$ eV with off-axis components 10^{-2} times axial ones; and for $\alpha = 3$, heat flux $Q_x = 1.8$, $Q_y = 91.1$, $Q_z = -7.6$ W/cm^2. The local current is predominantly in the direction of the axial magnetic field and agrees with other measurements. The temperature of 10.5

eV indicates that the fast electrons, $v_\parallel \geq 4 \times 10^8$ cm/sec, have run away in response to the induced parallel electric field.[6] The axial heat flux is carried mainly by the runaways.

We believe that the complex structure observed in velocity space may be qualitatively explained by two effects. In the center of the current sheet the trajectory of a single collisionless electron is a spiral as $B = B_{y0}$. However, electrons arriving at the detector originate at a variety of spatial locations and have complicated orbits[7] which may not average out to yield a uniform velocity distribution in the beam direction. Perhaps more interesting are wave-particle interactions which redistribute electrons whose phase velocities match those of unstable waves. There is a great deal of evidence for this in the neutral sheet.
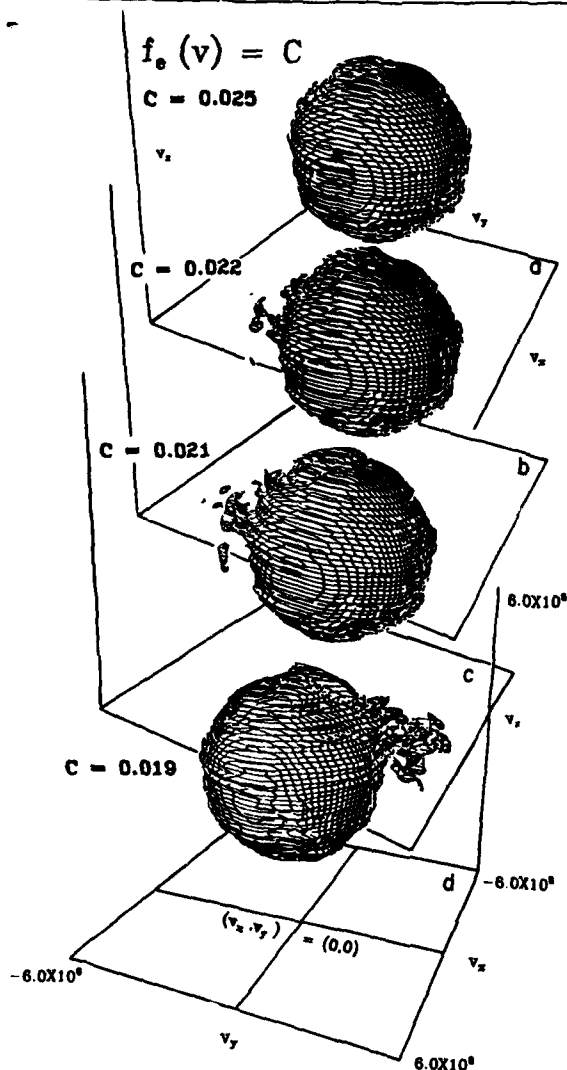
2415

FIG. 2. Surfaces in velocity space of $f_e(v_x, v_y, v_z)$ $= C =$const, $f_e(\mathbf{v}=0)=1.0$. Probe is located in the center of the neutral sheet. $B_{y0}=10$ G. (a) $C=$const$=0.025$. The surface is spherical indicating that the bulk of the particles is Maxwellian. (b) $C=0.022$. (c) $C=0.021$. The distortions and beamlets mark the presence of electrons in the electric field, $E_y \parallel B_{y0}$, of the current sheet. (d) $C=0.019$ viewpoint changed to $-v_x$ direction to reveal filamentary structure.

The ensemble-averaged magnetic field is somewhat deceiving; within the neutral sheet the magnetic fields exhibit large fluctuations $\delta B_\perp / |B_\perp| \sim 1$. The broad frequency spectrum peaks near the lower hybrid frequency ($f_{LH} \simeq 200$ kHz) and extends to the electron-cyclotron frequency. A detailed study of the instability growth was not done since it fully saturates within several wave periods. Extensive correlation measure-
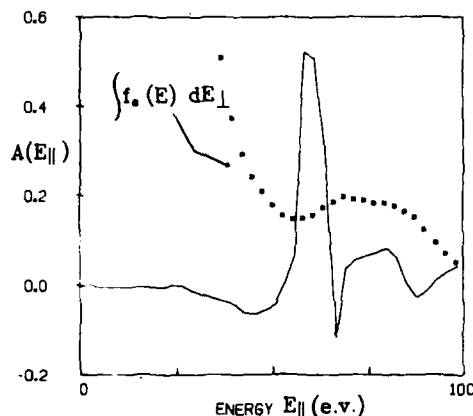
FIG. 3. Plot of parameter $A(E_{\parallel})$ (solid line), Eq. (2), evaluated from the distribution function shown in Fig. 2. $A > 0.04$ is an indication of sufficient anisotropy to destabilize parallel whistler waves. The dotted curve indicates a positive slope exists in $\int f_e dE_\perp$ at tail energies sufficiently high to destabilize Langmuir waves.

ments have been performed and the cross-spectral-function tensor evaluated.[8] The measurements indicate that at fixed ω the wave number k depends on angle as summarized in Fig. 1(b). Data from two orthogonal planes $(x\text{-}y, x\text{-}z)$ were used to construct the three-dimensional wave-vector spectrum. Shown is the multimode structure of one component of the cross-spectral tensor at a fixed frequency ($f=1$ MHz). The dispersion surfaces for oblique whistlers,[9]

$$kc/\omega \simeq \omega_p^2 / \omega(\omega_c \cos\theta - \omega),\qquad (1)$$

fill a volume of $\mathbf{k}$ space since ω_c, ω_p vary throughout the reconnection region.[10,11] No random waves are observed outside the surfaces described by Eq. (1) for the experimental extrema ($n_e = 4.9 \times 10^{12}$ cm^{-3}, $B = 10$ G). Tests on a number of these modes have established that they are right-hand circularly polarized.

The measured phase velocity of the Doppler-shifted whistlers $|\omega - \omega_c|/k_{\parallel} \simeq 4.3 \times 10^8$ cm/sec, ($\langle k_{\parallel}\rangle \simeq 0.6$ cm^{-1}) falls into the range of the observed tail. An anisotropy test which indicates that the measured electron-distribution function is prone to a parallel whistler instability[12] is that $A(E_{\parallel}) > (\omega_c/\omega - 1)^{-1}$ where

$$A(E_{\parallel}) = \frac{\int_0^\infty E_\perp (\partial f/\partial E_\perp - \partial f/\partial E_{\parallel}) dE_\perp}{\int_0^\infty f(E) dE_\perp}.\qquad (2)$$

This expression has been evaluated and $A(E_{\parallel})$ is shown in Fig. 3. In a range of energies the instability criterion $A(E_{\parallel}) > A_c \simeq 0.04$ is satisfied. The maximum is at $v_{\parallel} \simeq 4.7 \times 10^8$ cm/sec, close to the phase velocity of parallel whistlers.

The reduced parallel distribution, $g(v_{\parallel})$

$= \int f(E) dE_\perp$ [denominator of Eq. (2)], is also shown in Fig. 3. It exhibits a positive slope which satisfies the criterion for Cherenkov instabilities (oblique whistlers, Langmuir waves, etc.). Measurements of the microwave emission with horn antennas[8] have shown a strong peak at the plasma frequency $f \simeq f_p \simeq 12$ GHz, indicative of beam-driven strong Langmuir turbulence.[13]

A more general expression to test for growth of oblique whistlers[12] has been used with measurements of two-dimensional distribution functions in the Earth's bow shock.[14] Although whistler noise is observed in the shock transition region it is not possible to measure wave-number spectra and wave dispersion in space, and distribution measurements are insensitive at low energies within the main body. A number of interesting computer simulations along these lines have been carried out[15,16] and have shown the importance of trapped particles in the deformation of $f(v)$. Roux and Pellat[17] have shown analytically that a beam or hole is formed in the distribution function at the whistler resonant velocity. We are presently extending our analysis to examine the growth of the observed oblique whistler modes.

In this work we have pointed out that the structure of the electron distribution function in a turbulent, current-carrying magnetoplasma is rich in detail. It is long known that particles resonant with waves are scattered in velocity space as they interact with them. We have observed this to occur in three dimensions when oblique whistler-wave turbulence is present. Since faster particles heavily weight the moment calculations, the presence of low-density tails can greatly affect transport processes such as heat flux. We believe that the complex anisotropies discovered in velocity space are of great consequence in diffusion and transport.

[1]W. Gekelman and R. L. Stenzel, Phys. Scr. T2, 277–287 (1982).

[2]R. L. Stenzel et al., Rev. Sci. Instrum. 54, 1302–1310 (1983).

[3]R. L. Stenzel, W. Gekelman, and N. Wild, Phys. Fluids 26, 1949–1952 (1983).

[4]W. Gekelman, Bull. Am. Phys. Soc. 29, 1317 (1984).

[5]R. L. Stenzel and W. Gekelman, Physica (Utrecht) 12D, 133–144 (1984); Adv. Space Res. 4, 459 (1984).

[6]H. Dreicer, Phys. Rev. 115, 238–249 (1959).

[7]P. L. Rothwell and G. K. Yates, Geophys. Monogr. 30, 51–60 (1984).

[8]W. Gekelman and R. L. Stenzel, J. Geophys. Res. 89, 2715–2733 (1984).

[9]R. A. Helliwell, Whistlers and Related Ionospheric Phenomena (Stanford Univ. Press, Stanford, California, 1965).

[10]R. L. Stenzel and W. Gekelman, J. Geophys. Res. 86, 649 (1981).

[11]W. Gekelman and R. L. Stenzel, J. Geophys. Res. 86, 659 (1981).

[12]C. F. Kennel and H. V. Wong, J. Plasma Phys. 1, 75 (1967).

[13]D. A. Whelan and R. L. Stenzel, Phys. Fluids 28, 958 (1985).

[14]D. D. Sentman et al., J. Geophys. Res. 88, 2048 (1983); R. L. Tokar, D. A. Gurnett, and W. C. Feldman, J. Geophys. Res. 89, 105 (1984).

[15]H. Matsumoto and Y. Omura, Geophys. Res. Lett. 10, 607 (1983).

[16]J. P. Matthews, Y. Omura, and H. Matsumoto, J. Geophys. Res. 89, 2275 (1984).

[17]A. Roux and R. Pellat, J. Geophys. Res. 83, 1433 (1978).

LABORATORY EXPERIMENTS ON CURRENT SHEET DISRUPTIONS, DOUBLE LAYERS TURBULENCE AND RECONNECTION

R. L. Stenzel and W. Gekelman
Department of Physics, University of California, Los Angeles,
CA 90024

ABSTRACT

The role of laboratory experiments to the understanding of current systems in space plasmas is reviewed. It is shown that laboratory plasmas are uniquely suited to make detailed investigations of basic physical processes in current-carrying plasmas. Examples are given for double layers, current-driven instabilities, and the plasma dynamics at magnetic neutral points during reconnection. Observations of current sheet disruptions show the coupling between local plasma phenomena (double layers) and global circuit properties (magnetic energy storage).

INTRODUCTION

Although laboratory plasmas and astrophysical plasmas consider a vastly different parameter regime, unstable current systems are encountered in both cases. Although the observational methods are opposite, local versus remote, there is evidence for common physical processes: instabilities, plasma energization, reconnection. The investigation of these processes from various viewpoints contributes to the general understanding even though a one-to-one correspondence is often not established.

Carefully designed laboratory experiments establish stable plasmas with simple, known boundary conditions, and a variety of diagnostic tools for in-situ time and space resolved measurements of fields, waves, particle distributions. These features are especially suited for observing localized processes such as double layers which have been well established in the laboratory (Torvén, 1979; Sato, 1982). Similarly, electrostatic and short-scale length electromagnetic turbulence has been successfully studied in many laboratory plasmas carrying currents (Gekelman and Stenzel, 1978; Hollenstein and Guyot, 1983; Stenzel, 1977; Gekelman and Stenzel, 1983). The investigation of magnetic reconnection requires plasmas of larger dimensions, on the order of the ion

47

collisionless skin depth c/ω_{pi}. In earlier investigations (Baum and
Bratenahl, 1980; Frank, 1976; Ohyabu et al., 1974) this has been esta-
blished by high densities ($n_e \simeq 10^{15}$ cm^{-3}) and small physical sizes
(1 ... 10 cm) which makes the diagnostics difficult. Recent reconnec-
tion experiments at UCLA (Stenzel and Gekelman, 1979; Gekelman et al.,
1982; Stenzel et al., 1983a) have the opposite approach; large scales
(1 ... 2m) and medium densities ($n_e = 10^{12}$ cm^{-3}) so as to optimize the
diagnostic aspect. In these experiments a classical magnetic neutral
sheet has been established; reconnection and particle energization are
observed facts. The current sheet associated with the magnetic topol-
ogy of a flattened X-point exhibits microscopic instabilities (magnetic
turbulence) and macroscopic instabilities (current disruptions). The
latter case is most interesting since reconnection, current sheet
disruptions and double layers occur simultaneously. It is an example
of the complicated but probably realistic nonlinear plasma dynamics at
magnetic null points which also requires the knowledge of the global
circuit properties.

EXPERIMENTAL CONFIGURATION

    The UCLA reconnection experiments are performed in a device shown
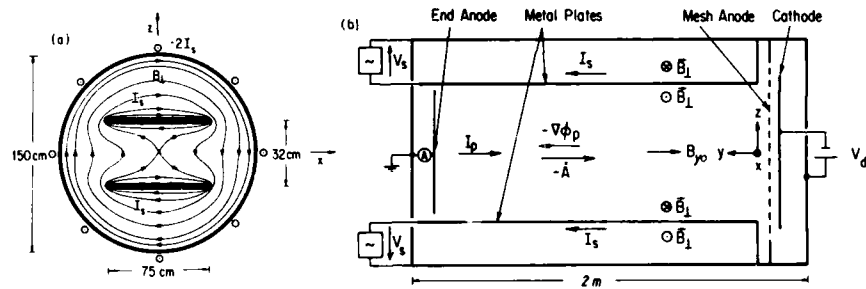schematically in Fig. 1. A linear discharge plasma column is generated

Fig. 1. Schematic picture of the experimental arrangement. (a) Cross-
sectional view showing parallel plate electrodes with pulsed currents
I_s and magnetic field lines $\vec{B}_\perp$ without plasma. (b) Side view of the
device with main electrodes, currents (I_p, I_s) electric fields
($\vec{E} = \vec{A} - \nabla\phi_p$), and magnetic fields ($\vec{B} = \vec{B}_\perp + \vec{B}_{yo}$). The coordinate
system common in magnetospheric physics has been adopted where y is
along the neutral line (device axis), x is along the horizontal neutral
sheet, and z is normal to the sheet.

with a 1 m diameter cathode. Detailed plasma diagnostic tools are
employed in conjunction with a state-of-the-art digital data processing
system. Time and space resolved probe measurements of fields ($\vec{E}$, $\vec{B}$),

plasma properties (n_e, T, ϕ, $\vec{v}$) and distributions [$f(\vec{v}, \vec{r}, t)$] are
performed. The analog data are digitized with 100 MHz, 32K A-D con-
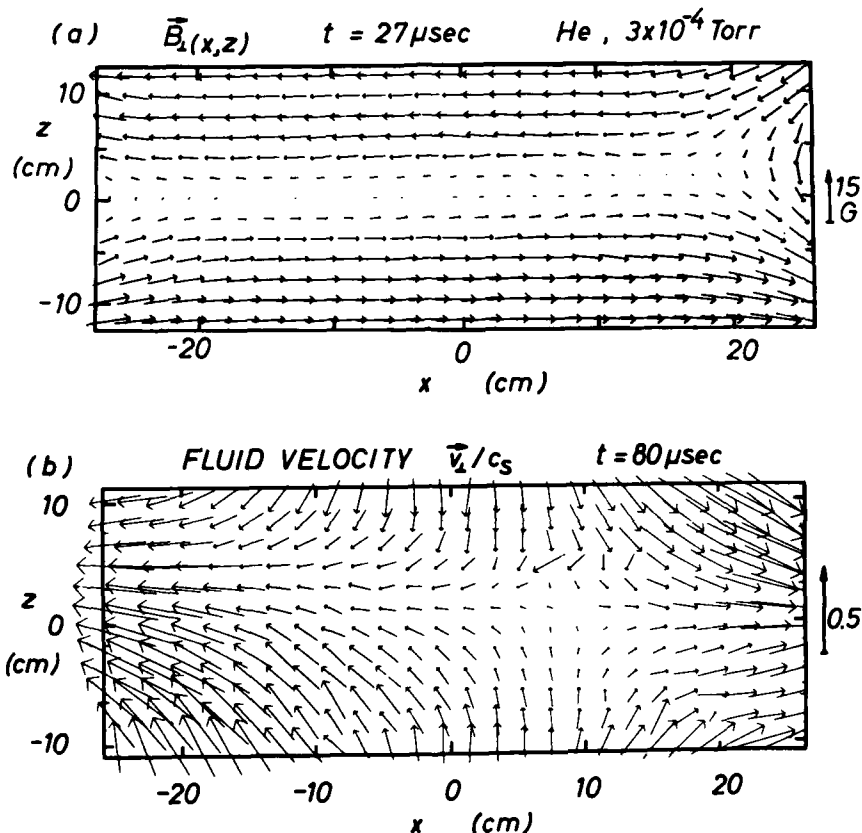verters, evaluated on-line with an array processor linked
to a Cray computer.

Fig. 2. Measured magnetic fields and flow field during reconnection.
(a) Transverse field $\vec{B}_\perp$ (x, z) at a fixed time t, position y = 137 cm,
showing the classical neutral sheet topology. (b) Transverse ion
flow velocity, $\vec{v}_\perp$ (x, z), normalized to the local sound or Alfvén
speed, $c_S = (kT_e/m_i)^{1/2} \simeq c_A = (B^2/2\mu_0 nm_i)^{1/2}$. Vertical compression
and horizontal jetting are in qualitative agreement witn reconnection
models.

        The plasma of typical density $n_e \simeq 10^{12}$ cm^{-3} and temperature
$T_e \simeq 10$ eV is uniform, quiescent, essentially collisionless, and highly
reproducible in pulses of duration $t_p \simeq 5$ msec, repeated every $t_r = 2$ sec.

71

After preparing the plasma in a uniform axial magnetic field ($B_y \simeq$ 10G) . a pulsed transverse magnetic field ($<B_\perp> \simeq$ 10G) is applied. Its topology vacuum contains an X-type neutral point along the axis of the device. In the presence of plasma, electron currents are induced which flow preferentially in regions of $B_\perp \simeq 0$. They are so large ($I \simeq$ 1000A) as to modify the field topology self-consistently, forming a Dungey (1958) type neutral sheet during the interval of rising applied fields ($0 < t \le 100\mu$sec) shown in Fig. 2a. The corresponding current sheet ($\vec{J} = \nabla \times \vec{B}/\mu_0$) has a thickness ($\Delta z \simeq$ 5cm) between the

$$V_{adc} = 10V$$

$$ARGON, \ 10^{-4} \ TORR$$

TIME t (10 μsec/div)
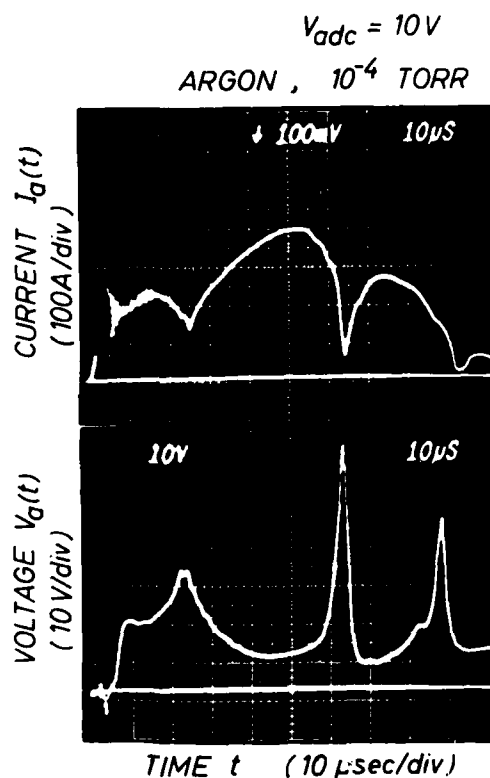
Fig. 3. Disrupted center plate current $I_{a(t)}$ (top trace) and instantaneous plate voltage $V_{a(t)}$ (bottom trace) measured in situ. At each disruption a voltage spike is generated owing to the distributed circuit inductance L. Note that $LdI_a/dt >> V_{adc} = 10V$.

collisionless electron skin depth ($c/\omega_{pe} \simeq 0.6$ cm) and the ion Larmor radius ($r_{ci} \simeq 30$ cm). Thus, we are investigating the fine structure of the diffusion region which is beyond the resolution of present

72

solar observations and has neither been observed in the magnetosphere. Reconnection occurs in our experiment at a rate indicated by the axial electric field along the separation ($E_y \approx 0.5$ V/cm) (Sonnerup, 1979) or the normalized inflow velocity of the fluid into the field reversal region ($v/v_A \approx 0.3$) shown in Fig. 2b (Vasyliunas, 1975). For uniform plasmas and modest current densities (normalized electron drifts $v_d/v_e \approx 0.1$) the current sheet is macroscopically stable on a time scale long compared with the Alfvén transit time across the sheet.

CURRENT DISRUPTIONS AND DOUBLE LAYERS

The stability of the current sheet with respect to increasing current densities at the separator has been investigated. This is accomplished by raising the potential of the central portion of the end anode on which the plasma terminates axially. When monitoring collected current I_a to this center electrode, we find that at increasing current densities ($v_d/v_e \gtrsim 0.3$) spontaneous current disruptions develop (see Fig. 3a). The cause for this current switch-off has been inferred from detailed diagnostics of the local plasma properties. During a disruption the plasma potential rises in the perturbed current channel to a value much larger than the dc potential ($V_{dc} \approx 10$V) applied to the end plate (see Fig. 3b). Simultaneously, the plasma density decreases. These processes have a finite axial extent. In particular, the plasma potential exhibits an abrupt axial drop ($\Delta\phi \approx 30$V in $\Delta y \approx 5$mm $\approx 100\lambda_D$), i.e., a double layer is formed in the region where the current is disrupted.
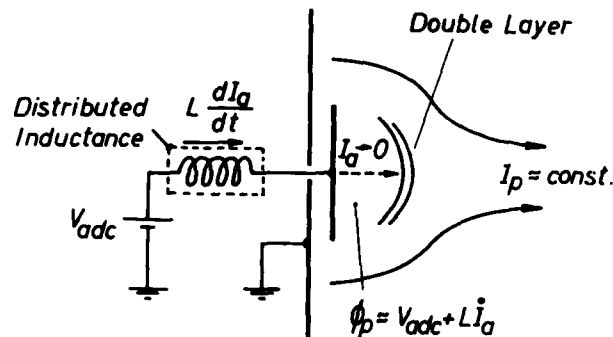

Fig. 4. Schematic diagram of the important elements in the physical model for the disruptive instability

The large positive plasma potential can only be explained in terms of the circuit properties. Fig. 4 shows schematically that the extended current path has a distributed inductance L which, in the presence of a current drop results in an inductive voltage rise LdI/dt.

73

This voltage drives the plasma potential positive and causes an
expulsion of ions, hence a density and current drop. The current
decrease in turn reinforces the inductive voltage so that an explosive
disruption develops. The current lost in the center of the original
sheet is redirected to the sides.

At the double layer particles are accelerated on expense of magne-
tic field energy stored at different locations in the current system.
The kinetic energy first resides in particle beams. Subsequent beam-
plasma instabilities transfer the directed energy into waves and heat.
For example, microwave emissions at the electron plasma frequency
are caused by electron beam-plasma interactions (Whelan and Stenzel,
1981).

Many of the observed phenomena of current sheet disruptions may
apply to space plasmas as well. The dynamic current modifications
during substorms and solar flares accelerate particles to high energies.
The formation of field aligned potential structures is well known
from auroral physics but it is possible that nonstationary double
layers arise from inductive voltages where the energy storage is
remote from the region of dissipation. Type III solar radio bursts
involve beam-plasma instabilities possibly analogous to the present
emission process.

TURBULENCE IN CURRENT SHEETS

Even in the absence of current disruptions the macroscopically
stable neutral sheet exhibits a significant level of turbulence.
Currents in collisionless plasmas create various fluid and kinetic
instabilities (Das, 1981). The first step in the observation of
turbulence is the mode identification from the frequency and wave-
number spectrum. Then, the instability mechanism has to be isolated
which involves particle distribution measurements. Finally, the effect
of the instability on the macroscopic transport properties is of
interest. Some of these questions have been addressed in the present
experiment.

Three characteristic modes have been identified. An enhanced
level of microwave emissions in the range of plasma frequencies
($6 \leq f \leq 12$ GHz) is observed during reconnection (see Fig. 5 top).
These nonthermal emissions are due to electron plasma waves excited
by energetic electrons. A second spectrum of waves below the ion
plasma frequency has been investigated (Fig. 5 bottom). With two-probe
cross-correlation measurements the dispersion $\omega(k)$ is obtained which
identifies the noise to consist of ion acoustic modes ($\omega \simeq kc_s$).
Finally, low frequency magnetic fluctuations above the lower hybrid
frequency ($f_{\ell h} \simeq 200$ kHz) are observed (Fig. 6a) and studied in depth.

74

MICROWAVE EMISSION

$$E^2$$

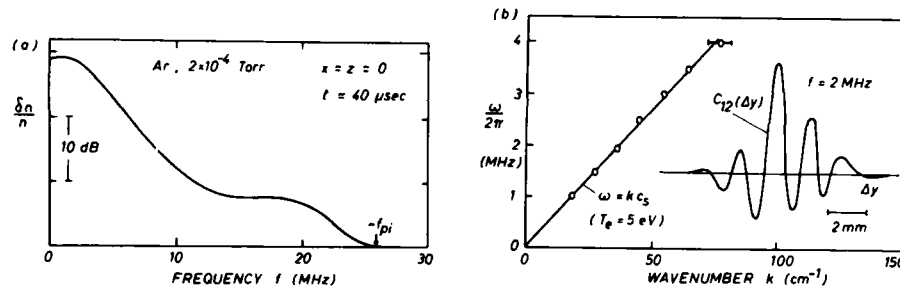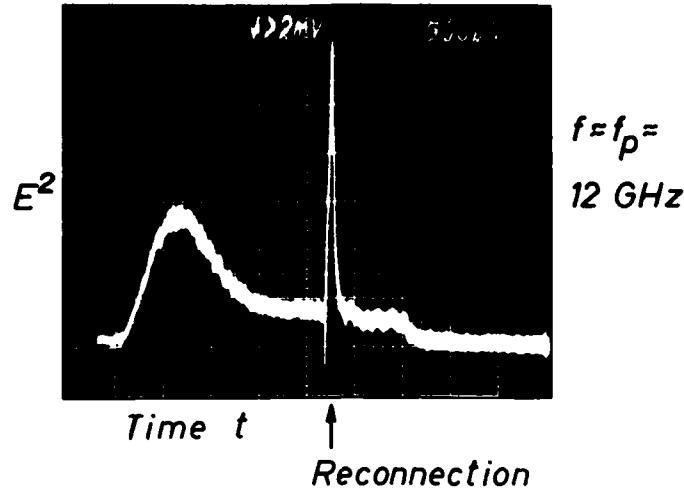$$f \approx f_p \approx$$

$$12\ GHz$$

Time t

↑

Reconnection

Fig. 5. Turbulence spectra in a current sheet. Top: Microwave
emission near the electron plasma frequency is greatly enhanced during
the reconnection pulse. Bottom: (a) Electrostatic turbulence spectrum
below the ion plasma frequency (~25 MHz) sampled during reconnection.
(b) Dispersion relation $\omega(k)$ obtained from measured cross-correlation
functions (see insert) identifies spectrum to consist of ion acoustic
modes.

The nonstationary magnetic turbulence is analyzed by ensemble
averaging two-probe vector cross-correlations. Digital Fourier
analysis in time and space reveals a multitude of modes which fall
near the average dispersion surface for whistler modes (Fig. 6b). By
selecting individual modes the polarization properties $\vec{B}(\Delta \vec{r}, \Delta t)$
are found to be right hand circular, confirming that the modes are
indeed whistlers.

75

(a)   ω Spectrum

$\dot{B}_x$

0   0.5   1
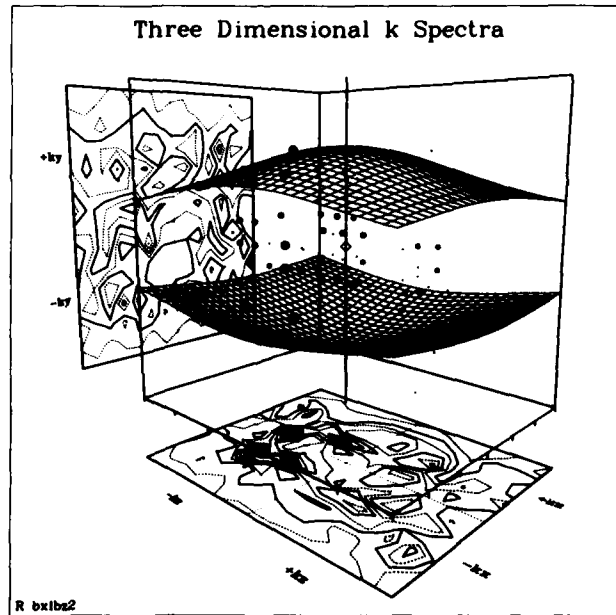ω/2π   (MHz)

Three Dimensional k Spectra

R bxlbz2
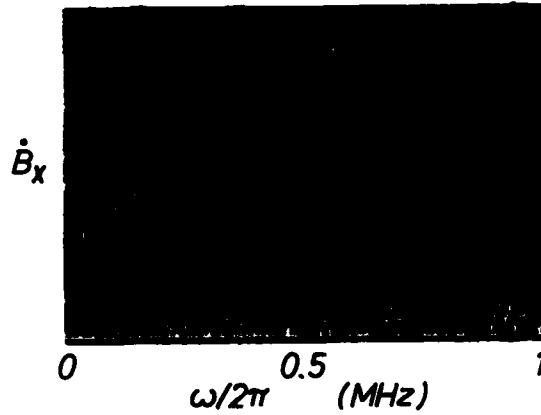
Fig. 6. Magnetic turbulence in a current sheet. (a) Frequency spectrum
(lower hybrid $\omega_{\ell h}/2\pi \simeq 0.1$ MHz; electron cyclotron $\omega_{ce}/2\pi \simeq 30$ MHz).
(b) Three-dimensional wave vector $\vec{k}$ space with unstable modes of
the magnetic turbulence. The cross spectral function $<B_{x1} B_{z2}>$ at f = 1
MHz has been measured in two orthogonal planes and spatially Fourier
transformed. The data points are scattered around the theoretical
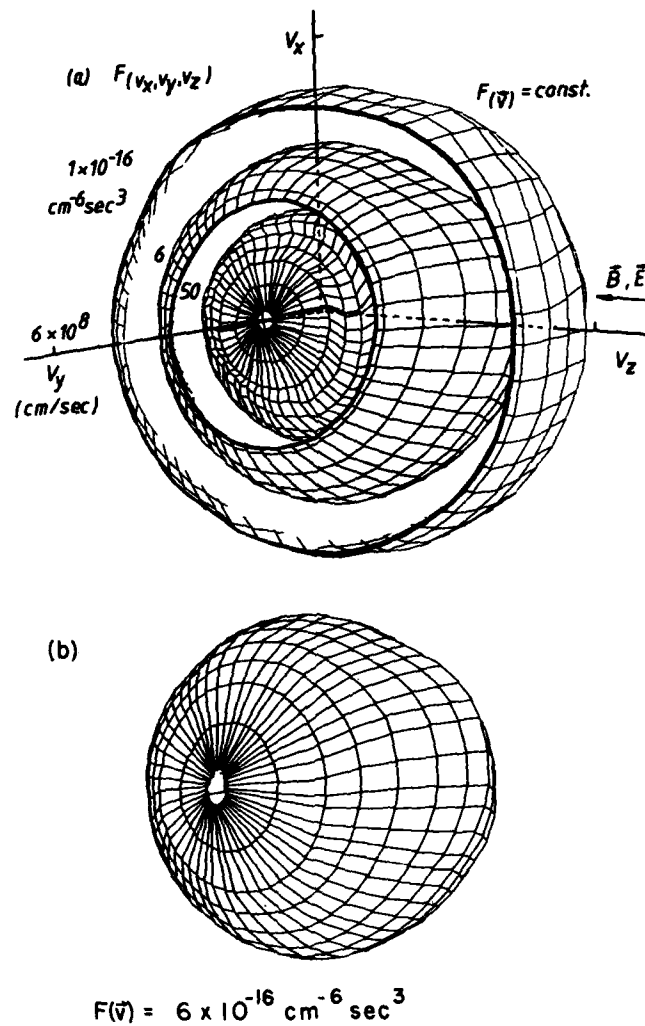dispersion surfaces of whistler waves.

76

Fig. 7. Display of the distribution function in three-dimensional
velocity space as surfaces of constant $f(v_x, v_y, v_z)$. (a) Three
nested surfaces cut for purpose of display. Radius expands with
decreasing value of $f(\vec{v})$. (b) Complete display of the middle surface
showing velocity space anisotropy (nonspherical shape) due to
runaway electrons in a current sheet.

77

Since whistler instabilities can arise from velocity space
anisotropies we have investigated the electron velocity distribution
function. These measurements are performed with a novel velocity
analyzer with good angular resolution ($\Delta\Omega \simeq 10^{-2}$ sterad) (Stenzel et al.,
1983b). The three-dimensional distribution $f(v_x, v_y, v_z)$ is
displayed in Fig. 7a as surfaces of constant value f, which are nested
with the maximum ($f_{max} \simeq 10^{-14}$ cm^{-6} sec^3) near the origin ($v = 0$).
Anisotropies cause deviations from spherical surfaces, clearly
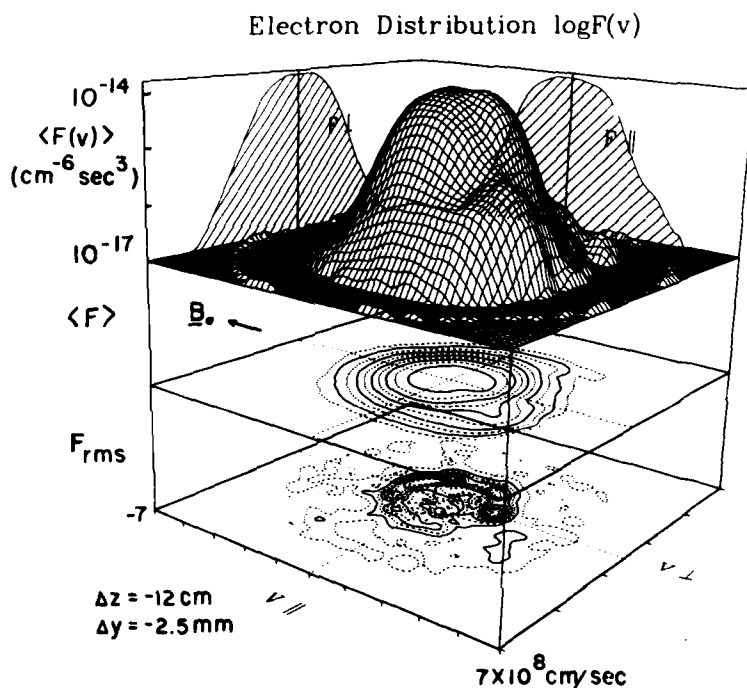visible for the contour $f = 6 \times 10^{-16}$ cm^{-6} sec^3 displayed separately
in Fig. 7b.

Electron Distribution logF(v)

Fig. 8. Comparison of ensemble average distribution $<f(\vec{v})>$ and root-
mean-square fluctuations $f(\vec{v})_{rms}$. Upper panel shows the mean $\log_{10}$
$<f(v_{||}, v_\perp)>$ and two one-dimensional cuts, $\log_{10} <f(v_{||}, 0)>$ and
$\log_{10} <f(0, v_\perp)>$. Middle plane shows contours of constant $<f(v_{||}, v_\perp)>$.
3 dB per contour. Lower plane shows fluctuations f_{rms} $(v_{||}, v_\perp)$,
$\sim 4 \times 10^{-16}$ cm^{-6} sec^{+3} per contour. Note anisotropic distribution of
fluctuations with approx. maxima where $f(\vec{v})$ exhibits strong gradients.

The elongation along the magnetic field is produced by energetic
electrons which runaway in the electric field along the separator.
Runaway electrons are observed only inside the neutral sheet. At the
sheet edge the normal field component B_z prevents the free acceleration

78

•of electrons.

Kinetic instabilities can be predicted both from the shape of the average distribution function (e.g. $\partial f/\partial v > 0$) and by fluctuations in the distribution involving wave-particle resonances. From a large ensemble of repeated measurements we have determined both the mean value and the rms fluctuations which are displayed in Fig. 8 in a two-dimensional velocity space. Comparing the contour plots of f_{mean} $(v_{\parallel}, v_{\perp})$ and f_{rms} $(v_{\parallel}, v_{\perp})$ we find enhanced fluctuations near the anisotropic runaway electrons. The particle velocities correspond to the Doppler shifted phase velocities of unstable whistlers, and their fluctuation spectra overlap. Thus, the origin of the whistler wave turbulence appears to lie in the observed nonequilibrium distributions in the current sheet.

The complete knowledge of the distribution function $f(\vec{v}, \vec{r}, t)$ provides us with the space-time resolved fluid properties of which we have calculated the particle density, current density, mean energy and heat flow. Transport parameters have been studied with the help of an array probe which provides the bulk electron temperature with high time resolution (Wild, et al., 1983). Correlation analysis of temperature fluctuations in the current sheet indicate that heating occurs in bursts of short durations ($\Delta t \simeq 3\mu sec$) generated in narrow regions (≤ 3 cm diam.) propagating and diffusing across the field at approximately the Alfvén speed. Heat bursts correlate with current pulses. The cross-field heat conductivity is larger than the classical value. The microscopic heating and transport processes in collisionless plasmas undoubtedly involve plasma turbulence effects, but further investigations are required to understand the processes in detail. Laboratory plasmas are highly suited for this task.

ACKNOWLEDGMENTS

REFERENCES

Baum, P. J. and Bratenahl, A.: 1980, in C. Marton (ed.), Advances in Electrons and Electron Physics, Academic, New York, Vol. 54, p. 1.
Das, A. C.: 1981, in H. Kikuchi (ed.), Relation Between Laboratory and Space Plasmas, D. Reidel Publ. Co., Dordrecht, Holland, p. 241.
Dungey, J. W.: 1958, Cosmic Electrodynamics, Cambridge University Press, New York.
Frank, A. G.: 1976, Proc. P. N. Lebedev Phys. Inst. Acad. Sci. USSR Engl. Transl., 74, 107.

79

Gekelman, W. and Stenzel, R. L.: 1978, *Phys. Fluids* 21, 2014.
Gekelman, W., Stenzel, R. L., and Wild, N.: 1982, *Physica Scripta*
    T2/2, 277.
Gekelman, W. and Stenzel, R. L.: 1983, *J. Geophys. Res.* (submitted).
Hollenstein, Ch. and Guyot, M.: 1983, *Phys. Fluids* 26, 1606.
Ohyabu, N., Okamura, S., and Kawashima, N.: 1974, *J. Geophys. Res.*
    79, 1977.
Sato, N.: 1982, in P. Michelsen and J. J. Rasmussen (eds.), *Symposium
    on Plasma Double Layers, Risø National Laboratory, June 16-18, 1982,*
    Risø-R-472, p. 116.
Sonnerup, B. U. O.: 1979, in *Space Plasma Physics: The Study of the
    Solar System*, National Academy of Sciences, Washington D. C.,
    Vol. 2, p. 879.
Stenzel, R. L.: 1977, *J. Geophys. Res.* 82, 4805.
Stenzel, R. L. and Gekelman, W.: 1979, *Phys. Rev. Lett.* 42, 1055.
Stenzel, R. L., Gekelman, W., and Wild, N.: 1983a, *J. Geophys. Res.*
    88, 4393.
Stenzel, R. L., Gekelman, W., Wild, N., Urrutia, J. M., and Whelan, D.:
    1983b, *Rev. Sci. Instrum.* 54 (in press).
Torvén, S.: 1979, in P. J. Palmadesso and K. Papadopoulos (eds.),
    Wave Instabilities in Space Plasmas, D. Reidel, Hingham, Mass.,
    p. 109.
Vasyliunas, V. M.: 1975. *Rev. Geophys. Space Phys.* 13, 303.
Whelan, D. A. and Stenzel, R. L.: 1981, *Phys. Rev. Lett.* 47, 95.
Wild, N., Stenzel, R. L., and Gekelman, W.: 1983, *Rev. Sci. Instrum.*
    54, (in press).

DISCUSSION

Sonnerup: What is the ion gyroradius? What is the reconnection
rate?

Stenzel: The calculated ion Larmor radius is $r_{ci} \sim 30$ cm for Argon,
$r_{ci} \sim 10$ cm for Helium at $\langle B \rangle \sim 20$ G. The reconnection rate, as
determined by the observed upstream inflow velocity, is given by

$$M = \frac{v}{v_A} \sim 0.2.$$

Van Hoven: What is the driving electric field strength $(E/E_{Dreicer})$
when you show disruptions? Is there any E-field threshold for this
behavior?

Stenzel: We are in the regime where the electron drift velocity
approaches the thermal velocity or $E/E_{Dreicer} \sim 1$. There are no
disruptions observed for $v_d/v_e \sim 0.1$; they build up in the range
$0.2 \lesssim v_d/v_e \lesssim 1$.

Benford: Your 6 GHz radiation seems to be evidence for strong
electromagnetic emission near ω_p. What is the efficiency of this
radiation, and how does it compare, roughly, to microwave emission from
flaring loops and type III bursts?

Stenzel: Microwave signals at $f \sim f_p \sim 6$ GHz are observed both as
electrostatic signals in the beam-plasma region and as electromagnetic

80

waves outside the plasma. The mode conversion on density gradients and scattering off ion acoustic modes has a rather low efficiency, estimated to be $P_{em}/P_{es} \sim 10^{-4}$. I have pointed out the qualitative analogy between type III solar radio bursts and our ω_p emission which occur during impulsive reconnection events.

Sato: Can you distinguish between double-layer acceleration and the acceleration by reconnection (slow shocks, for example)?

Stenzel: Yes, the acceleration by the double layer is mainly in the direction of the separator (y-axis) while the acceleration due to the reconnection is in the direction of the neutral sheet (x-axis).

Kundu: With regard to 6 GHz plasma emission, I believe that the time structure of these microwave bursts is less than 10 µs. Does it mean that in an astrophysical object such as the solar flare plasma, one should be able to produce such fine time structure bursts intrinsically, except for the fact that other effects may modify such time structures?

Stenzel: The time scale for the current distruption and associated microwave bursts is roughly given by the ion transit time through the perturbed current channel, here $\tau \sim 5$ cm/$(5 \times 10^5$ cm/sec$) \sim 10$ µsec. If a solar flare of similar plasma parameters would exhibit a multitude of unstable current filaments of comparable scale size one may indeed expect the emission to be randomly modulated at the above mentioned time scale.

Birn: In magnetotail simulations the asymmetry of the configuration with gradients parallel to the current sheet and a magnetic field component perpendicular to it seems to have an important effect. Could you study such effects with your device?

Stenzel: Yes, such studies could be done. We could establish such asymmetries by inclining the current-carrying plates at an angle with respect to one another.

Dum: You pointed out the importance of the electrodynamics of the plasma and external circuit for Double Layer (DL) formation. I think this is a very significant point for our going beyond the usual electrostatic laminar solution of the one dimensional Vlasov equation that is offered as an explanation even for such highly dynamic processes as auroras. Nevertheless, particles are also important. What do you think are the particle boundary conditions essential to DL formation such as injection or reflection from electrodes, etc. In the very recent experiment of Guyot and Hollenstein (Phys. Fluids 1983) DL formation seems to depend on whether one electrode is heated or not. How do you trigger DL in a controlled manner, as you mentioned?

Stenzel: The anode, which is the only relevant boundary, absorbs all electrons; thus we have no control over the injected particle distributions as in Hollensteins work.

I mentioned that we now trigger current disruptions (not necessarily double layers) in a controlled manner. This is done by pulsing a thin slab of magnetic field (B_z) transverse to the current sheet (J_y) which causes a total current disruption. Large inductive voltages drop off across the slab, possibly forming again double layers.

Bratenahl: Did I understand that you are now looking for spontaneous development of double layers; that is, double layer development without artificial stimulation?

81

Stenzel: The work reported did describe spontaneous development of double layers without artificial stimulations. We are now working on controlled disruptions of the entire current sheet.

D. Smith: You mention that when a double layer forms, a 3-D potential results with radial ion acceleration. Could you explain in more detail how this occurs?

Stenzel: The potential structure is three-dimensional, since only the perturbed central part of the current sheet rises to a large positive potential over a finite axial length. Since the ions are unmagnetized, they are accelerated in both radial and axial directions. This leads to a large ion, hence density loss from the perturbed current channel. The pump-out of plasma ultimately causes the current loss.

Henriksen: Does the electron distribution have a characteristic shape in velocity space?

Stenzel: Yes, we have made extensive measurements of the electron distribution function and found asymmetric distributions even without current dusruptions. The current sheet contains a large number ($\sim 10\%$) of runaway electrons which are accelerated by the inductive electric field along the separator. These particles strongly influence the transport processes and provide a source of free energy for driving various microinstabilities.

82

LESSONS FROM LABORATORY EXPERIMENTS ON RECONNECTION

R. L. Stenzel, W. Gekelman and J. M. Urrutia

Department of Physics, University of California, Los Angeles, CA 90024, U.S.A.

ABSTRACT

Magnetic reconnection has been studied in a laboratory experiment designed to model the basic two-dimensional neutral sheet configuration. However, the focus has been put on the inner region of the neutral sheet where the ions are effectively unmagnetized and MHD concepts are violated. In this parameter regime driven reconnection is governed by the fast dynamics of electrons. In true neutral sheets ($B_z \simeq 0$) the current is carried by electrons. Thin current sheets ($\Delta z \gtrsim c/\omega_{pe}$) rapidly form multiple X and 0 points due to the onset of the collisionless electron tearing mode. Magnetic energy is transported along the separator at the speed of whistler waves rather than Alfvén waves. Due to space charge separation the reconnection electric field E_y is, in general, not constant along the separator but localized near boundaries, nonuniformities in density and magnetic fields which limit the current I_y. This leads to localized particle acceleration, formation of anisotropic velocity distributions and instabilities. Reconnection and energization can be spatially separated which shows the importance of investigating both the global current system as well as critical local plasma properties. Experiments of current sheet disruptions are performed which demonstrate the processes of magnetic energy storage, transport, conversion and dissipation. Double layers and shock waves can be produced by current disruptions. The laboratory experiments show new dynamic features of reconnection processes not considered in MHD models yet relevant to narrow current sheets or the center of thick sheets.

INTRODUCTION

Since its introduction the concept of magnetic field line reconnection has been formulated in terms of MHD theories /1-4/. This was based on the conception that all gradient scale lengths in space plasmas are large compared with the particle gyroradii and that the time scales for magnetic field configurations to change are slow compared to gyroperiods. However, in the vicinity of magnetic neutral points where first the ions become unmagnetized the basic MHD concepts such as frozen-in magnetic fields, Alfvén wave propagation, space charge neutrality are all violated. Thus, the central region of neutral sheets is governed by different physical processes than the outer global region. While some processes such as single particle orbits have been investigated /5/ a self-consistent treatment for the inner region of neutral sheets does not seem to exist. This region is also difficult to observe from satellites in space due to the short transit time and the variability of the plasma. On the other hand laboratory plasmas are highly suited to establish neutral sheets less than an ion Larmor orbit thick. High resolution three-dimensional measurements of magnetic fields, electric fields, plasma properties, particle distributions and waves can and have been performed under controlled repeatable conditions /6/. The laboratory experiments can extend the parameter regime for reconnection to electron-dominated thin current sheets which would be difficult to investigate in space. Such thin current sheets are also likely to exist in space plasmas, possibly embedded in larger scale structures as indicated by rapid intense magnetic fluctuations near null regions. Other cases for thin current sheets are auroral arcs /7/ and magnetic cavities created by barium cloud releases /8/.

We observe that thin current sheets are dominated by the dynamics of electrons. Magnetic field perturbations propagate at whistler wave speeds rather than Alfvénic speeds. Thin current sheets are found to be unstable to the fast electron tearing mode. Space charge electric fields produce electron Hall currents and a magnetic field component B_y along the separator. The resultant magnetic field configuration approximates that of flux ropes embedded in a neutral sheet, however, with scale lengths small compared to the ion gyroradius r_{ci} and inertial length c/ω_{pi}. An external magnetic field component B_y magnetizes the electrons throughout the current sheet and permits electron currents to flow in regions of normal magnetic fields B_z. While the contribution of the ions to the plasma
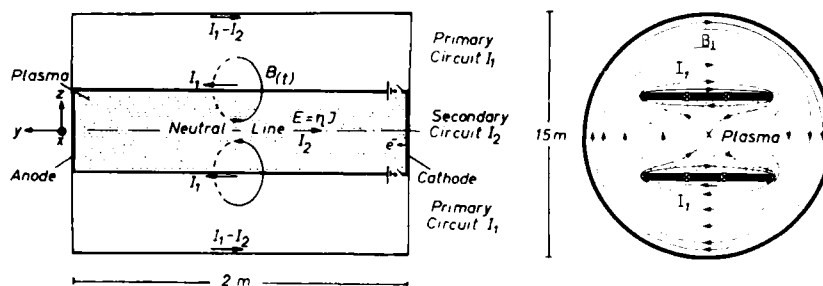
135

currents is negligible the ions are important with respect to setting up space charge fields to which they respond self-consistently. For quasi-stationary conditions, the ions stream across the separatrix as predicted by fluid theory but the acceleration mechanism differs from fluid models, i.e. the magnetic $\vec{J} \times \vec{B}$ force is exerted on the current-carrying electrons while the unmagnetized slow ions are accelerated by space-charge electric fields.

The properties of the global current system including boundary conditions have been investigated. It is found that the reconnection electric field E_y is, in general, not uniformly distributed along the separator but localized in regions of low conductivity, e.g. density depressions, normal magnetic fields, sheaths and double layers. Such localized electric fields give rise to localized particle accelerations. The injection of fast particles into the ambient plasma results in anisotropic distributions, velocity-space instabilities and plasma turbulence. The role of these instabilities is seen in the dissipation of the free energy in the distribution function, i.e conversion of streaming energy into heat. The dynamics of a current system has been studied by a controlled disruption of a current sheet. The processes of energy storage, release, transport, conversion to particle kinetic energy and dissipation into thermal energy have been followed. The understanding of dynamic reconnection processes requires knowledge of both global and local properties of the current system. These can be obtained in the laboratory but the extrapolation of the laboratory results to current systems in space remains a difficult task.

EXPERIMENTAL SETUP

As in the magnetosphere the reconnection process in the laboratory is driven by an external energy source, the solar wind in space, an external current system in the laboratory. Figure 1a shows schematically the experimental arrangement. A pulsed plasma column is generated by a dc discharge between a 1 m diameter cathode and an anode. The plasma of parameters listed in Figure 1b is uniform, quiescent, essentially collisionless, and highly

(a) EXPERIMENTAL ARRANGEMENT

(b) BASIC PARAMETERS

Plasma	$n = 10^{12}\,cm^{-3}$	Frequencies	$f_{pe} = 10\,GHz$, $f_{ce} = 30\,MHz$, $v_{ei} = 1\,MHz$
	$kT_e = 10\,eV$, $kT_i = 2\,eV$		$f_{pi} = 30\,MHz$, $f_{ci} = 400\,Hz$
	Argon , 10^{-4} Torr	Time scales	reconnection $t = 100\,\mu sec$
Fields	$B = 0-20\,G$, $E = 1\,V/cm$, $B = \vec{0}(t)$		disruption $t = 10\,\mu sec$
Scale lengths	$\lambda_d = 30\,\mu m$, $c/\omega_{pe} = 5\,mm$		Alfvén time $1/v_A = 15\,cm/6 \times 10^5 cm/sec$
	$r_{ce} = 1\,cm$, $r_{ci} = 60\,cm$, $l_{mfp} = 2\,m$		$= 25\,\mu sec$
	plasma dim $2\,m \times 1\,m \times 0.35\,m$		

Fig. 1.   (a) Schematic diagram of the experimental set-up in a side view (left hand) and cross-sectional view (right hand).   (b) Basic plasma parameters.

reproducible in pulses of duration $t_p \simeq 5$ msec repeated every $t_r \simeq 1.5$ sec. The plasma column is immersed in a uniform axial magnetic field $0 < B_{yo} < 100$ G. For the driven reconnection experiments a time-varying ($t_{rise} \simeq 100$ µsec) magnetic field ($0 < B_\perp \le 20$ G) is applied transverse to the plasma column. This field is produced by pulsing primary currents I_1 through two parallel-plate electrodes adjacent to but insulated from the plasma column. The two primary currents close via the cylindrical chamber wall. Due to the symmetry of the current system there is a magnetic neutral line along the axis of the device. Typical magnetic field lines in vacuum are shown in the cross-sectional view of the device (Figure 1a, right figure). Since the space between the plates is filled with a highly conducting plasma a secondary current I_2 is induced anti-parallel to the primary current. The plasma current is mainly carried by electrons, it flows preferentially along the neutral line (separator) and closes via the outer chamber wall. In a linear device the electrons are supplied by a source (cathode) and absorbed by a sink (anode). The plasma current is so large ($I_2 \simeq 1000A$) that the vacuum magnetic field topology of the curl-free X-point is fundamentally changed resulting in a neutral sheet, magnetic islands, or tearing

84

mode configurations. We emphasize the importance of the current closure which is usually
not discussed in two-dimensional reconnection models. For example, if in the present
experiment the electron supply is absent (e.g. in the afterglow) the plasma current drops
to the low value of the ion saturation current $[I_1/I_e \simeq (m_e\ T_1/m_1\ T_e)^{1/2} \simeq 10^{-3}]$ and the
reconnection proceeds almost as in vacuum, irrespective of the high conductivity of the
plasma.

Detailed plasma diagnostic tools are employed in conjunction with a high-speed digital data
processing system. Vector magnetic fields $\vec{B}(\vec{r},t)$ are obtained in situ with a movable probe
at up to 5000 spatial locations ($\Delta r \simeq 2$ cm) and 1000 temporal points ($\Delta t \simeq 100$ nsec). From
repeated measurements statistical averages are formed (mean, standard deviation, correla-
tions). Distribution functions are measured with a modified retarding potential analyzer
which filters particles through a passive microchannel plate and thereby obtains high
directional sensitivity ($\Delta\Omega/4\pi \simeq 10^{-3}$). The small detector (~3 mm radius) can be moved in
real space, rotated at each position through the two orthogonal spherical angles θ, ϕ so as
to obtain from the differential particle flux the three-dimensional distribution function
$f(v,\theta,\phi)$ or $f(v_x,v_y,v_z)$. Electron and ion phase space measurements $f(\vec{v},\vec{r},t)$ are time
resolved to within a few microseconds. Ensemble averages yield fluctuations in velocity
space. Measurements of such multi-dimensional functions produce large data flows ($N > 10^9$
numbers) which can only be handled by digital techniques. The analog traces are therefore
digitized with 100 MHz, 32 K, 8 bit A-D converters, evaluated on-line with an array
processor and a VAX 11/750 computer linked to a Cray computer for further analysis.
Besides particles and fields, plasma waves are investigated. Frequency spectra ($10^5 < f <$
10^{10} Hz) and wavevectors $\vec{k}$ are measured using two-point cross correlation techniques.

In order to facilitate comparison between the geometries of the laboratory and the
magnetotail we have chosen the same coordinate system where x is along the neutral sheet, z
is normal to the sheet, and y is along the neutral line or separator.

EXPERIMENTAL RESULTS: THE NEUTRAL SHEET

During the time of rising external flux ($0 < t \leq 100$ μsec) the magnetic field topology in
the x-z plane assumes the shape of a classical neutral sheet. Figure 2a shows a vector
field (B_x, B_z) vs. (x,z) which indicates the long ($L_x \simeq 40$ cm), thin ($L_z \simeq 5$ cm) region of
vanishing transverse fields embedded in the reverse-field geometry. Normal to the plane
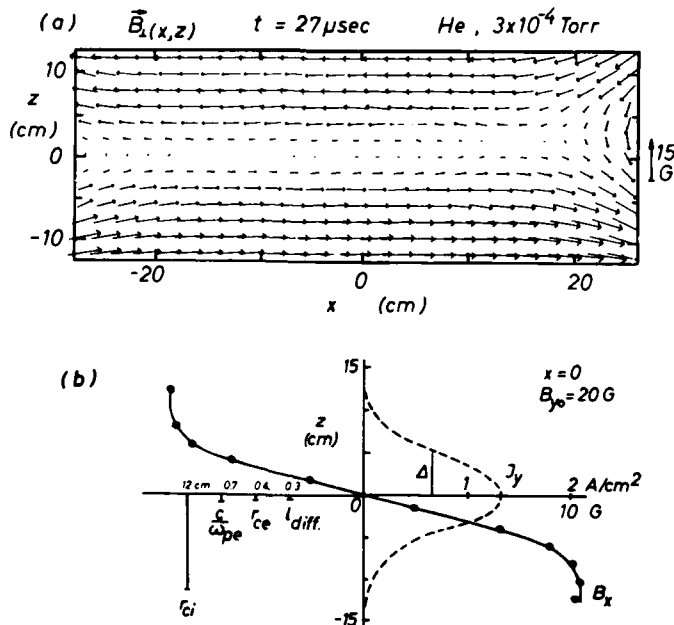

Fig. 2. (a) Magnetic field vector map (B_x, B_z) in the x-z plane (y = 137 cm
from cathode), showing the classical neutral sheet topology. The field
configuration is quasi stationary, i.e. unchanged as long as external flux is
supplied. ($B_{yo} \simeq 20$ G = const). (b) Magnetic field variation $B_x(z)$ across the
neutral sheet yields the current density profile $J_y(z) = (\partial B_x/\partial z)/\mu_0$. The
half width $\Delta \simeq 5$ cm is smaller than characteristic ion scale lengths ($c/\omega_{pi} \simeq$
60 cm, $r_{ci} \simeq 12$ cm), but larger than electron lengths ($c/\omega_{pe} \simeq 0.7$ cm, $r_{ce} \simeq$
0.4 cm). The current is carried by electrons.

85

there is a uniform field component $B_{yo} \simeq 20$ G. Figure 2b displays at x = 0 the B_x component vs. z and its derivative which yield the current density $J_y \simeq (\partial B_x/\partial z)/\mu_o$. The half width $\Delta \simeq 5$ cm of the current sheet is seen to be small compared to characteristic ion scale lengths ($c/\omega_{pi} \simeq 60$ cm, $r_{ci} \simeq 12$ cm in helium) but larger than the corresponding electron scale lengths ($c/\omega_{pe} \simeq 0.7$ cm, $r_{ce} \simeq 0.4$ cm) and the length of the classical diffusion region ($\ell_{diff} \simeq 0.3$ cm). Such narrow current sheets are typical when the current is dominated by electrons [$j_e/j_i \gtrsim (m_i/m_e)^{1/2}$] which is always the case near a true neutral sheet ($B_z = 0$). A finite B_y component enables electrons to flow in regions of finite B_z which broadens the electron current sheet ($\Delta > r_{ce}$). An electron current sheet of width $\Delta_e \simeq c/\omega_{pe}$ carries as much current as an ion current sheet of width $\Delta_i \simeq c/\omega_{pi}$, provided the currents are driven by the same electric fields E_y. Thus, the role of electrons and the inner structure of the neutral sheet are very important to the reconnection problem.

Long thin neutral sheets are subject to tearing instabilities /9/. We have established an experimental configuration which is particularly suited to study current sheet instabilities since it establishes known boundary and initial conditions. As shown in Figure 3 a fine wire grid (transparency > 80%) with a long ($L_x \simeq 75$ cm), narrow ($1 < L_z < 4$ cm) slot is inserted in the plasma in the midplane (y $\simeq 100$ cm). At a desired time (t' = 0) the grid is biased to a large negative potential ($-V_g \simeq 200$ V $\gg kT_e$) which constricts the current sheet to the width of the slot. The subsequent space-time evolution of the magnetic field $\vec{B}_{(x,y,z,t)}$ is measured from which the current density $\vec{J}_{(x,y,z,t)} = \nabla \times \vec{B}/\mu_o$ is calculated.
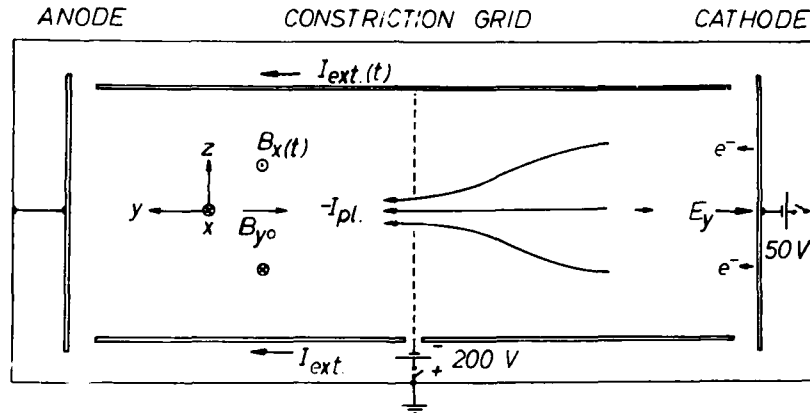

Fig. 3. Experimental arrangement for studying the stability of thin current sheets. The electron current is forced to flow through a narrow ($\Delta z \simeq 1$ cm) long ($\Delta x \simeq 75$ cm) slot in a grid at y $\simeq 100$ cm pulsed to a large negative potential ($e|V_g| \gg kT_e$). Tearing mode growth in the x-z plane and propagation effects in the y-direction are observed.

Figure 4 displays the magnetic topology $\vec{B}_{(x,z)}$ which has developed multiple X and 0-points within $\Delta t \simeq 8$ μsec after constricting the current to flow through a 1 cm x 75 cm slot. The time and spatial scales indicate that the spontaneous tearing process is due to the collisionless electron tearing mode /10/ whose growth rate is predicted to be

$$\gamma = \frac{k_x v_e}{\sqrt{\pi}} \frac{B_{ox}}{B_{oy}} \left(\frac{\lambda_e}{\ell}\right)^2 (1 - k_x^2 \ell^2) \tag{1}$$

where k_x is the wavenumber of the modes ($k_x \simeq 2\pi/20$ cm^{-1}), v_e the electron thermal speed ($v_e \simeq 1.5 \times 10^8$ cm/sec), B_{ox} is the asymptotic B_x component away from the current layer ($B_{ox} \simeq 8G$), B_{oy} is the field component along the separator ($B_{oy} \simeq 20$ G), λ_e is the electron inertial length ($\lambda_e = c/\omega_{pe} \simeq 0.7$ cm) and ℓ is the halfwidth of the current layer ($\ell \simeq 2$ cm). The predicted growth time for the experimental conditions is $\gamma^{-1} \simeq 1.3$ μsec, consistent with the observed fast island growth.

Figure 5 demonstrates the rapid axial propagation of the current system. Contours of constant current density J_y are displayed in the y-z plane (x $\simeq 0$) at different times Δt after the constriction of the current channel by a 4 cm x 75 cm slot located at $\Delta y = 0$. One constant amplitude contour enhanced as a heavy solid contour represents approximately the front of the constricted current sheet. It propagates along $B_{yo} \simeq 20$ G at a speed $v_y \lesssim 10^7$ cm/sec which is much faster than the Alfvén speed ($v_A \simeq 7 \times 10^5$ cm/sec) and more closely given by the group velocity of a whistler wave packet with frequency determined by the switching time ($\Delta t \simeq 2$ μsec $\simeq f^{-1}$),
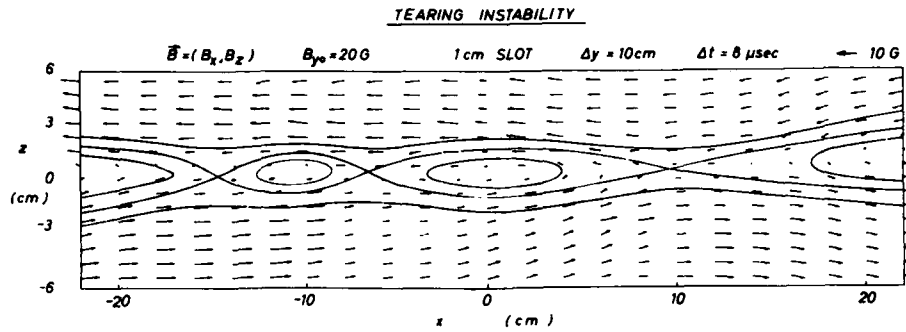
86

TEARING INSTABILITY

Fig. 4. Magnetic field topology $\vec{B}_{(x,z)}$ for a thin current sheet ($\Delta \simeq 2$ cm $\simeq$ 3 c/ω_{pe}) exhibiting multiple X and O points as a result of electron tearing modes. The measurement is taken at $\Delta y = 10$ cm from the center grid and $\Delta t = 8$ μsec after the injection of the narrow current sheet.
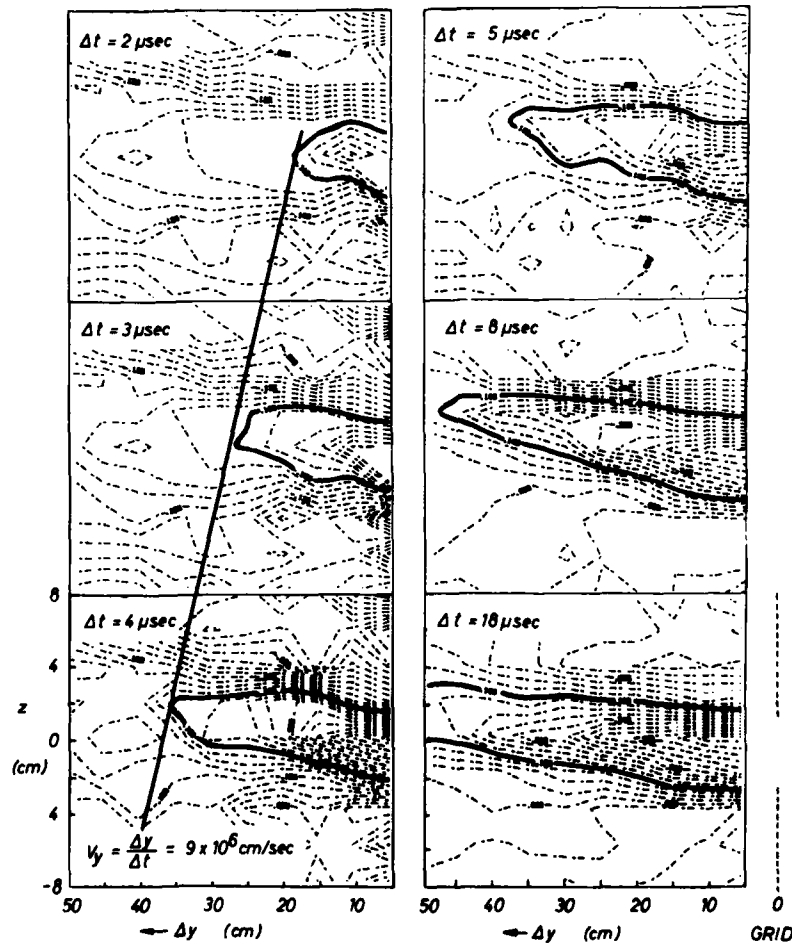
PROPAGATION OF CURRENTS

$$J_y(y,z) = const.$$

Fig. 5. Propagation of a current sheet along the separator. At $\Delta t = 0$ a narrow current sheet is injected at the slotted ($\Delta z = 4$ cm) grid located at $\Delta y = 0$. The thick curve in the contour plot of constant current density $J_{y(x=0,y,z)}$ roughly indicates the front of the current sheet which propagates at initial speeds $v_y \gg v_{Alfvén}$, $v_y \lesssim v_{whistler}$.

87

$$v_{g_{||}} = \frac{\partial \omega}{\partial k} \simeq 2 \quad \omega\,\omega_{ce} \quad \frac{c}{\omega_{pe}} \simeq 3 \times 10^7 \text{ cm/sec} \qquad (2)$$

Thus, the common assumption that currents or magnetic field perturbations propagate at the
Alfvén speed does not hold near magnetic neutral regions where the ions are effectively
unmagnetized. There, the electrons remain magnetized, carry currents and transport
magnetic energy along the separator with their characteristic modes, i.e. whistlers. This
result is very important when we consider the disruption of a current sheet and the release
of stored magnetic energy.

THE RECONNECTION ELECTRIC FIELD AND PARTICLE ENERGIZATION

Two-dimensional reconnection models assume that there are no variations along the neutral
sheet ($\partial/\partial y = 0$). Such models cannot address the problems of current closure and the
realistic situation that global current systems are, in general, not uniform along the
entire current path. This has important consequences on the reconnection electric field E_y
which in 2-D models is assumed constant along y and is given by the flux transfer rate $E_y =
\partial A_y/\partial t$. In general 3-D current systems, Faraday's law only determines the line integral of
the reconnection electric field to be given by the magnetic flux change, $\oint \vec{E}\cdot d\vec{l} = -\partial\phi/\partial t$,
and it depends entirely on the circuit properties how the electric field is distributed
along the current path. An important result of the laboratory experiments is the finding
that the reconnection electric field E_y can be highly localized. This fact is significant
for the understanding of particle acceleration during reconnection.

Figure 6 shows in schematic form our global current system and gives three examples of
localized electric fields.   Figure 6a indicates that during quasi-stationary reconnection
experiments (I_2 = const.) the reconnection voltage (analogous to cross-tail potential
difference) is observed to drop off mainly (~80%) at the plasma boundary near the cathode.
The bulk of the highly conducting plasma shields itself from the applied inductive electric
field by setting up an opposing space charge electric field, hence behaves similar to the
highly conducting external current closure. It is the cathode sheath which, in this
current system, limits the total current and has the highest effective "resistance" V/I.
The consequence of this localization of E_y is that the particle energization occurs mainly
at the plasma boundary rather than in the bulk of the plasma. Reconnection and energiza-
tion are spatially separated, a concept never considered in 2D theories. It is not
inconceivable that similar situations also arise in magnetospheric current systems; for
example, flux changes due to reconnection in the magnetotail may set up localized electric
fields at the boundary layer and in auroral regions such that the energy dissipation is not
in the tail itself but in other parts of the extended magnetospheric current system.

A second situation where localized electric fields have been observed is shown in Figure
6b. At large current densities spontaneous fast current disruptions have been observed
/11/. When the electron drift velocity approaches the thermal velocity a spontaneous
density depression leads to a current decrease, a localized electric field which in turn
enhances the density depression, and the process runs away into a major current disruption.
The inductive voltage associated with the rapid current/flux change ($V = LdI/dt = d\phi/dt$)
drops off at the location of the current disruption forming a transient potential double
layer /12/. Again, electrons and ions are locally accelerated gaining kinetic energy on
expense of released magnetic energy stored in other parts of the current system. The
injection of particle streams into the ambient plasma creates a variety of instabilities
which eventually convert the directed kinetic energy into thermal energy.

A third example of localized fields and particle accelerations is depicted in Figure 6c.
In this experiment which will be described in more detail below, the electron current sheet
is disrupted by a pulsed slab of normal magnetic field B_z (>> B_{yo} ≈ 6G) located in the
center of the device. The inductive voltage generated by the loss of magnetic flux due to
rapid reconnection drops off across the slab of normal B_z, the magnetic "switch". In the
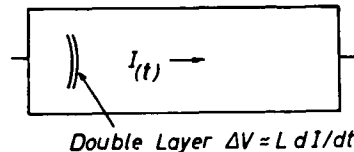same region the particles are energized.

Finally, an example of the energized particles is shown in Figure 7. The electron
distribution is measured with a directional velocity analyzer /13/ in the neutral sheet
during quasi-stationary reconnection. Figure 7a shows basic current-voltage traces of the
analyzer which represent the integrated electron flux vs. energy. One can clearly
distinguish a population of low energy bulk electrons and a group of energetic electrons
streaming away from the cathode. The energy of the tail electrons exceeds the dc cathode
potential (~40 V) by approximately the reconnection voltage ($d\phi/dt$ ≈ 100 V). Since these
fast electrons are observed already near the cathode end of the device they have been
accelerated by a localized electric field. With increasing distance from the cathode the
tails are scattered and the bulk temperature increases although kT_e ≈ 10 eV << $d\phi/dt$.
Figure 7b indicates the electron distribution function in the middle of the device,
displayed as a contour of constant value $f(\vec{v}) = 10^{-16}$ cm^{-6} sec^3 in three-dimensional
velocity space $\vec{v} = (v_x, v_y, v_z)$. The energized electrons injected into the neutral sheet
topology are scattered in velocity space by $\vec{E} + \vec{v} \times \vec{B}$ forces and form complicated tail

88

LOCALIZED ELECTRIC FIELDS

(a) Quasi-stationary Reconnection

Plasma R ≈ 0

Sheath Potential

$\Delta V = -d\emptyset/dt = \oint_C E\, dl$

$\otimes\ B_{(t)}\ \otimes\ \ \otimes$
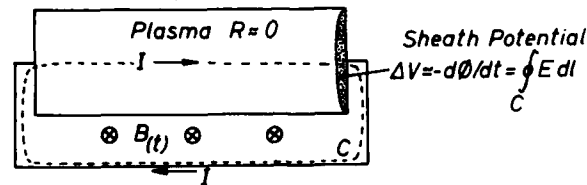
(b) Current Disruptions ($v_d \rightarrow v_e$, $n_i \rightarrow 0$)

$I_{(t)} \rightarrow$

Double Layer $\Delta V = L\, dI/dt$

(c) Localized Magnetic Fields $B_{z(y,t)}$

$I_{(t)} \rightarrow$:B: $I \rightarrow$

$\Delta V = -d\emptyset/dt = L\, dI/dt$
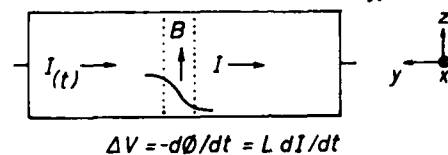
Fig. 6. Examples of localized reconnection electric fields E_y which can only be explained by considering the global current system rather than a local section containing a two-dimensional current sheet. (a) In quasi-stationary reconnection ($0 < t \leq 100\mu sec$) the induced voltage associated with the flux transfer across the separatrix mainly drops off at the cathode sheath. Local particle acceleration by inertial effects permits rapid reconnection in the otherwise highly conducting current system. (b) Spontaneous fast current disruptions ($\Delta t \simeq 10\mu sec$) are observed at large current densities which lead to a local density depletion and the formation of a double layer. At the double layer the excess magnetic energy is converted into particle kinetic energy. (c) A controlled rapid current sheet disruption ($\Delta t \sim 10\mu sec$) is produced by a pulsed normal magnetic field $B_{z(t)}$ which prevents the free electron motion along the separator. The inductive voltage drops off across the region of B_z where the excess magnetic energy is dissipated.

distributions /14/. The free energy in these distributions drives various instabilities, e.g. electron plasma waves and whistler waves, some of which have been studied in detail /15/.

The laboratory experiments have shown the importance of investigating both the global current system and local plasma properties in order to understand the dynamics and energetics of reconnection. The formation of localized electric fields permits rapid reconnection to occur in highly conducting plasmas by the process of inertial reconnection. During the finite transit time through the electric field structure the particles are energized without undergoing collisions. The field structure provides dissipation of magnetic energy in a current system without significant resistivity. The energization of particles can be localized, sporadic, and usually leads to anisotropic distribution functions. Such features have also been observed in the magnetotail with high resolution electron detectors /16/.

DISRUPTION OF A CURRENT SHEET

Reconnection attempts to explain the rapid conversion of magnetic energy into particle kinetic energy which is observed to occur in solar flares and magnetic substorms. Although in the laboratory one cannot model the complicated global current systems encountered in space one can establish simpler but related configurations and investigate the basic physics of magnetic energy storage, release, transport, conversion and dissipation. Such an experiment will be described here.

Figure 8 summarizes the events observed when an initially quasi-stationary current sheet is suddenly disrupted in order to release the excess magnetic energy of the system. The

89

R. L. Stenzel, W. Gekelman and J. M. Urrutia

(a) INTEGRATED ELECTRON FLUX

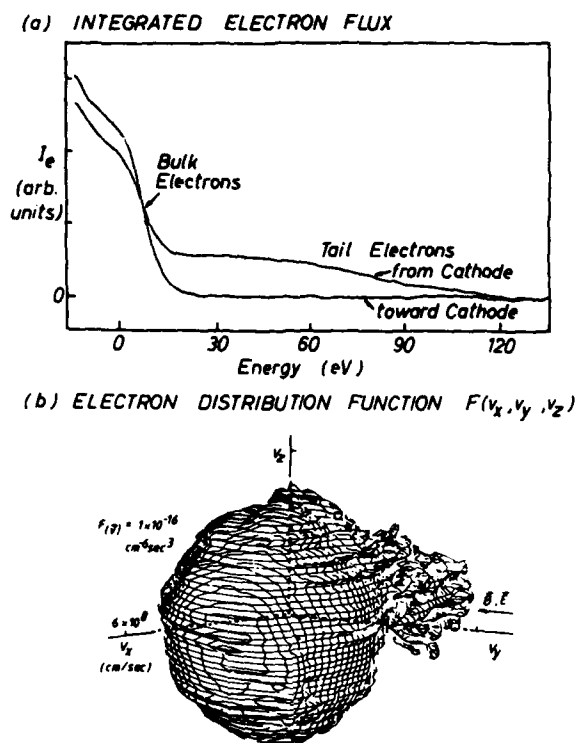(b) ELECTRON DISTRIBUTION FUNCTION $F(v_x, v_y, v_z)$

Fig. 7. Anisotropic electron distributions produced by localized electric
fields. (a) Electron flux vs. energy observed with a directional particle
analyzer pointed in both directions along the separator. From the localized
field E_y near the cathode a flux of energetic electrons is ejected which
acquired most of the reconnection energy ($ed\phi/dt \approx 100$ eV). (b) Three-
dimensional electron distribution function displayed as surface of constant
value $f(v_x, v_y, v_z) = 10^{-16}$ cm^{-6} sec^3, showing the distribution of tail electrons
after propagation along the neutral sheet. The free energy in the distribution
excites Langmuir and whistler turbulence.

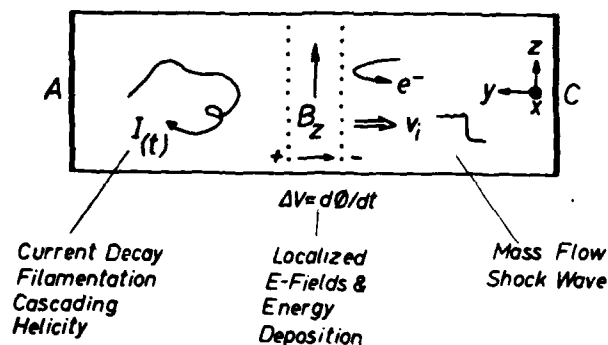CURRENT DISRUPTION
DUE TO LOCALIZED B_z FIELD

Fig. 8. Schematic diagram describing the results of disrupting a current sheet
J_y with a rapidly pulsed solenoidal magnetic field B_z.

disruption mechanism described in Figure 6c establishes reproducible initial and boundary
conditions so that one can follow the complicated events in space and time. In space
plasmas analogous disruptions may arise from large amplitude magnetic waves or fast tearing
modes. We find that after applying the switch magnetic field B_z the excess magnetic energy
of the neutral sheet disappears on a time scale of whistler wave propagation along the
separator (~ 100 cm/10^7 cm sec^{-1} $\approx$ 10 μsec). The initially laminar current sheet cascades

into small scale filamentary current loops which generate magnetic helicity /17/. A
potential difference corresponding to the magnetic flux change $d\phi/dt$ drops off across the
magnetic switch. The global decrease of magnetic energy $Id\phi/dt$ causes a local increase in
particle energy, i.e. ions are accelerated by E_y across B_z since $r_{ci} > B/\nabla B$, electrons are
heated by cross-field instabilities, and additional plasma is created by ionization of
neutrals at high electron temperatures. The rapid local energization causes the plasma to
expand primarily in the direction of the ion flow. The front of the mass flow steepens
into a large-amplitude electrostatic shock wave. It slowly dissipates its energy by
interaction with the background ions.

The events summarized in Figure 8 will now be supported by direct observations. Figure 9a
displays the time dependence of the plasma current I_2 as measured at the anode. After it
has built up to its quasi-stationary value the local normal magnetic field B_z is switched
on which completely disrupts the external current flow. Figure 9b shows the time
dependence of the dominant magnetic field component B_x in the plasma and, for comparison,
in vacuum. The formation of the neutral sheet stores excess magnetic energy which upon
current disruption is released within $\Delta t < 10$ μsec. This rapid time scale cannot be ex-
plained by Alfvén wave propagation ($\Delta t \sim 100$ μsec) or resistive dissipation ($\Delta t > 1$ msec),
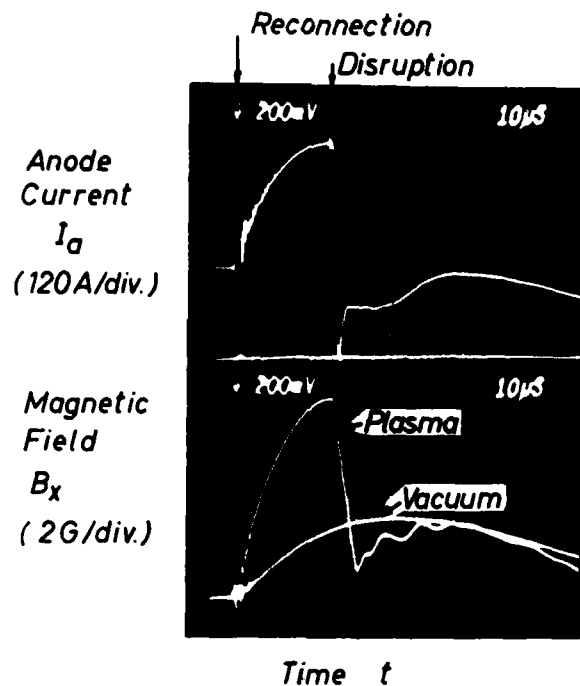but by whistler wave propagation of rapid magnetic perturbations such as shown in Figure 5.

Fig. 9. Time scale of current disruption and magnetic energy loss. (a) Plasma
current at the anode which, after building up to its peak value is disrupted at
$t \simeq 25$ μsec by the magnetic switch. (b) Magnetic field $B_{x(t)}$ in the neutral
sheet region (with plasma) and in vacuum. Prior to the disruption excess
magnetic energy is stored by the plasma current. After the disruption it is
released within $\Delta t \simeq 10$ μsec, a time scale too short for convection by Alfvén
waves or resistive diffusion but consistent with whistler wave propagation
(Figure 5).

Figure 10 shows the dynamics of the current system during the disruption. From repeated
measurements of the magnetic field $\vec{B}_{(\vec{r},t)}$ at 5000 spatial locations ($\Delta r \simeq 2$ cm) and 1024
time increments ($\Delta t = 50$ nsec) the current density $\vec{J}_{(\vec{r},t)} = \nabla \times \vec{B}/\mu_0$ is calculated, field
lines are fitted through this vector field, and displayed in the plasma volume between
switch and anode at different times of the disruption process. Prior to the disruption
($t = -0.6$ μsec) the current flows as a laminar sheet in the x-y plane ($z \simeq 0$) from anode to
cathode. As the electron inflow at the left-hand x-z plane is inhibited by the growing B_z
component the current begins to circulate within the plasma volume forming temporally
repeatable but spatially random patterns of small-scale current loops and filaments. The
process of cascading from large to small-scale structures coincides with the decrease in
the strength of the current or magnetic energy, however, a causality between the two
processes is not easy to infer. Similar cascading processes have also been observed in
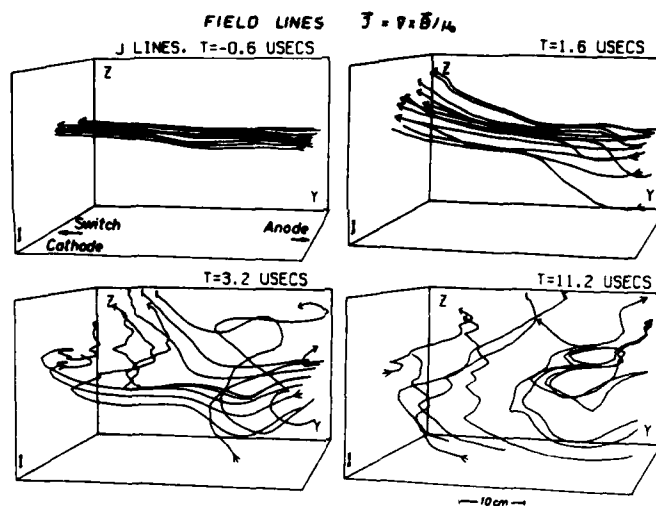other laboratory devices and compared with solar flare phenomena /18/.

FIELD LINES $\vec{J} = \nabla \times \vec{B}/\mu_0$

Fig. 10. Field lines for the current density vector $\vec{J}_{(x,y,z,t)}$ at different
times of the current sheet disruption. The initially ($t = -0.6$ μsec) laminar
current sheet cascades during the disruption into small scale current loops and
filaments. Simultaneously, the magnetic energy is lost. Due to the controlled
disruption the spatially random current pattern is highly repeatable from pulse
to pulse.

From the knowledge of the current density $\vec{J}$ the vector potential $\vec{A}_{(\vec{r},t)} = \frac{\mu_0}{4\pi} \int \vec{J}_{(\vec{r},t)}/$
$|\vec{r}-\vec{r}|\,dV'$ has been calculated. Since $\vec{B}_{(\vec{r},t)}$ is also known, the magnetic helicity $K_{(t)} = \int \vec{A}\cdot\vec{B}\,dV$ of the plasma current system can be found. Helicity is a measure for the linkage
of magnetic flux of current systems and, in ideal MHD, is a conserved quantity like
magnetic energy /19/. Figure 11 shows the observed change of helicity which indicates flux
linkage to occur during the current sheet decay. Helicity and energy decay on the fast
time scale of electron whistlers.

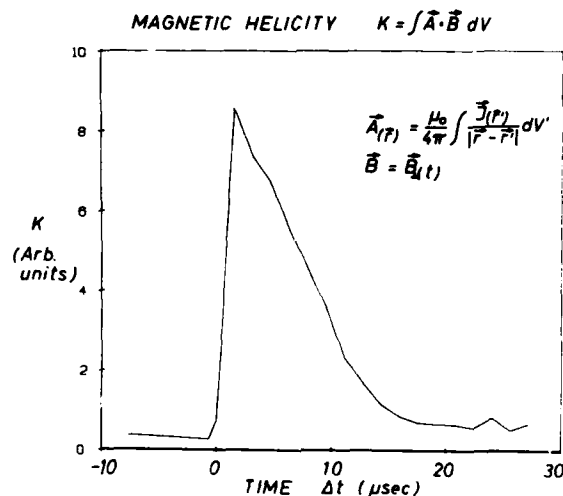MAGNETIC HELICITY $K = \int \vec{A}\cdot\vec{B}\,dV$

Fig. 11. Temporal variation of the magnetic helicity of the plasma current
system. The current sheet disruption changes helicity and energy on a time
scale of whistler wave propagation through the device.

In order to account for the loss of magnetic energy the plasma parameters have been
measured throughout the plasma volume. The only region where significant energization
occurs is around the magnetic switch. Figure 12 shows an axial plot of density,
temperature and plasma potential during the early disruption ($\Delta t \simeq 2$ μsec). A potential
$\Delta\phi_p \simeq 30$ V drops off across the region of normal B_z which locally raises the electron
temperature to $kT_e \simeq 10$ eV, and increases the density by ionization. With increasing time
the density peak grows ($\delta n/n \geq 100\%$) and propagates into the low potential region due to
ion acceleration.

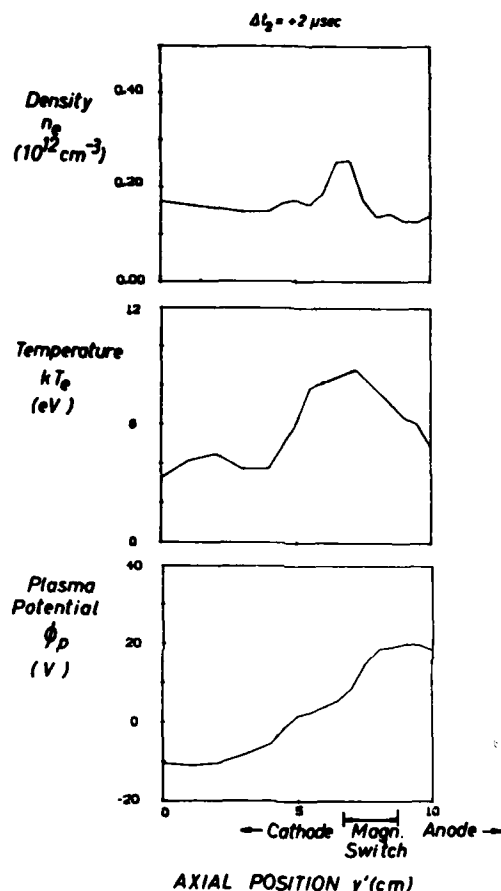## Plasma Parameters
During Current Disruptions.

$\Delta t_2 = +2 \mu sec$

Density
n_e
$(10^{12} cm^{-3})$

Temperature
kT_e
(eV)

Plasma
Potential
ϕ_p
(V)

← Cathode Magn. Anode →
Switch

AXIAL POSITION y'(cm)

Fig. 12. Plasma properties n_e, T_e, ϕ_p vs. y during the early phase of the
current disruption. A potential difference $\Delta\phi_p \simeq$ 30V drops off across the
region of normal magnetic field B_z which leads to ion acceleration, electron
heating and a density increase by ionization, all on expense of the magnetic
energy of the disrupted current system.

The ejection of energized plasma is shown in Figure 13. It displays the ion density vs.
time observed at increasing distances Δy from the magnetic switch toward the cathode. The
front of the ejected plasma is observed to steepen into an electrostatic shock wave of
width $\delta_y \simeq 0.6$ mm $\simeq 15$ λ_D propagating with sonic Mach number M = $v_y/c_s \simeq 1.5$ along B_{yo}.
With increasing distance the shock amplitude decays, i.e. wave energy is transferred to the
background plasma. Such dissipation processes involve the acceleration and reflection of
background ions. Measurements of the ion distribution function have shown the tail
formation /20/. At the foot of the shock enhanced density fluctuations are observed
associated with reflected ions exciting beam-plasma instabilities.

SUMMARY

Magnetic reconnection has been studied in a laboratory plasma with electron dominated
current sheets. Reconnection is viewed as a property of an entire current system rather
than a local process. Investigation of the third dimension, i.e. the direction along the
current flow, has shown that reconnection (flux transfer) and dissipation (acceleration by
localized electric fields) can be spatially separated. The energy is transported along the
current system by characteristic electromagnetic modes, which are whistlers for electron
dominated current sheets. The central region of neutral sheets ($\Delta z \lesssim r_{ci}$) is controlled by
the dynamics of electrons. Examples of dynamic current systems have been presented
(current constrictions, partial and total disruptions) which differ in the details of the
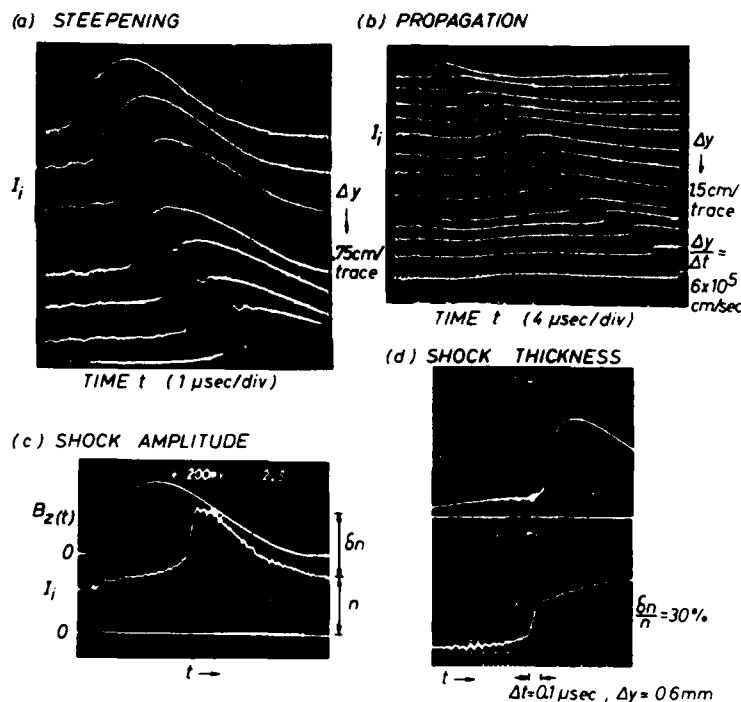events but have in common the rapid conversion of magnetic energy into particle kinetic

93

Fig. 13. The local energization of the plasma at the magnetic switch leads to a mass outflow which steepens into an electrostatic shock wave propagating along $B_{yo} \simeq 6$ G toward the cathode. (a) Ion flux vs. time at different positions Δy showing shock formation by nonlinear steepening. (b) Shock wave propagation at sonic Mach number $M = v_s/c_s \simeq 1.5$ ($v_s \simeq 5.5 \times 10^5$ cm/sec, $kT_e \simeq 6$ eV). (c) Shock wave amplitude $\delta n/n \simeq 100\%$ near region of formation. For comparison the waveform of the switch B_z is shown. (d) Shock thickness $\Delta y = v_s \Delta t \simeq 0.6$ mm $\simeq 15\lambda_D$ of a fully steepened shock wave observed on two time scales (1 µsec/div top, 0.2 µsec/div bottom). Note oscillations at the shock foot due to reflected ions forming beam-plasma instabilities.

energy in highly conducting plasmas. Since current systems in space also differ greatly there may be many unexpected forms and signatures of reconnection in addition to the standard fluid motion across the separatrix. The laboratory experiments suggest to look at processes along the separator, i.e. electric fields at nonuniformities, the role of electrons in transporting energy and momentum, the role of a B_y component, the current closure, and correlations between magnetic flux variations and particle energization at different parts of the current system. Simultaneous observations from several spacecraft would seem a prerequisite for investigating three-dimensional dynamic current system.

ACKNOWLEDGMENTS

REFERENCES

1. J. W. Dungey, Conditions for the occurrence of electrical discharges in astrophysical systems, Phil. Mag., Ser. 7, 44, 725-738 (1953).

2. P. A. Sweet, The neutral point theory of solar flares, in: Electromagnetic Phenomena in Cosmical Physics, ed. B. Lehnert, Cambridge University Press, London, 1958, pp. 128-134.

3. H. E. Petschek, Magnetic field annihilation, AAS-NASA Symposium on the Physics of Solar Flares, NASA Spec. Publ. SP-50, 1964, pp. 425-439.

4. V. M. Vasyliunas, Theoretical models of magnetic field line merging, 1., Rev. Geophys. Space Phys. 13, 303 (1975).

5. T. W. Speiser, Particle trajectories in model current sheets, 2., <u>J. Geophys. Res.</u> 72, 3919 (1967).

6. R. L. Stenzel, W. Gekelman and J. M. Urrutia, Laboratory experiment on magnetic reconnection and turbulence, in: <u>Magnetic Reconnection and Turbulence</u>, ed. M. A. DuBois, D. Grésillon and M. N. Bussac, Editions de Physique, Orsay, France, 1985, pp. 63-77.

7. J. C. Cerisier, C. Machard, J. J. Berthelier, and C. Beghin, Electrostatic and magnetic turbulence in auroral regions, in: <u>Magnetic Reconnection and Turbulence</u>, ed. M. A. DuBois, D. Grésillon and M. N. Bussac, Editions de Physique, Orsay, France, 1985, pp. 179-192.

8. G. Haerendel, Plasma and neutral gas injections -- an overview, <u>Symposium on Active Experiments</u>, XXVI, Abstract 1.1.1, (1986).

9. G. Laval, R. Pellat, and M. Vuillemin, Instabilités electromagnétiques des plasmas sans collisions, in: <u>Proceedings of the Conference on Plasma Physics and Controlled Nuclear Fusion</u>, International Atomic Energy Agency, Vienna, Austria, 1966, Vol. 2, p. 259.

10. A. A. Galeev and L. M. Zeleny, Magnetic reconnection in a space plasma, in: <u>Theoretical and Computational Plasma Physics</u>, International Atomic Energy Agency, Vienna, Austria, 1978, p. 93.

11. R. L. Stenzel, W. Gekelman, and N. Wild, Magnetic field line reconnection experiments, 5. Current disruptions and double layers, <u>J. Geophys. Res.</u> 88, 4793 (1983).

12. P. Carlquist, On the formation of double layers in plasmas, <u>Cosmic Electrodynamics</u> 3, 377-388, 1972.

13. R. L. Stenzel, W. Gekelman, N. Wild, J. M. Urrutia, and D. Whelan, Directional velocity analyzer for measuring electron distribution functions in plasmas, <u>Rev. Sci. Instrum.</u> 54, 1302-1310 (1983).

14. W. Gekelman and R. L. Stenzel, Measurement and instability analysis of three-dimensional anisotropic electron distribution functions, <u>Phys. Rev. Lett.</u> 54, 2414 (1985).

15. W. Gekelman and R. L. Stenzel, Magnetic field line reconnection experiments, 6. Magnetic turbulence, <u>J. Geophys. Res.</u> 89, 2715 (1984).

16. J. W. Bieber, E. C. Stone, E. W. Hones Jr., D. N. Baker, S. J. Bame and R. P. Lepping, Microstructure of magnetic reconnection in Earth's magnetotail, <u>J. Geophys. Res.</u> 89, 6705-6716 (1984).

17. W. Gekelman, J. M. Urrutia and R. L. Stenzel, Measurement of magnetic helicity during the disruption of a neutral current sheet, University of California, Plasma Physics Report PPG 940, 1986.

18. S. A. Colgate, Solar flares: An extremum of reconnection, in: <u>Magnetic Reconnection in Space and Laboratory Plasmas</u>, ed. E. W. Hones, Geophysical Monograph 30, AGU, Washington, D. C., 1984, pp. 372-374.

19. J. B. Taylor, Relaxation of toroidal plasma and generation of reverse magnetic fields, <u>Phys. Rev. Lett.</u> 33, 1139 (1974).

20. R. L. Stenzel, Ion acceleration processes in laboratory plasmas, in: <u>Ion Acceleration in the Magnetosphere and Ionosphere</u>, ed. T. Chang, Geophys. Monograph 38, American Geophysical Union, Washington, D. C., 1985, pp. 211-223.

ANOMALOUS CURRENTS TO AN ELECTRODE IN A MAGNETOPLASMA

J. M. Urrutia and R. L. Stenzel

Anomalous Currents to an Electrode in a Magnetoplasma

J. M. Urrutia and R. L. Stenzel

Department of Physics, University of California, Los Angeles, California 90024
(Received 31 March 1986)

An electrode pulsed to a large positive potential ($V \gg kT_e/e$) in a collisionless magnetoplasma is observed to draw currents far in excess ($10\times$) of the field-aligned electron saturation current prescribed by probe theory. The large currents are inferred to be due to anomalous cross-field transport caused by current-driven instabilities. Electric fields due to space-charge separation and anomalous conductivity lead in time to ion expulsion from the current channel and hence to density depletion and current collapse.

The current to an electrode biased above the plasma potential in a collisionless plasma is a long-standing problem of fundamental interest in plasma diagnostics[1-3] and current systems in space.[4] Earlier reports[5] have derived the plasma parameters from probe characteristics but have not considered the perturbing effects of saturation currents on the plasma. In this Letter we report measurements of the spatial and temporal evolution of the electron saturation current system, $\mathbf{J}(\mathbf{r},t)$, within the plasma as well as detailed diagnostics of electric field, density, and temperature. From the observations we conclude that electrons drawn by a highly biased ($V \gg kT_e/e$), pulsed probe raise the plasma potential in the flux tube roughly subtended by the electrode giving rise to electron Hall currents, expulsion of the unmagnetized ions from the flux tube, and anomalous radial electron currents. The enhanced parallel current near the probe creates an anomalously low parallel conductivity $\sigma(J)_\parallel^*$ which results in resistive electric fields, $E_\parallel = J_\parallel/\sigma(J)_\parallel^*$, far outside of the sheath region. Ions are accelerated away from the probe and electrons toward it resulting in a net density depletion, $n_e = n_i \rightarrow 0$, and hence the probe current collapses. Recovery of the current-driven instability causes plasma to flow back to the perturbed region and the process repeats periodically creating pulsating currents in steady state. The large transient current pulses penetrate into the plasma along $\mathbf{B}_0$ at near electron thermal speeds, but since they exist only over durations of ion transit times across the current channel the penetration along $\mathbf{B}_0$ is limited to distances

$$L = \frac{v_{d,e}}{v_{d,i}} r_{ft} \approx \left(\frac{kT_e m_i}{4\pi e \Delta\phi m_e} \right)^{1/2} r_{ft},$$

where $\Delta\phi$ is the radial potential drop in the channel and r_{ft} the flux tube radius. Our plasma is much larger than these scales; hence the results are not boundary dependent and can be scaled to relevant applications.[4]

The experiments are conducted in the quiescent afterglow ($t = 120$ μsec) of the pulsed ($t_{rep} = 2$ sec, $t_{on} = 4$ msec) plasma ($n_e \approx 2\times10^{11}$ cm^{-3}, $T_e \approx 5T_i$

≈ 1.5 eV, $B_0 \approx 30$ G, $p_n \approx 4\times10^{-4}$ Torr, Ar) schematically shown in Fig. 1(a). The electrode is a tantalum disc of 0.8-cm radius (r_D) insulated on one side. It is biased to $V = 80$ V ($\gg kT_e/e$) via a transistor switch with respect to the grid anode and chamber walls. The magnetic field, $\mathbf{B}(\mathbf{r},t)$, induced by the current is measured with a probe consisting of three electrostatically shielded, small (1-cm diam), orthogonal magnetic loops. The probe tip is capable of scanning a suitably large volume ($0 < r < 8$ cm, $0 < z < 55$ cm) about the electrode. The current-density vector field, $\mathbf{J}(\mathbf{r},t)$, is calculated via $\mathbf{J} = \nabla \times \mathbf{B}/\mu_0$. The local plasma parameters (n_e, kT_e, ϕ_{pl}) are obtained with a small (1×1.5-mm^2) Langmuir probe. The probe tip can also scan a volume about the electrode. The probe bias is changed in successive shots and the probe current-voltage characteristic as a function of time is reconstructed at each spatial point. The acquisition and handling of the necessary large data set is done by computer.[6]
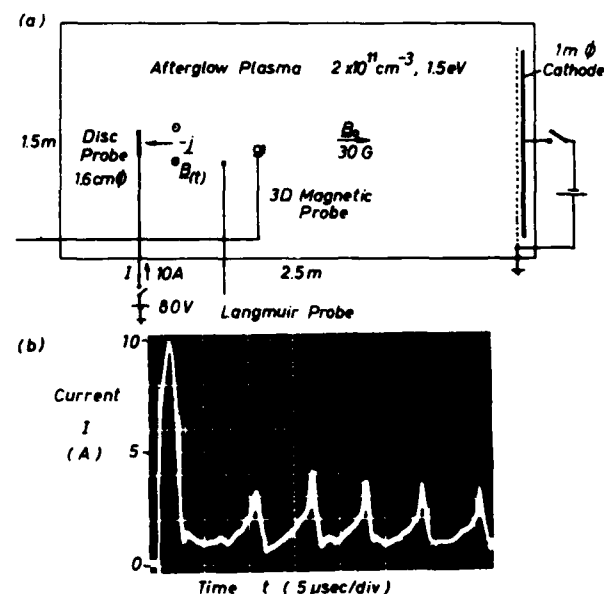

FIG. 1. (a) Experimental device. (b) Electrode current I vs time t at $V = 80$ V.

715

99

The normally floating electrode is pulsed (rise time $\simeq$ 200 nsec, $t_{on} \gtrsim$ 40 μsec) to the supply voltage. The probe current exhibits a temporary increase above the expected electron saturation current ($I_{e,sat} = \pi r_D^2 \times ne [kT_e/2\pi m_e]^{1/2} \simeq 1$ A) whenever the supply voltage exceeds the plasma potential. Current overshoots have earlier been observed[7] and explained theoretically[2,7] by excess ions in the probe sheath but here we will show that the underlying physics is different. After the first current overshoot smaller current peaks appear at somewhat regular time intervals. This implies that no steady-state ($\partial/\partial t \simeq 0$) currents exist, presumably because the plasma has been radically perturbed by the first overshoot. This Letter concentrates on the first overshoot ($I_{max} = 10$ A) caused by an 80-V bias [Fig. 1(b)].

The penetration of currents or magnetic fields is addressed by observation of the temporal evolution of magnetic energy density, $B^2/2\mu_0$, as shown in Fig. 2. The front of the magnetic energy-density perturbation, arbitrarily chosen as the first contour, assumes a speed of $v \simeq 2 \times 10^7$ cm/sec, nearly the thermal electron drift speed to the probe, $v_{d,e} = (kT_e/2\pi m_e)^{1/2} \simeq 2 \times 10^7$ cm/sec, but lower than the speed of a whistler wave packet of 2-μsec duration,

$$v_g \simeq 2c/\omega_{pe}(\omega\omega_{ce})^{1/2} \simeq 9 \times 10^7 \text{ cm/sec.}$$

and much faster than the Alfvén speed,

$$v_A = B_0/(\mu_0 nm_i)^{1/2} \simeq 3 \times 10^6 \text{ cm/sec,}$$

and the ion sound speed,

$$c_s = (kT_e/m_i)^{1/2} \simeq 2 \times 10^5 \text{ cm/sec.}$$

The region of maximum energy, which is also the region of maximum current density, does not extend far ($z \leq 20$ cm) from the electrode. The axial divergence implies that currents are not confined to flow along the flux tube but must funnel radially in from the entire plasma into the electrode.

Examination of the current density reveals the existence of both parallel and perpendicular currents. Figures 3(a) and 3(b) display, for example, the current density ($J_\parallel \leq 0.7$ A/cm^2, $J_\perp \leq 0.4$ A/cm^2) in the plane $z = 5$ cm at $t = 1.5$ μsec. The direction of $J_\perp$ is mainly azimuthal to the flux tube, i.e., a Hall current, and partly radial outside the flux tube. Consequently,
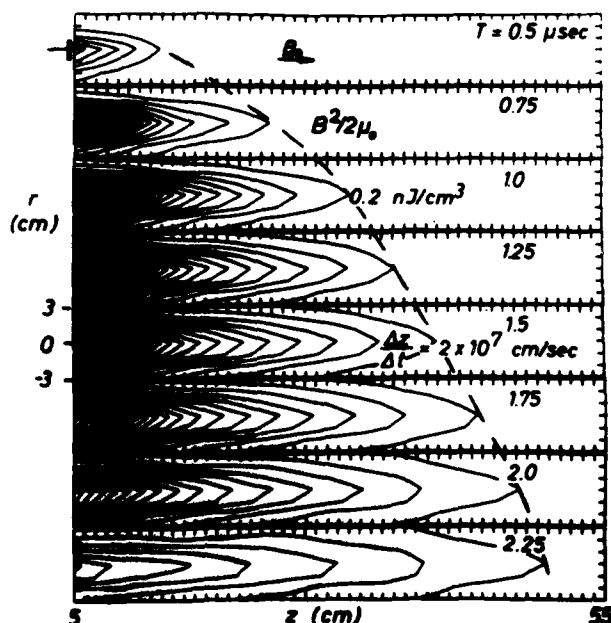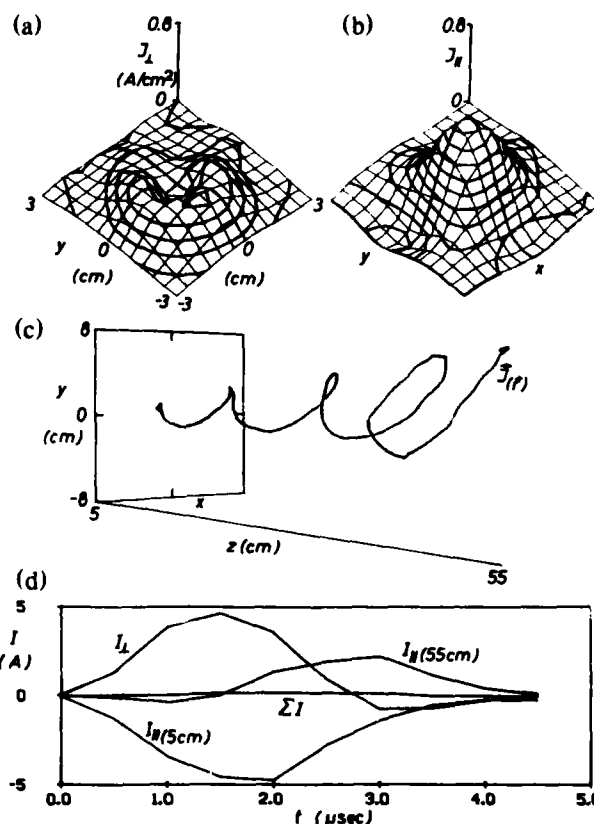

FIG. 2. Contours of constant magnetic energy density in the r-z plane at different times. Contour separation is 0.2 nJ/cm^3. The front asymptotically assumes a speed of 2×10^7 cm/sec. The electrode is shown to scale in the first panel; however, it is located at $z = 0$ cm.

FIG. 3. (a) Topological map of $J_\perp$ for a limited region about the origin for the plane $z = 5$ cm at $t = 1.5$ sec. Contour spacing is 0.08 A/cm^2. Maximum value is 0.8 A/cm^2.
(b) Same as (a) but for $J_\parallel$. Maximum value is 0.4 A/cm^2.
(c) Trajectory of a current density line at $t = 1.5$ μsec exhibiting the right-handed, conical helix of varying pitch path.
(d) Current at the boundaries of the explored volume as a function of time.

716

the current flows along nested right-handed conical helices whose apex is at the electrode. Because $J_\perp/J_\parallel$ is a function of space, the pitch and conical angle of the helices vary continuously. A typical example out of the infinite set of current-density lines is shown in Fig. 3(c). While the current density describes the local properties of the current system one would also like to know the integrated currents $I = \int \mathbf{J} \cdot d\mathbf{A}$. Figure 3(d) shows that the current across the surface closest to the electrode ($I_{\parallel,z=5\,\text{cm}}$) evolves in time as the externally measured current [Fig. 1(b)]. Its magnitude, however, is not the same since it is measured at $z = 5$ cm. Current flowing through the opposite surface ($I_{\parallel,z=55\,\text{cm}}$) is initially much smaller than the current at $z = 5$ cm. However, the perpendicular current flowing out of the four side surfaces of the rectangular volume explored [Fig. 3(c)] account for $I_{\parallel,z=5\,\text{cm}}$ in spite of the low magnitude of $J_\perp$ on the boundaries. Hence, current is funneled into the electrode. Only after the current overshoot begins to decay does $I_{\parallel,z=55\,\text{cm}}$ overtake $I_\perp$ as the source for $I_{\parallel,z=5\,\text{cm}}$. The late appearance of flux across the plane at $z = 55$ cm is clearly due to the propagation of the current front. The closure path for the current therefore evolves in time and probably encompasses the entire plasma volume. It is appropriate to note that

$\sum I = \oint \mathbf{J} \cdot d\mathbf{A}$ is not strictly zero at all times ($\approx 5\%$ of $I_\perp$ at $t = 1.5$ μsec) indicating that current measurements may have a similar error.

Upon switchon of the electrode bias, the plasma potential is observed to rise with negligible delay throughout the entire plasma by as much as $\Delta\phi \approx 30$ V and near the probe by $\Delta\phi \approx 40$ V. The global potential shift is caused by the return electrode (grid anode and chamber walls) which must draw an ion current equal to the electrode electron current so as to maintain charge neutrality. The local potential gradients near the electrode are observed to extend well beyond the sheath region [thickness $\delta = (\Delta\phi/kT_e)^{1/2}\lambda_{De} \approx 5\lambda_{De} \approx 0.15$ mm]. Figure 4 shows vector maps of the net electric field, $\mathbf{E}(r,t) = -\nabla\phi - \nabla(nkT_e)/ne$. Inductive electric fields are negligible compared to the electrostatic fields [$\partial A/\partial t \approx 1$ mV/cm]. One can observe the following features: (a) At early times ($t \approx 1$ μsec) the electric field is predominantly radial ($E_r \approx 2$ V/cm) as a result of an excess positive charge [$(n_i - n_e)/n_i \approx 10^{-4}$] in the flux tube caused by electron drain to the probe; and (b) as the probe current peaks, an unexpectedly strong parallel field [$E_z \gtrsim 4$ V/cm $\gg \nabla(nkT_e)/ne$] builds up near the probe ($z < 3$ cm). The consequence of the radial field is an azimuthal drift of the magnetized electrons ($v_\theta = E_r \times B_0/B_0^2 \approx 6 \times 10^6$ cm/sec) producing the Hall currents ($J_\theta \approx ne v_\theta \lesssim 0.4$ A/cm²) and a radial outflow of the unmagnetized ions ($r_{ci} \approx 20$ cm $\gg r_{ft} \approx 2$ cm $\gg r_{ce} \approx 2$ mm) causing a small radial current density ($J_r = nec_s \approx 5$ mA/cm²),

$\vec{E} = -\nabla\phi - \nabla p/ne$
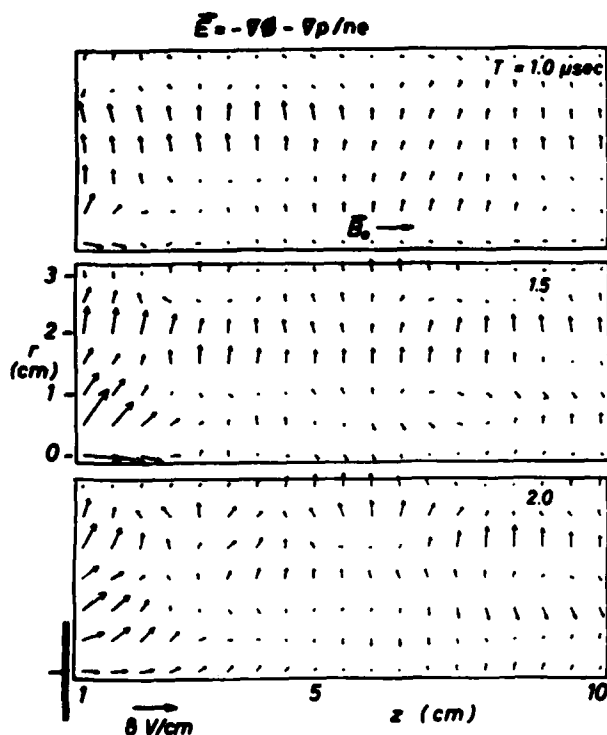
FIG. 4. Vector field map of the net electric field, $\mathbf{E}(r,t) = -\nabla\phi - \nabla_{p/ne}$, for selected times. The electrode is shown to scale in the bottom panel; however, it is at $z = 0$ cm.
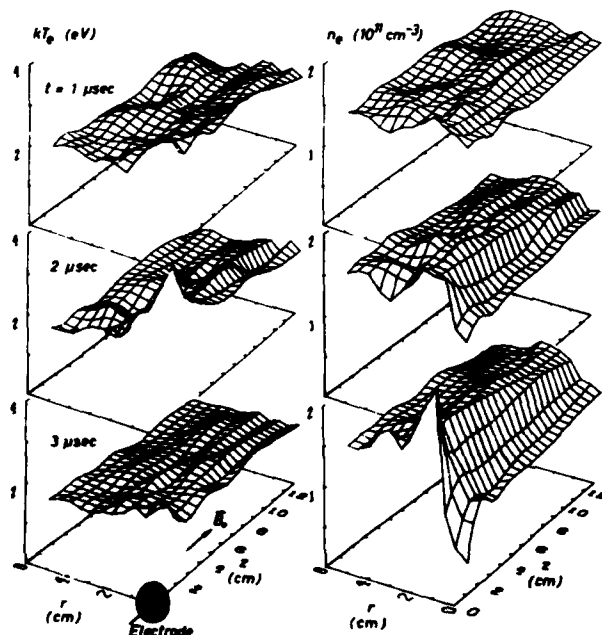

FIG. 5. Space-time dependence of electron temperature, kT_e, and density, n_e.

which when integrated over the large cylindrical area involved yields significant currents ($I_{\perp i} = 2\pi r_{fl} L_{\parallel} J_r \simeq 3.1$ A). The Hall current is expected to generate ion-sound turbulence[8] ($v_\theta \gg c_s, T_e \gg T_i$) producing azimuthal-wave electric fields, E_θ, and radially inward electron Bohm transport[3] ($I_{\perp e} \gtrsim I_{\perp i}$). Thus the radial transport of ions and electrons accounts for the unexpected cross-field currents. The large parallel electric field produces electron heating [or increase in mean energy if $f_e(v,r,t)$ is non-Maxwellian] and acceleration of ions away from the electrode with a resultant density depression. Both of these effects are shown in Fig. 5 which displays kT_e and n vs (r,z) at different times. Local heating is observed during times and locations of strong $\mathbf{E} \cdot \mathbf{J}$ ($t \approx 1.5$ μsec, $z < 3$ cm). The increase in kT_e and the electron-ion drift velocity produces ion acoustic[8] and Buneman[9] instabilities ($v_d \simeq 1.2 \times 10^8$ cm/sec $> v_{th,e} \simeq 7 \times 10^7$ cm/sec $\gg c_s$, $T_e \gg T_i$) which have been tentatively identified in observed density-fluctuation spectra. Such instabilities produce the anomalous parallel conductivity[10] which, in turn, explains the large parallel electric fields.

In summary, currents far above the electron saturation current can momentarily be collected in a magnetoplasma. Such large currents are due to the appearance of anomalous conductivity and are possible only when the electrode bias is rapidly switched above the plasma potential. The large currents are terminated by the onset of anomalous electric fields which lead to ion expulsion, and hence density depletion, from the vicinity of the electrode. The observations have profound bearing in the use of rapidly swept Langmuir probes, charging of spacecraft, and the proposed shuttle electrodynamic tether system.[4]

[1]H. M. Mott-Smith and I. Langmuir, Phys. Rev. 28, 724 (1926).

[2]F. F. Chen, in *Plasma Diagnostic Techniques*, edited by R. H. Huddleston and S. Leonard (Academic, New York, 1965), p. 113.

[3]D. Bohm, in *The Characteristics of Electrical Discharges in Magnetic Fields*, edited by A. Guthrie and R. K. Wakerling (McGraw-Hill, New York, 1949), Chaps. 1, 2, and 9.

[4]L. M. Linson, J. Geophys. Res. 74, 2368 (1969); P. M. Banks, P. R. Williams, and K.-I. Oyama, Planet. Space Sci. 29, 139 (1981); H. B. Garrett, Rev. Geophys. Space Phys. 19, 577 (1981); U. Samir, N. H. Stone, and K. H. Wright, Jr., J. Geophys. Res. 91, 277 (1986).

[5]T. Dote, H. Amemiya, and T. Ichimiya, Jpn. J. Appl. Phys. 3, 789 (1964); M. Sugawara and Y. Hatta, J. Appl. Phys. 36, 314 (1965); F. F. Chen, C. Etievant, and D. Mosher, Phys. Fluids 11, 811 (1968).

[6]W. Gekelman and L.-Y. Xu, Rev. Sci. Instrum. (to be published).

[7]D. G. Bills, R. B. Holt, and B. T. McClure, J. Appl. Phys. 33, 29 (1962).

[8]D. B. Fried and R. W. Gould, Phys. Fluids 4, 139 (1961); D. B. Fenneman, M. Raether, and M. Yamada, Phys. Fluids 16, 871 (1973); R. L. Stenzel and W. Gekelman, Phys. Fluids 21, 2024 (1978).

[9]O. Bunemann, Phys. Rev. 115, 503 (1959).

[10]K. Papadopoulos, Rev. Geophys. Space Phys. 15, 113 (1977).

102